Switchable Microtopographies based on the Two-Way Shape Memory Effect in Nickel-Titanium Alloys

Dissertation

zur Erlangung des Grades
des Doktors der Ingenieurwissenschaften
der Naturwissenschaftlich-Technischen Fakultät III
Chemie, Pharmazie, Bio- und Werkstoffwissenschaften
der Universität des Saarlandes

UNIVERSITÄT
DES
SAARLANDES

von
MAREIKE FRENSEMEIER

Angefertigt am INM – Leibniz Institut für Neue Materialien
Metallische Mikrostrukturen / Schaltbare Oberflächen

Saarbrücken,
Januar 2016

Tag des Kolloquiums: 24. Juni 2016	
Dekan:	Prof. Dr.-Ing. Dirk Bähre
Vorsitzender:	Prof. Dr.-Ing. Frank Mücklich
Berichterstatter:	Prof. Dr. Eduard Arzt Prof. Dr. Stefan Seelecke Prof. Dr. Anand Jagota
Akad. Mitarbeiter:	Dr.-Ing. Frank Aubertin

Meinen Eltern

“The greatest compliment that was ever paid me was
when one asked me what I thought,
and attended to my answer.”

— Henry David Thoreau

Abstract

Nickel-titanium (NiTi) shape memory alloys are functional materials that are capable of undergoing a reversible temperature-induced shape change. Specifically in martensitic NiTi alloys, a reversible two-way shape memory effect can be induced using indentation techniques enabling a temperature-induced change in topography. Combining switchable topographies with nano- or microstructures could expand the properties of functional surfaces, and in addition make the surfaces responsive to their environment. For example, it would be possible to change the adhesive properties of surfaces with switchable dry adhesive microstructures or to control celladhesion on implant materials with specific nano- and micro-switchable structures.

In this study, the indentation induced two-way shape memory effect was investigated in different NiTi alloys. In particular, the effects of alloy microstructure, deformation parameters (training) and thermal treatments on switchability were explored. In an austenitic NiTi alloy a specific thermal treatment led to the formation of coherent precipitates, which were shown to be crucial for the two-way shape memory behavior; exceeding the phase transformation temperature considerably decreased the switchability of the topography. At higher temperatures the stabilized martensite, which is required for an oriented phase transformation and consequently for the two-way shape memory behavior, transforms to austenite.

An embossing and an electrochemical forming process were developed to prepare switchable topographies on larger areas. Both methods led to surface arrays on NiTi with two-way shape memory topographies.

Finally, two approaches were presented, which use the switchable topographies to enable switching of a formerly passive surface function. In combination with bioinspired dry adhesive structures, the switchable NiTi topography led to a reversible, temperature-induced change of the adhesive properties of the surface. Secondly, the two-way shape memory effect was transferred to an alloy system with a phase transformation temperature near body temperature and a small width of hysteresis. By this, a switchable topography was induced, which is controllable within a physiological temperature range. The only issue impeding the use of this switchable surface for experiments on cell-surface interactions is an increased leakage of harmful copper ions. Therefore, surface passivation through oxidation is presented as a method to reduce the ion leakage.

Kurzzusammenfassung

Nickel Titan (NiTi) Formgedächtnislegierungen ermöglichen eine Formänderung als Funktion der Temperatur. Bei martensitischen NiTi-Legierungen kann durch Indentieren der Oberfläche ein reversibler Zwei-Weg Formgedächtniseffekt induziert werden, der die Ausbildung thermisch schaltbarer Topographien bewirkt. Die Kombination dieser schaltbaren Topographie mit funktionalen Nano- oder Mikrostrukturen erlaubt die Entwicklung von Oberflächen mit schaltbaren Eigenschaften. Beispielsweise ließe sich durch eine schaltbare Topographie das Zellwachstum auf Implantatmaterialien steuern, oder in Kombination mit trocken-adhäsiven Mikrostrukturen, die Adhäsionseigenschaften einer Oberfläche regulieren.

In der vorliegenden Arbeit wurde der indentations-induzierte Zwei-Weg Formgedächtniseffekt in verschiedenen Legierungen untersucht, insbesondere der Zusammenhang zwischen Schaltbarkeit und Verformung, Mikrostruktur und Temperaturänderung. In einer austenitischen NiTi-Legierung führte eine gezielte Temperaturbehandlung zur Bildung kohärenter Ausscheidungen, welche sich als entscheidend für eine schaltbare Topographie gezeigt haben. Wurde die Phasenumwandlungstemperatur weit überschritten, wandelte sich der für den Zwei-Weg Formgedächtniseffekt notwendige stabilisierte Martensit in Austenit um, was eine Rückumwandlung der Topographie verhindert.

Um schaltbare Topographien auf größeren Flächen zu erzeugen, wurden ein Kaltpräge- und ein elektrochemisches Abtragungsverfahren entwickelt. Beide Methoden ermöglichten die Herstellung von schaltbaren NiTi- Oberflächen.

Dass dynamische Topographien in NiTi für die Schaltbarkeit einer passiven Oberflächenfunktion genutzt werden können, wurde in zwei Ansätzen aufgezeigt. In Kombination mit bioinspirierten Haftstrukturen wurde eine reversible temperatur-induzierte Änderung der adhäsiven Eigenschaften einer Oberfläche ermöglicht. Außerdem wurde der Zwei-Weg Formgedächtniseffekt auf ein quaternäres Legierungssystem mit einer Phasenumwandlungstemperatur nahe der Körpertemperatur und schmaler Hysteresebreite übertragen. Hieraus resultierte eine Oberfläche, deren Topographie sich innerhalb eines physiologisch tolerierbaren Temperaturfensters schalten lässt. Einzig eine erhöhte Abgabe von zellschädigenden Kupferionen stand der Untersuchung einer Zellwechselwirkung mit der schaltbaren Oberfläche entgegen. Mit dem Ziel die Ionenabgabe zu reduzieren, wurde deshalb die Oberfläche durch Oxidation passiviert.

Danksagung

Die vorliegende Dissertation ist am INM – Leibniz Institut für Neue Materialien in Saarbrücken unter der Leitung von Prof. Dr. Eduard Arzt in den Forschungsgruppen metallische Mikrostrukturen und schaltbare Oberflächen entstanden.

Während der Bearbeitung habe ich von vielen Seiten, wissenschaftlich wie privat, Unterstützung erfahren dürfen. An dieser Stelle möchte ich mich bei allen für ihren Beitrag zu dieser Arbeit bedanken.

Allen voran gilt mein Dank meinem Doktorvater *Prof. Dr. Eduard Arzt* für die Ermöglichung dieser Dissertation, die konstruktiven Anregungen und die stetige Unterstützung.

Ebenfalls möchte ich mich herzlich bei *Prof. Dr. Stefan Seelecke* für die motivierenden Gespräche und die Übernahme des Zweitgutachtens bedanken.

Für ihren Einsatz während und nach ihrer Zeit als Juniorforschungsgruppenleiter am INM verdienen *Dr. Andreas Schneider* und *Dr. Elmar Kroner* meine Anerkennung und ein großes Lob. Mit ihren fachlichen Ratschlägen und neuen Ideen haben sie einen besonderen Beitrag zum Fortgang dieser Arbeit geleistet. Neben einem freundschaftlichen Arbeitsklima stieß ich bei ihnen stets auf ein offenes Ohr, viel Verständnis und, nicht zu vergessen, eine konstante Versorgung mit Nervennahrung.

Weiterhin möchte ich auch *Dr. Carl Frick* von der University Wyoming danken, er hat mich nicht nur mit den komplexen Eigenschaften von Formgedächtnislegierungen vertraut gemacht sondern auch damit, dass Wyoming deutlich mehr als Cowboys zu bieten hat.

Ein ‚Dangschee' gilt auch *Birgit Heiland* - ohne die vielen Tipps und Tricks zur Probenpräparation ‚däd i wohl heid no poliera ond schloifa ond häd nichts gmachd ghedd'. Ebenso möchte ich mich bei *Jörg Schmauch*, *Rudolf Karos*, *Robert Drumm* und *Dr. Yuliya Silina* für ihre Unterstützung bei den TEM Aufnahmen, XRD-, DSC und ICP-MS Messungen bedanken sowie bei *Dr. Vera Bandmann* und *Isabella Reichert* für die Durchführung der Zellversuche. Für die Konstruktion und kontinuierliche Rekonstruktion des Mikro-Heizers gilt mein Dank dem *Team der Werkstatt*, das sich den Verbesserungswünschen und Reparaturen geduldig angenommen hat.

Dank des großen Zusammenhalts und der Unternehmungsfreude des gesamten Kollegenkreises kam auch der Ausgleich abseits der Wissenschaft nicht zu kurz. Neben meinen Kollegen aus den ehemaligen Juniorforschungsgruppen Metallische Mikrostrukturen und Schaltbare Oberflächen möchte ich mich insbesondere bei *Dr. Jennifer Atchison*, *Amanda Bellafatto*, *Dr. Nathalie Guimard*, *Dr. René Hensel*, *Nicolas Jäckel*, *Jessica Kaiser*, *Bentejui Medina Clavijo*, *Maurizio Micciché*, *Nicolas Peter*, *Julia Purtov*, *Dominik Schirra*, *Mariana Viegas Greco de Oliveira* und *Paula Yagüe Isla* für das schöne Gefühl bedanken, mit guten Freunden zusammen zu arbeiten.

Abschließend gilt mein persönlicher Dank meinen Freunden und meiner Familie in der Heimat sowie meinem Freund *Jona*. DANKE, für die großartige Unterstützung trotz der zeitweise großen Entfernung, die Ausdauer und das entgegengebrachte Verständnis während der Anfertigung dieser Arbeit.

Contents

Abbreviations and symbols

A	Contact area
a	Radius of the contact area
A_f	Austenite finish temperature
A_s	Austenite start temperature
a_s	Aspect ratio of the PECM structures
d	Diameter of pillar tip
d_c	Indentation depth after cooling below M_f
d_h	Indendation depth after heating above A_f
d_i	Indentation depth after indentation
DSC	Differential scanning calorimetry
E	Young’s modulus
E^*	Reduced elastic modulus
EBSD	Electron backscatter diffraction
ECM	Electrochemical machining
EDM	Electrodischarge machining
F	Applied load
F_C	Pull-off force, minimum negative load
F_{CB}	Pull-off force in the bumpy state
F_{CF}	Pull-off force in the flat state
FEA	Finite element analysis
FIB	Focused ion beam
h_s	Height of the structures
ΔH	Enthalpy difference
I	Current pulse
ICDD	International center for diffraction database
ICP-MS	Inductively coupled plasma mass spectrometry
JKR	Johnson-Kendall-Roberts modell
l_c	Diameter of the cavity in the cathode
lN	Liquid nitrogen
l_s	Length of cross-section of the structures at the base
MEMS	Micro electromechanical systems

M_f	Martensite finish temperature
M_s	Martensite start temperature
NiTi	Nickel-titanium alloy
OWSME	One-way shape memory effect
$\bar{P}$	Ratio of load to pull-off force
PBS	Phosphate-buffered saline
PDMS	Polydimethylsiloxane
PECM	Pulse electrochemical machining
R	Reduced radius
R_a	Average roughness
R_{CF}	Effective radius in the flat state
R_{CB}	Effective radius in the bumpy state
R_f	R-phase finish temperature
RR_{OW}	Recovery ratio one-way shape memory
R_s	R-phase start temperature
RR_{TW}	Recovery ratio two-way shape memory
R_z	Peak-to-valley roughness
S	Switching efficiency
ΔS	Entropy difference
SEM	Scanning electron microscopy
SIM	Stress induced martensite
SMA	Shape memory alloy
SME	Shape memory effect
T	Stress-induced transformation temperature
T_0	Temperature of thermodynamic equilibrium
TEM	Transmission electron microscopy
TWSME	Two-way shape memory effect
WLI	White-light interferometer
XRD	X-Ray Diffraction
w	Work of adhesion
z_0	Equilibrium separation
ε	Strain
σ	Stress

σ_y	Yield stress
υ	Poisson’s ratio
μ	Ratio of elastic displacement at the point of pull-off

Chapter 1
Introduction

Functional surfaces with super-hydrophobic, (anti)-reflective, adhesive or bioactive properties play a central role for new developments in research areas such as tribology, microfluidics or biomedicine.[1-5] In many cases these surface properties were induced using functional micro- or nanostructures or even a hierarchical morphology, as found in the lotus leaf, the natural prototype for super-hydrophobic surfaces.[6] In addition, functional coatings and changes in the surface texture are frequently used to improve or change surface properties such as wettability or friction.[7-8] For these properties the surface topography on micro- and nanometer scale plays an important role and induces macroscopic effects.[9]

So far, mostly passive structures and materials have been used to obtain certain functionalities. Recently, investigations in the field of 'smart', 'stimuli-responsive', 'intelligent', 'active' or 'dynamic' materials and hybrid systems have gained increasing attention. The ability to change and control specific surface properties could enable applications from data-storage, over microelectromechanical systems to dynamic biomedical surfaces, guiding cell-adhesion, and surfaces with adaptive reflectivity. Besides complex molecular systems, which show a responsive chemical modification, shape memory materials, which are able to manifest a shape change, have been used to trigger surface functionalities. Many of these systems are based on polymers changing their physio-chemical properties activated by pH, humidity, light or temperature.[10-12] Only a few studies are available using inorganic and metal-based responsive surfaces. Most of these switchable systems obtain their active properties by a combination with a modified polymeric surface layer or physical adsorption of polymer molecules.[12-13] These hybrid systems combine the mechanical advantages of a passive metal with the switchable properties of an active polymer. However, switchable metallic topographies could surpass switchable polymeric topographies in particular for load bearing or high temperature applications. Magnetism, electric currents and inductive heating could be used as external stimulus and induce a shape change in shape memory alloys with actuation forces exceeding those of polymers by far.[14-16] Regarding biomedical applications, metal based implants were frequently used and medically proven.[17]

Prominent responsive metallic materials are nickel-titanium (NiTi) shape memory alloys. Near equiatomic NiTi alloys show a reversible shape change triggered by a change in temperature and extraordinarily high elastic deformation, called pseudoelasticity. Their exceptional mechanical properties make them a frequently used material in actuator applications and biomedicine.[18-19] For example, pseudoelastic NiTi materials are used in orthodontic wires or in flexible stents for endovascular therapy.[20-22] Only few applications, such as actuators, control devices, or fasteners, make use of the two-way shape memory behavior in NiTi alloys.[23-25]

Depending on the alloy composition and specific thermomechanical training, either the one-way shape memory effect (OWSME) or the two-way shape memory effect (TWSME) can be exploited. Previous research on the two-way shape memory effect has established temperature-induced switchable topographies in NiTi shape memory alloys. Indentation followed by planarization yielded a shape memory effect, where the topography of the NiTi surface reversibly changed from flat to textured. The switch is controlled by heating above, or cooling below the characteristic phase transformation temperatures of the alloy.[16, 26-28]

So far, the detailed microstructural mechanisms behind the indentation induced TWSME remain unclear, especially the influence of heat treatments on the TWSME is not well understood. A better knowledge on the adaptation of the phase transformation temperatures and on the enlargement of protrusion height and reversibility is required for technical application. For example, could this enable a switch of topographies at physiological conditions and improve the manufacturing technology for such switchable metallic topographies.

Apart from a study by Fei et al. the focus of previous studies has been on the scientific investigation of the effect. The same indentation preparation technique presented in the first study by Zhang et al. was used, which is rather complex and time consuming.[27, 29] No method has been presented for a training of the TWSME on larger areas that enables a parallel preparation. This step is crucial for upscaling of switchable metallic arrays and subsequent implementation into process engineering.

Apart from a wear resistant coating, applications of metallic switchable topographies have been rarely investigated. [30] The usage of such a switchable metallic topography is very promising regarding the control of surface properties. The change in topography from flat to textured might have a strong impact on the contact area. In particular, properties which are strongly related to the surface topography, such as friction, wettability or adhesion, could be controlled.

The development of a hybrid system, combining switchable metallic surface topographies with functional coatings and microstructures could further extend the field of applications. For example, could a combination with dryadhesive microstructures induce switchable adhesive properties for pick and place applications. In biomedicine, the control of the surface topography of a hybrid NiTi implant system may promote the healing process, e.g. by controlled drug release or by influencing cell proliferation due to controlled wettability and surface roughness.[31-32]

With respect to these possible applications, the aim of this thesis is to understand the indentation induced shape memory effect and its influence on switchable surface structures in more detail. Furthermore, with a view to a possible upscaling, preparation techniques that enable large area patterning were developed. Finally, two applications of switchable metallic topographies will be presented; an approach using a shape memory topography in a NiTi-polymer hybrid system to gain temperature-induced switchable adhesion, and a switchable topography activated near body temperature using a new shape memory alloy. This thesis is outlined as follows:

After the introduction in the *first chapter,* in the *second chapter* the nature of NiTi shape memory alloys, the martensitic phase transformation and the indentation induced two-way shape memory effect are described. Furthermore, a brief overview on the current state of the art in micro manufacturing and structuring of NiTi alloys is given. The chapter ends with a detailed overview of the current research in the field of functional micro- and nanostructures, coatings and topographies. In particular, developments on switchable dry adhesive and biomedical surfaces are emphasized.

The *third and the fourth chapter* present the research on the influence of precipitates on the two-way shape memory effect. This work was started by Dr. Enwei Qin and completed during this thesis with additional differential scanning calorimetry (DSC), indentation and temperature cycling measurements to analyze the effect of aging on the indentation induced two-way-shape memory effect in austenitic NiTi. In *chapter 5* embossing and pulse electrochemical machining are reported as techniques to train switchable metallic surfaces based on the TWSME. Three different geometries are induced by these techniques. The resulting switchable surface arrays are quantified with focus on their morphology and reversibility using white light interferometry and thermal cycling. *Chapter 6* discusses the development of a hybrid system by combining a switchable metallic topography in NiTi with a bioinspired, micro-patterned adhesive polymer layer. The adhesion properties and reversibility of the hybrid system are measured as a function of temperature. The results are discussed in terms of a change in contact area using classic contact mechanics and a finite element analysis.

Chapter 7 introduces switchable metallic topographies activated near body temperature using a quaternary shape memory alloy. The reversible switch between flat and structured is used to investigate the control of cell adhesion and cell alignment without chemical surface modifications.

The thesis concludes in *Chapter 8* with a general discussion of the most relevant results presented in this work, and an outlook on possible investigations based on the presented findings is given. Further, ideas for subsequent developments using metallic shape memory topographies are introduced.

1.1 Publications and author contributions

Parts of the present thesis have been published with contributions of co-authors in refereed scientific journals. Two manuscripts were mainly contributed by the author of this thesis and published with first authorship; the third publication was published in co-authorship.

» Chapter 3 was published by Qin, E.; Peter, N. J.; Frensemeier, M.; Frick, C. P.; Arzt, E.; Schneider, A. S. in the article *Vickers Indentation Induced One-Way and Two-Way Shape Memory Effect in Austenitic NiTi*, *Adv. Eng. Mater.* **2014,** *16* (1), 72-79.
The author carried out the indent-depth-measurements and the evaluation and interpretation of the results. The writing of the paper was conducted in close collaboration with C. Frick and N. Peter. E. Qin was responsible for the sample heat treatment and TEM measurements. The project was supervised by E. Arzt and A. S. Schneider.

» Chapter 4 was published by Frensemeier, M.; Arzt, E.; Qin, E.; Frick, C. P.; Schneider, A. S. in the article *Indentation Induced Two-Way Shape Memory Effect*

in Aged Ti-50.9 at.% Ni, in MRS Commun. **2015,** *5* (01), 77-82.
The first author was responsible for the conduction and evaluation of the DSC, topography and temperature cycling measurements. The TEM imaging and heat treatment was carried out by E. Qin. The author wrote the manuscript and received scientific supported by E. Arzt and C. P. Frick. Both contributed with fruitful discussions. The idea and concept of the publication was developed by A. S. Schneider.

» Chapter 5 was published by Frensemeier, M., Schirra, D., Weinmann, M., Weber, O., Kroner, E. in the article *Shape-Memory Topographies on Nickel-Titanium Alloys Trained by Embossing and Pulse Electrochemical Machining* in *Adv. Eng. Mater.* **2016**, *doi: 10.1002/adem.201600012*
The author carried out the concept of the work, the sample preparation and topography change measurements. The writing of the paper was conducted in close collaboration with E. Kroner. D. Schirra performed the reversibility tests under supervision of M. Frensemeier. M. Weinmann and O. Weber provided the PECM system and were responsible for the PECM structuring process.

» Chapter 6 was published in the article *Temperature-Induced Switchable Adhesion using Nickel–Titanium–Polydimethylsiloxane Hybrid Surfaces*, by Frensemeier, M.; Kaiser, J. S.; Frick, C. P.; Schneider, A. S.; Arzt, E.; Fertig, R. S.; Kroner, E. in *Adv. Funct. Mater.* **2015,** *25* (20), 3013-3021.
The first author was responsible for all laboratory work and measurements, particularly the establishment of the hybrid systems. The adhesion measurements were supported by J. Kaiser and the advice from E. Kroner. The FEM analysis was performed by R.S. Fertig. The author has coordinated the summary of the results and the writing of the manuscript. The final manuscript was discussed and corrected with the suggestions from the co-authors C.P. Frick, E. Arzt and A.S. Schneider. The project was supervised by E. Arzt and E. Kroner.

1.2 References

1. Feng, L.; Li, S.; Li, Y.; Li, H.; Zhang, L.; Zhai, J.; Song, Y.; Liu, B.; Jiang, L.; Zhu, D., Super-hydrophobic surfaces: from natural to artificial. *Advanced Materials* **2002,** *14* (24), 1857-1860.
2. Li, Y.; Zhang, J.; Yang, B., Antireflective surfaces based on biomimetic nanopillared arrays. *Nano Today* **2010,** *5* (2), 117-127.
3. Kikuta, H.; Toyota, H.; Yu, W., Optical elements with subwavelength structured surfaces. *Optical Review* **2003,** *10* (2), 63-73.
4. Zhao, G.; Raines, A.; Wieland, M.; Schwartz, Z.; Boyan, B., Requirement for both micron-and submicron scale structure for synergistic responses of osteoblasts to substrate surface energy and topography. *Biomaterials* **2007,** *28* (18), 2821-2829.
5. Wennerberg, A.; Albrektsson, T.; Andersson, B.; Krol, J., A histomorghometric study of screw-shaped and removal torque titanium implants with three different surface topographies. *Clinical oral implants research* **1995,** *6* (1), 24-30.
6. Koch, K.; Bhushan, B.; Jung, Y. C.; Barthlott, W., Fabrication of artificial Lotus leaves and significance of hierarchical structure for superhydrophobicity and low adhesion. *Soft Matter* **2009,** *5* (7), 1386-1393.
7. Ponsonnet, L.; Reybier, K.; Jaffrezic, N.; Comte, V.; Lagneau, C.; Lissac, M.; Martelet, C., Relationship between surface properties (roughness, wettability) of titanium and titanium alloys and cell behaviour. *Materials Science and Engineering: C* **2003,** *23* (4), 551-560.
8. Pettersson, U.; Jacobson, S., Influence of surface texture on boundary lubricated sliding contacts. *Tribology International* **2003,** *36* (11), 857-864.
9. Assender, H.; Bliznyuk, V.; Porfyrakis, K., How Surface Topography Relates to Materials' Properties. *Science* **2002,** *297* (5583), 973-976.
10. Ichimura, K.; Oh, S.-K.; Nakagawa, M., Light-Driven Motion of Liquids on a Photoresponsive Surface. *Science* **2000,** *288* (5471), 1624-1626.
11. Berna, J.; Leigh, D. A.; Lubomska, M.; Mendoza, S. M.; Pérez, E. M.; Rudolf, P.; Teobaldi, G.; Zerbetto, F., Macroscopic transport by synthetic molecular machines. *Nature materials* **2005,** *4* (9), 704-710.
12. Skorb, E. V.; Andreeva, D. V., Surface Nanoarchitecture for Bio-Applications: Self-Regulating Intelligent Interfaces. *Advanced Functional Materials* **2013,** *23* (36), 4483-4506.
13. Chen, M.; Yang, X.; Hu, R.; Cui, Z.; Man, H., Bioactive NiTi shape memory alloy used as bone bonding implants. *Materials Science and Engineering: C* **2004,** *24* (4), 497-502.
14. Müller, C. W.; Pfeifer, R.; El-Kashef, T.; Hurschler, C.; Herzog, D.; Oszwald, M.; Haasper, C.; Krettek, C.; Gösling, T., Electromagnetic induction heating of an orthopaedic nickel–titanium shape memory device. *Journal of Orthopaedic Research* **2010,** *28* (12), 1671-1676.
15. Ohandley, R. C.; Murray, S. J.; Marioni, M.; Nembach, H.; Allen, S. M., Phenomenology of giant magnetic-field-induced strain in ferromagnetic shape-memory materials (invited). *Journal of Applied Physics* **2000,** *87* (9), 4712-4717.
16. Fei, X. L.; Zhang, Y. J.; Grummon, D. S.; Cheng, Y. T., Indentation-induced two-way shape memory surfaces. *Journal of Materials Research* **2009,** *24* (3), 823-830.
17. Park, J. B.; Lakes, R. S., Metallic implant materials. *Biomaterials* **2007**, 99-137.
18. Duerig, T.; Pelton, A.; Stöckel, D., An overview of nitinol medical applications. *Materials Science and Engineering: A* **1999,** *273*, 149-160.

19. Saadat, S.; Salichs, J.; Noori, M.; Hou, Z.; Davoodi, H.; Bar-On, I.; Suzuki, Y.; Masuda, A., An overview of vibration and seismic applications of NiTi shape memory alloy. *Smart Materials and Structures* **2002,** *11* (2), 218.
20. Blum, U.; Voshage, G.; Lammer, J.; Beyersdorf, F.; Töllner, D.; Kretschmer, G.; Spillner, G.; Polterauer, P.; Nagel, G.; Hölzenbein, T., Endoluminal stent–grafts for infrarenal abdominal aortic aneurysms. *New England Journal of Medicine* **1997,** *336* (1), 13-20.
21. El Feninat, F.; Laroche, G.; Fiset, M.; Mantovani, D., Shape memory materials for biomedical applications. *Advanced Engineering Materials* **2002,** *4* (3), 91.
22. Miura, F.; Mogi, M.; Ohura, Y.; Hamanaka, H., The super-elastic property of the Japanese NiTi alloy wire for use in orthodontics. *American Journal of Orthodontics and Dentofacial Orthopedics* **1986,** *90* (1), 1-10.
23. Pfeifer, R.; Müller, C. W.; Hurschler, C.; Kaierle, S.; Wesling, V.; Haferkamp, H., Adaptable orthopedic shape memory implants. *Procedia CIRP* **2013,** *5*, 253-258.
24. Kim, H.-C.; Yoo, Y.-I.; Lee, J.-J., Development of a NiTi actuator using a two-way shape memory effect induced by compressive loading cycles. *Sensors and Actuators A: Physical* **2008,** *148* (2), 437-442.
25. Perkins, J., *Shape memory effects in alloys*. Springer Science & Business Media: **2012**.
26. Ni, W.; Cheng, Y.-T.; Grummon, D. S., Microscopic shape memory and superelastic effects under complex loading conditions. *Surface and Coatings Technology* **2004,** *177*, 512-517.
27. Zhang, Y.; Cheng, Y. T.; Grummon, D. S., Shape memory surfaces. *Applied Physics Letters* **2006,** *89*, 041912.
28. Zhang, Y.; Cheng, Y.-T.; Grummon, D. S., Two-way indent depth recovery in a NiTi shape memory alloy. *Applied Physics Letters* **2006,** *88* (13), 131904-131904-3.
29. Fei, X.; Grummon, D. S.; Ye, C.; Cheng, G. J.; Cheng, Y.-T., Surface form memory in NiTi shape memory alloys by laser shock indentation. *Journal of Materials Science* **2012,** *47* (5), 2088-2094.
30. Ni, W.; Cheng, Y.-T.; Grummon, D. S., Wear resistant self-healing tribological surfaces by using hard coatings on NiTi shape memory alloys. *Surface and Coatings Technology* **2006,** *201* (3), 1053-1057.
31. Hermawan, H.; Dubé, D.; Mantovani, D., Developments in metallic biodegradable stents. *Acta Biomaterialia* **2010,** *6* (5), 1693-1697.
32. Ranella, A.; Barberoglou, M.; Bakogianni, S.; Fotakis, C.; Stratakis, E., Tuning cell adhesion by controlling the roughness and wettability of 3D micro/nano silicon structures. *Acta Biomaterialia* **2010,** *6* (7), 2711-2720.

Chapter 2

Fundamentals and literature review

2.1 Shape memory effects in nickel-titanium alloys

Intermetallic NiTi shape memory alloys respond to external mechano-caloric stimuli. They are frequently used in micromechanical and biomedical devices as actuators, sensors and implant materials.[1-3] All of these applications originate from the shape memory effect or pseudoelasticity; two complex behaviors associated with an austenite-martensite phase transformation.[4] In order to increase the magnitude of shape change and the reversibility, the underlying martensitic phase transformation has been the subject of continued research since its discovery in 1963.[5] NiTi alloys show extraordinarily strong pseudoelastic properties and a reversible shape change even for relatively large strains up to 8%.[6] In addition to their shape memory behavior, good corrosion resistance and biocompatibility compared to other shape memory alloys makes them an excellent candidate for advanced biomedical and implant applications.[7-8]

2.1.1 The martensitic phase transformation

NiTi alloys with shape memory effect typically have a near equiatomic composition. At moderate temperatures (<650 °C), the region of homogeneity is quite narrow and lies between 50.0 and 50.5 at.% Ni.[9] In this temperature range, slightly Ni-rich alloys (>50.5 at.% Ni) decompose upon ageing into metastable Ti_3Ni_4, Ti_2Ni_3 and subsequently $TiNi_3$. Especially, the Ti_3Ni_4 phase influences the shape memory effect due to a lattice distortion by the formation of coherent precipitates.[10-11] Their anisotropic shrinking of 2.7 % in the [111]-direction and only 0.3 % in the perpendicular orientation leads to a lenticular shape surrounded by strain fields, as shown in Figure 2.1.[11] The phase transformation temperatures can be altered by changing the composition, additional alloying elements, and by thermo-mechanical treatments of the alloy. In binary NiTi alloys of 50.0 to 51.5 at.% Ni, M_s decreases by 150°C per at.% Ni until no martensite phase transformation occurs anymore.[12]

The shape change recovery of NiTi shape memory alloys is based on a martensitic phase transformation, a shear-dominant diffusionless solid-state phase transformation. As shown in Figure 2.2, the martensitic phase transformation involves an athermal first-order displacive transformation from the cubic B2 high-temperature parent phase (austenite, A) to the monoclinic B19' low-temperature phase (martensite, B).[4] Ageing and thermo-mechanical treatments, enable a two-step transformation from the highly symmetric B2 phase over the trigonal R-Phase to the lower symmetric B19' phase.[13]

The martensitic B19' unit cell is elongated over 10% compared to the austenitic B2 unit cell in the [223] B2-orientation and an order larger than the R-phase with an elongation of 0.94% along the [111] B2-orientation.[14-16] The shape change in NiTi alloys is driven by this change of transformational volume and the high mobility of twin boundaries under the influence of shear stress. In polycrystalline NiTi shape memory alloys, the martensitic phase transformation is driven by nucleation and growth. Nucleation preferably evolves at phase and grain boundaries, at temperatures below the martensitic start temperature M_s. Below the martensitic finish temperature M_f the phase transformation is completed and the material is fully martensitic. Analogously, the transformation from the low temperature martensitic phase to the high temperature austenitic phase starts at the austenite start temperature A_s and continuous until the austenite finish temperature A_f is reached and the material is in a fully austenitic state.

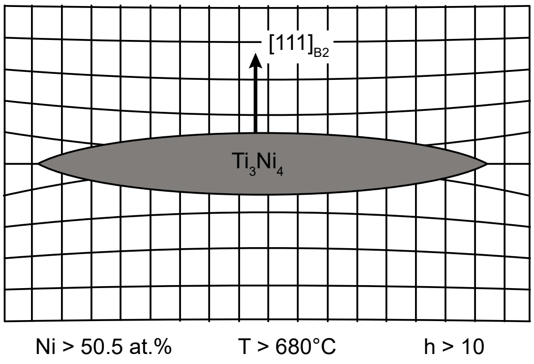

Figure 2.1: Schematic of the lattice distortion and intrinsic stress fields induced by shrinking of coherent Ni_4Ti_3 precipitates. Modified after Tadaki et al.[11]

The phase transformation temperatures can be altered by changing the composition, additional alloying elements, and by thermo-mechanical treatments of the alloy. In binary NiTi alloys of 50.0 to 51.5 at.% Ni, M_s decreases by 150°C per at.% Ni until no martensite phase transformation occurs anymore.[12] Moreover, the formation of precipitates in Ni-rich alloys and the formation of a two-step transformation due to the R-Phase have to be considered.[17]

Phase transformation temperatures are usually determined by DSC, and range for NiTi from -150 to 100 °C. This temperature range generally defines the field of application of the shape memory alloy.

Furthermore, phases can be stabilized by mechanical stress. Due to the displacive nature of the phase transformation, martensite can also be induced by stress (SIM). The correlation between induced stress and temperature is described by the Clausius-Clapeyron equation:[18]

$$\frac{\mathrm{dT}}{\mathrm{d}\sigma} = -\frac{\varepsilon}{\Delta S} = -\frac{\varepsilon T_0}{\Delta H} \tag{2.1}$$

Here, T is the stress-induced transformation temperature, ε is the transformation induced strain, ΔS is the entropy, ΔH the enthalpy difference of the phase transformation, and T_0 the temperature of thermodynamic equilibrium. Accordingly, martensite can be induced by mechanical stress at a constant temperature ($T > A_f$). It spontaneously recovers after unloading since the reverse transformation takes place.

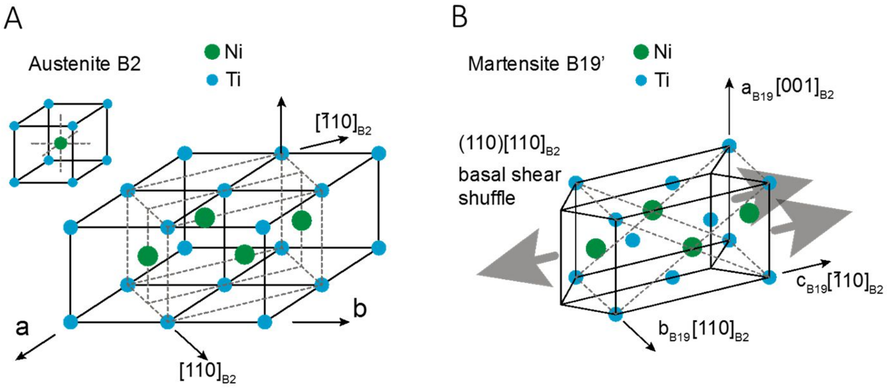

Figure 2.2: Sketch of the crystal structures in NiTi shape memory alloys.[4, 19] (A) The parent austenitic B2 structure, with four primitive cells leading to a tetragonal unit cell (dashed line). (B), The phase transformation from austenite (B2) to martensite (B19') is induced by shifting the (110) plane in the $[\bar{1}10]$-direction and a cooperative shearing of the (001) planes in $[\bar{1}10]$-direction.

This stress-induced reversible deformation, called pseudoelasticity, is limited by the temperature dependent critical stress for plastic yielding in the austenitic phase (Figure 2.3).

Once the applied stress level overcomes the critical stress for slip, before reaching the level for a stress-induced martensitic transformation, permanent deformation occurs.[20] M_s is shifted to higher temperatures with increasing stress, until the critical yield stress, σ_y, is reached. With further increasing stress level, the pseudoelastic deformation is displaced by plastic deformation.

2.1.2 The shape memory behavior

Depending on the thermomechanical treatment and loading path, the diffusion-less stress-induced martensitic transformation leads to either pseudoelastic, one-way shape memory or a two-way, i.e. repeatable, shape memory behavior (Figure 2.4). At temperatures below M_f, two different variations of martensite accommodation are shown.

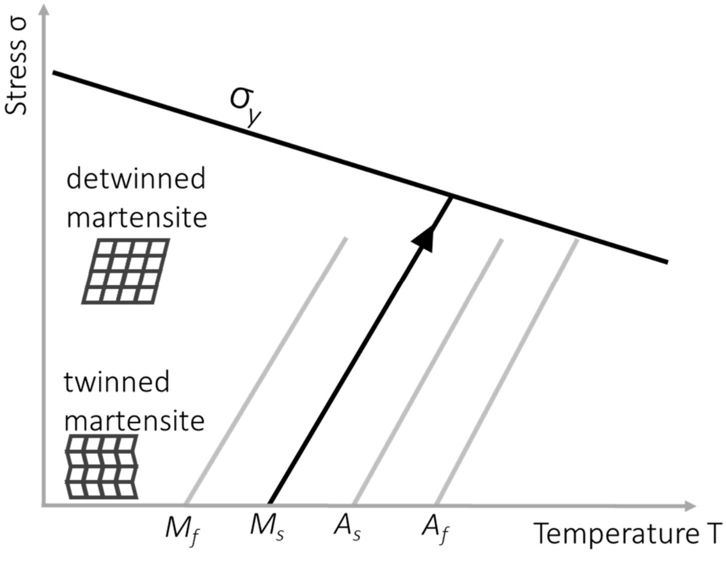

Figure 2.3: Schematic relationship between temperature and stress-induced martensitic phase transformation. After Lagoudas et al.[20]

If the martensitic transformation takes place in absence of any external mechanical stimuli, e.g. an applied stress, the multiple variants of the low-symmetric martensite show an intrinsic self-accommodation due to twinning. In this case, no macroscopic shape change can be observed. The change in symmetry enables the formation of twin-related pairs of the martensite variants, which nucleate to a single, coherent habit-plane variant.

If the transformation takes place in presence of an external mechanical load, the multiple martensitic variants re-accommodate with a preferred orientation (Figure 2.4). This detwinning process leads to a large, reversible (non-plastic) strain, accompanied by a macroscopic shape change. After heating above A_f, the material returns to the highly symmetric, single variant austenite phase and the deformation fully recovers.

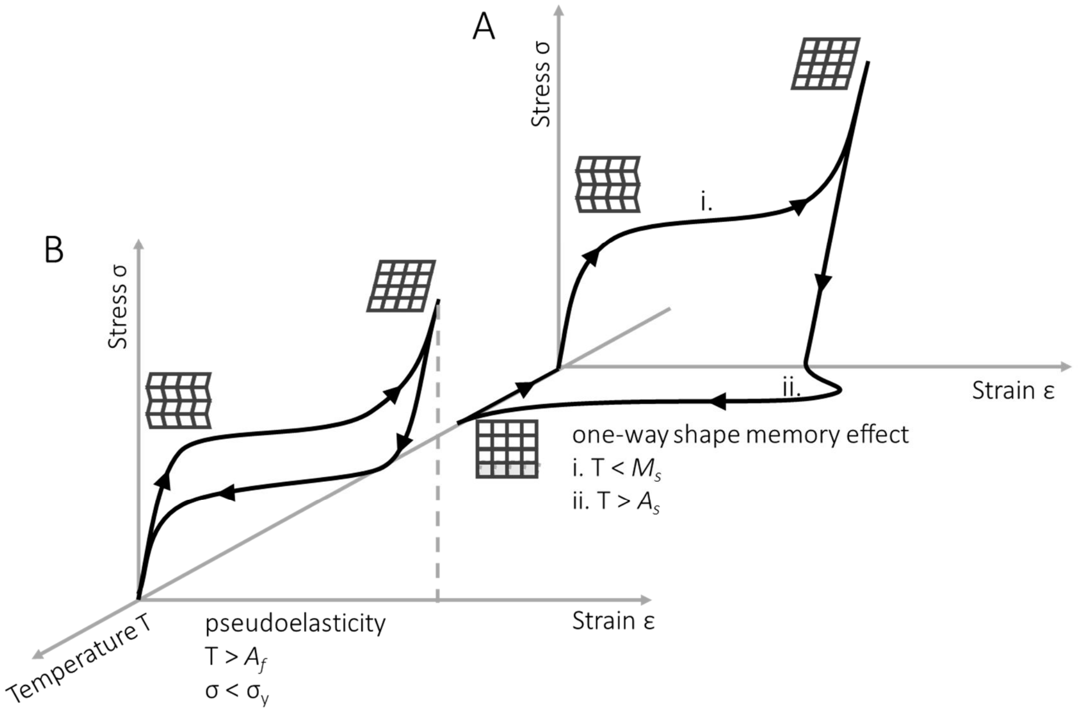

Figure 2.4: Schematic stress-strain diagram and martensitic phase transformation of (A) the one-way shape memory effect and (B) pseudoelasticity.

The memorized shape is always the austenitic shape, which can be recovered by heating the deformed, martensitic sample. Once the original austenitic shape is recovered, no re-deformation occurs during a subsequent cooling. Thus, this shape memory behavior is restricted to one switching process, the so-called one-way shape memory effect (OWSME). If the macroscopic shape recovery is inhibited during transformation from martensite to austenite, high restoring forces occur. Combined with an external bias force, the one-way shape memory effect can be used as a switchable actuator.[21]

For applications with operating temperatures above A_f, another effect is elicited due to mechanical loading, referred to as pseudoelasticity. If the material is deformed at temperatures near or above A_f, a spontaneous stress induced formation of SIM takes place. Similarly, to the transformation mechanism of the OWSME, favored martensite variants start growing and detwin depending on the magnitude of the applied stress. Thus, the microstructure and the macroscopic deformation is assumed to be the same as for lower temperatures. When the external load is removed, a sudden re-transformation to the austenitic shape occurs. The pseudoelastic deformation is directly related to the phase equilibrium temperature and the martensitic transformation temperature. It can be controlled in a mechanically loaded state and decreases immediately in the absence of load. The martensite recovers isothermally to highly symmetric austenite.

In order to elicit the two-way shape memory effect, an appropriate thermo-mechanical 'training procedure' has to be applied to the shape memory alloy.[22-23] The combination of deformation and heat treatment enables the material to memorize its shape at both high and low temperature. Thus, the two-way shape memory effect (TWSME) allows switching between the two shapes controlled by cycling temperature.

While the TWSME shows relatively low recovery strains compared to the OWSME, it shows high reversibility and high fatigue resistance.[24-25] Most training procedures create internal stress fields, which then guide the growth of oriented martensite variants. Usually, a thermomechanical training process is applied to the material, which consists of a defined heating and cooling procedure under controlled stress, strain and temperature.[3, 26] The applied stress or strain often exceeds the recoverable strain and leads to plastic slip and the generation of dislocations and stress fields. It is believed, that these stress fields act as nucleation sites for martensite variants with a favored orientation, a process that is crucial for the shape deformation in absence of an external load (Figure 2.5).[23] After the ‘training’ (i.-iii.), which induces a permanent dislocation structure in the material, a reversible deformation occurs spontaneously during thermal cycling across the transformation temperatures without any external bias (iv. –vi.).[27-28]

The internal stress, generated by the dislocations, is associated with the stabilization of martensitic variants in favored orientations. During the thermally induced transformation, these pre-oriented variants guide the direction of the overall martensitic transformation leading to a macroscopic deformation of the sample.[22]

The reversible shape change due to the TWSME has been demonstrated in various studies.[29-31] However, theoretical attempts explaining the underlying fundamental principles of the TWSME were mostly based on the analysis of experimental phenomena. A detailed analysis of the interaction between deformation, associated dislocation structures, precipitates, stress fields, and the generation of oriented martensite variants is currently missing. Only a few studies investigated the specific interaction between deformation, precipitates and the activation of martensite growth with certain variant orientation.[25, 32-33]

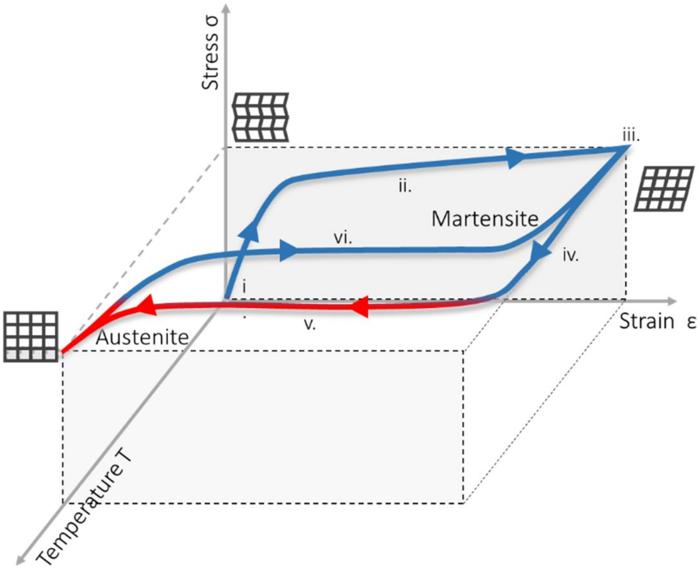

Figure 2.5: Characteristic stress-strain behavior of the two- way shape memory effect (TWSME). The oriented microstructural change during deformation and the martensitic phase transformation lead to a macroscopic shape change induced by changing temperature. No external stress is required for the shape recovery.

For example, the interaction of the dislocation structure with favored martensitic variants was investigated by transmission electron microscopy (TEM) of fatigued NiTi samples by Gall and Maier.[25] It was suggested that defect nucleation is energetically favored at the austenite-martensite interface. Norfleet et al. showed that the amount of stress-induced martensite correlates with a high dislocation density and that the orientation of the martensite twins is parallel to the dislocation accumulation.[34]

Nishida and Honma, and Gall et al. showed that, in addition to the dislocation structure, the presence of precipitates may influence the behavior of the TWSME.[10, 29] The phase transformation behavior (see 2.1.1) changes with internal stress fields. Therefore, size, amount, volume and orientation of precipitates were directly correlated to the growth of oriented martensite variants.[33, 35] These studies have highlighted that the guidance of oriented martensite growth by precipitates and dislocation structures is the key-element for TWSME evolution, a fundamental understanding of the TWSME is still missing.

2.1.3 The indentation induced two-way shape memory effect

While the fundamental mechanisms causing the reversible two-way shape transformation remain unclear, recent research has identified a new mechanism for inducing the TWSME. Besides relatively complex treatments such as thermo-mechanical cycling or stress-assisted aging, severe plastic deformation, e.g. through indentation, can induce a reversible shape memory effect.[36]

Studies by Ni et al. have shown that a TWSME can already be induced by a single indentation, without repeated thermal cycling or subsequent heat treatment. The indentation depth in a NiTi-surface was shown to decrease or increase upon heating and cooling above and below the transformation temperature, respectively. Thus, after indentation the material elicit a reversible shape memory effect, i.e. a TWSME (Figure 2.6).[37]

Most of the decrease in indentation depth is related to the OWSME and occurs after heating the sample above A_f. After cooling the sample below M_f, the indent depth increases again, leading to a partially reverse deformation related to the TWSME. Upon thermal cycling, the depth of the indent can be changed reversibly. Lower indent depth is shown after heating and an increase is shown after cooling.

Based on these results, Zhang et al. proposed a technique to develop a reversible shape memory surface.[38-40] They indented NiTi alloys to high strains, thermally cycled them, and replanarized the samples by stepwise grinding and polishing (Figure 2.7). The multiple grinding and polishing steps were applied in order to remove the remaining indents and regain an optically smooth surface. When heated above A_f, the replanarized surface elicited semispherical surface protrusions at the former positions of the indents. These protrusions were thermally switchable and most likely induced by the residual dislocation structure oriented around the initial indent.

Hence, indentation of the surface leads to a surface form memory by means of a specific indentation and planarization technique. This method (indentation induced TWSME) leads to a thermally reversible surface topography which can be switched between a flat and structured state, depending on the initially applied deformation.

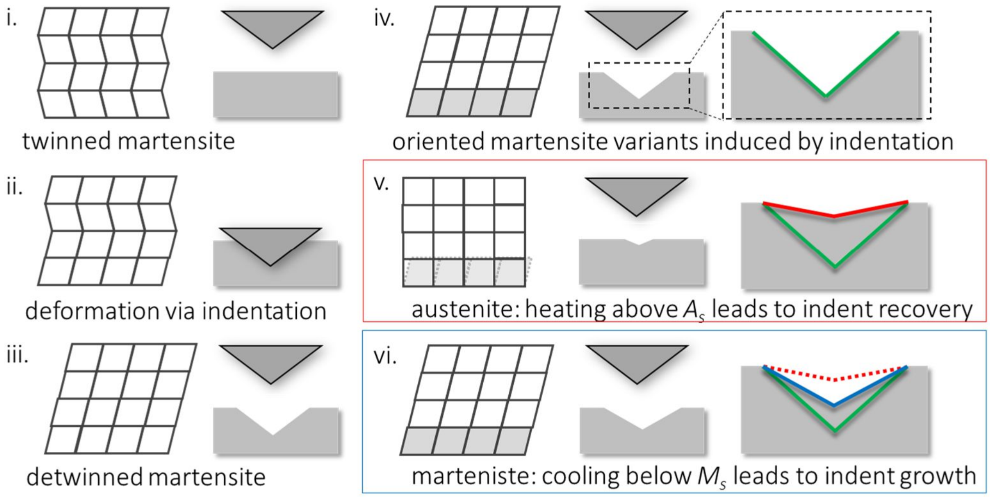

Figure 2.6: The indentation induced two-way shape memory effect. (i.-ii.) Twinned martensite is indented and plastically deformed. (iii.-iv.) The indentation induced stress leads to detwinning and stabilization of martensite variants with a preferred orientation. (v.) If the sample is heated the first time above A_f a recovery of the indent takes place. The depth of the initial indent profile (green) decreases with the austenitic transformation by the associated one-way shape memory effect. (vi.) After cooling the sample below M_f, the indentation depth increases (blue). A reverse shape change is shown within the martensitic transformation, which is related to the two-way shape memory effect. The profile depth can be changed reversibly by heating (red, v.) and cooling across the transformation temperatures (blue, vi.).

The microstructural mechanisms of the structure formation have not been identified in detail and a characterization of the interacting mechanisms of the structuring phenomena remains unclear. Likewise, the experimental parameters, which may enhance the structure formation and their role during martensite transformation, have not been identified in detail.

Current approaches used either single indentation or scratching to induce the deformation related stress field. The resulting remnant dislocation structure favors the nucleation of certain martensitic variants. The growth of these variants causes a shape change upon cooling and is thus thought to be responsible for the TWSME.[39] Based on this theory, Fei et al. tried to improve the recovery rate of the TWSME by shifting the quasistatic indentation conditions (Hertzian contact at low strain rates) to a dynamical regime by laser shock indentation (high strain rates).[41] They observed that the shape recovery was five times greater in laser shock indentation compared to quasistatic indentation. Accordingly, a higher protrusion size was achieved relative to the deformation depth induced by indentation.

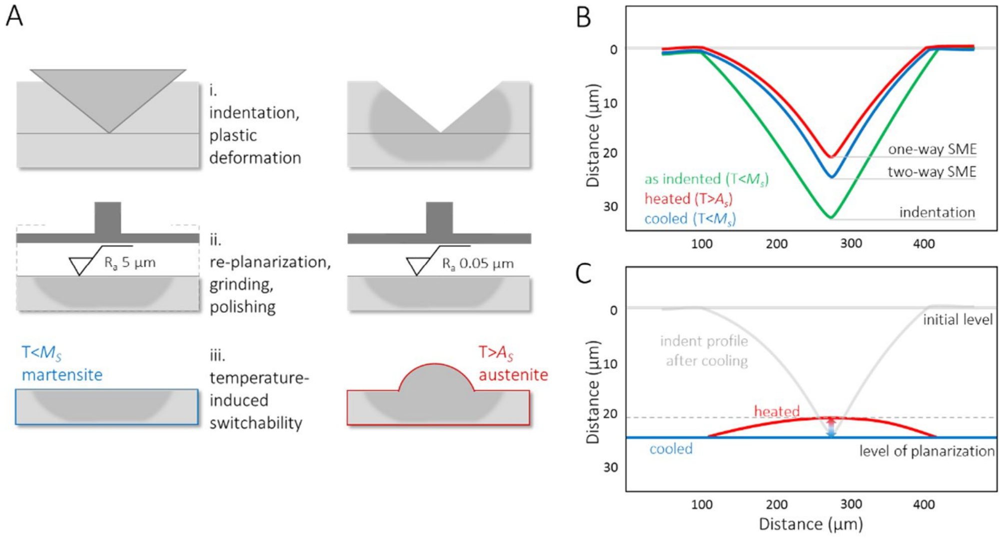

Figure 2.7: Illustration of the preparation steps for switchable surface topographies induced via surface indentation.(A, i) The surface of a NiTi shape memory alloy is plastically deformed by the indenter, leading to a remaining indent. (B) After heating and cooling the sample above and below the phase transformation temperatures a shallower indent profile (blue) remains on the surface due to the two-way shape memory effect. (A, ii) This indent is removed by grinding and subsequent polishing until an optically smooth surface is regained. (A, iii) When the sample is heated above A_f, a semispherical protrusion appears in the indented area and disappears again after cooling below M_f. (C) Thus, by successively heating and cooling the sample, the surface can be switched between flat and structured and vice versa.

2.1.4 Metal forming and structuring processes

The methods of surface texturing for metals range from macroscopic computer numerical controlled machining such as drilling,[42] over laser treatments[43] and lithographic technologies,[44] to micromachining using focused ion beam technology,[45] or electrochemical processes.[46] Preparation methods, in which the topography is formed serial and point-by-point, are significantly slower compared to parallel texturing, where the whole pattern is transferred at the same time such as in batch or roll-to-roll processes.

Apart from the study by Fei et al., where laser shock indentation was used to prepare switchable TWSME surfaces, all other studies used the same indentation based preparation technique presented by Zhang et al. (Figure 2.7). This technique is a rather complex and time consuming preparation routine.[38] Neither single indentation, nor stepwise planarization is an adequate technique for large-scale production of TWSME surfaces.

In order to select an appropriate machining technology for producing surfaces with switchable topographies on NiTi, the following requirements and specifications have to be considered:

- » The size of manufactured structures should range from nano- to millimeters, since usually surface functionalities are related to structures of such a size scale.
- » Preferably strong stress fields should be induced highly localized into the surface to promote the TWSME.
- » The amount of heat transfer into the work piece should be kept as low as possible in order to avoid any negative influence on the TWSME.
- » The process should enable an efficient parallel structuring of larger areas and already be applied or being applicable in industry.

2.1.5 Cold embossing

One of the most direct ways to induce a surface texture into a metal is the surface deformation through embossing or coining. A relatively coarse surface texture with several grooves of 5 to 20 μm in width can be used to improve lubrication for roller/piston in hydraulic motors as shown by Pettersson and Jacobson.[47] A specific diamond embossing tool was used to induce parallel or crossed grooves, with a 45°

rotation to the sliding direction on a steel piston.[47-49] With the increasing demand for miniaturization, the limits of these technologies were currently investigated. Geiger et al. summarized the developments in micro-metalforming and showed that especially the tool manufacturing limits the application for small-scale features.[50]

Böhm et al. showed that a structure size in the range of a few micrometers can be embossed into a surface with high accuracy (see Figure 2.8). In order to do so, high pressures exceeding the yield strength of the substrate material were applied. The samples were loaded with 2000 N for alumina and more than 5000 N for stainless steel. Subsequently, very high die wear or even failure of the brittle silicon dies was observed.[51]

Only little research has been carried out regarding the texturing of NiTi shape memory alloys through embossing. Hornbogen described a thermomechanical embossing process as the simplest way to determine the final shape formation in NiTi.[52] He clamped the martensitic material in a die and heated it high above A_f but below the recrystallization temperature. At temperatures above A_f the growth of nanometer scale precipitates, which then affect the martensitic transformation, was favored.

Bradley et al. patented the structuring of a shape memory sheet via embossing using an electromagnetic force-assisted imprint technology.[53-54] The features of the 'embossed shape memory sheet metal article' should be suitable for the generation of holographic images. The required surface features to gain a visible image is in the range of millimeters and is formed by an electromagnetic forming process. The authors preferred the use of thin foils for this process and applied a thermal treatment in form of heating and cooling during the electromagnetic forming.

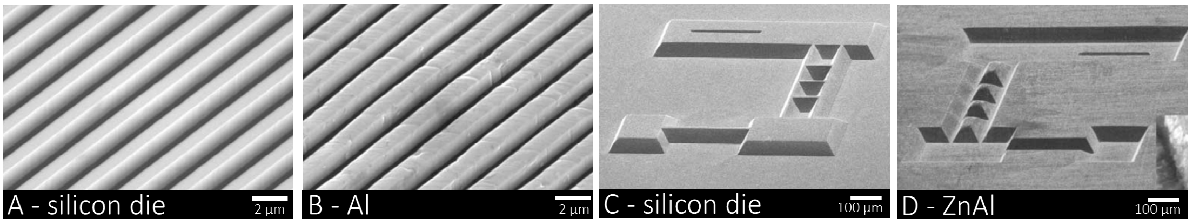

Figure 2.8: SEM images of metallic surfaces with complex micro-geometries fabricated via embossing. (A) Silicon die with straight grooves and a gap width of 1 µm. (B) Straight grooves on an alumina (Al99.5) substrate transferred with cold embossing. (C) Silicon die with a complex geometry. D, Complex surface structure transferred by superplastic embossing at 250°C for 12 min.[51]

Due to the specific stress-strain behavior and high degree of work hardening, in NiTi shape memory alloys, the embossing process leads to a poor structuring accuracy and high tool wear.[55] Various studies demonstrated the poor machinability of NiTi shape memory alloys using conventional machining such as cutting and drilling.[55-58] Thus, non-conventional techniques such as electrochemical machining are of growing interest to form NiTi devices.

2.1.6 Pulse electrochemical machining

Pulse electrochemical machining (PECM) is an extension of electrochemical machining (ECM), an electrolysis process without direct contact between tool and sample surface. As shown in Figure 2.9, a negative pattern of a tool is transferred onto a substrate by an anodic dissolution. During the process, a small gap between the sample and the cathode is maintained and flushed with an electrolyte at high flowrates. A high voltage is applied, leading to very high current densities. Heat production is avoided and residues of the manufacturing are removed from the interelectrode gap by a uniform flow of the electrolyte through a flushing chamber.[59] The pulse current leads to higher instant current densities and subsequently enables higher surface quality compared to electrochemical machining with continuous current.

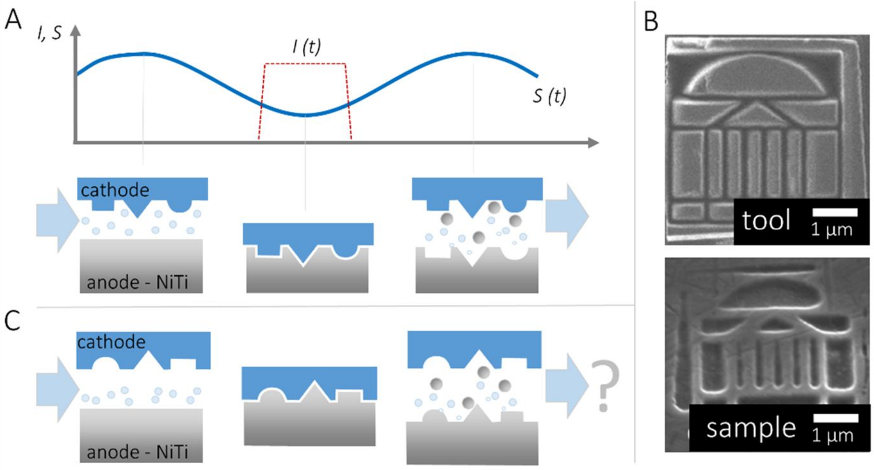

Figure 2.9: Schematic drawing of the PECM process and resulting surface texture. (A) The tool is moved upwards and downwards to widen the interelectrode gap (S, gap distance). A short pulse (I, current pulse) is applied at the lower turning point. Modified after [60]. (B) SEM images of a micro-machined tool and the structured Ni substrate.[61] (C) It has yet to be shown if protruding structures could also be manufactured by using a cathode with cavities of various geometries.

The tool (cathode) is moved in a sinusoidal manner upwards and downwards to widen the interelectrode gap (*S*, gap distance) between the substrate (anode) for the removal of oxides and trapped air in the electrolyte. A short pulse (*I*, current pulse) is applied at the lower turning point and induces the anodization of the sample, leading to an increased manufacturing accuracy. Rajurkar et al. mentioned that PECM is already applied to manufacture dies, turbine blades, and precision electronic components with an accuracy of 20 to 100 µm.[62-63]

Besides the advantages of a residual stress-free structure formation and low production of heat, the geometry of the structures and their accuracy is limited by the electrolytic flow. Hence a sophisticated design of the inverse tool geometry is required.[64]

In literature, most investigations on nonconventional machining of NiTi alloys focus on electropolishing for a highly accurate surface finish in biomedical applications or electro discharge machining (EDM) to structure implant surfaces of NiTi.[65-66] Both processes do not meet the requirements for the preparation of TWSME topographies, since electropolishing does not allow a formation extending surface structures and EDM, as a thermal process, interacts with the thermo-sensitive TWSME in NiTi. Only few investigations have focused on PECM processing of NiTi.[67-68]

2.1.7 Applications of two-way shape memory surfaces

In terms of potential applications of TWSME surfaces, little research has been conducted.[38] The recovery behavior of the indentation depth upon heating, which can be described as a self-healing property, has been studied for tribological applications by Ni et al.[69] Due to the recovery behavior of the OWSME, former indents and wear scars faded away upon heating. Because the hardness of NiTi was not high enough, the wear-induced material loss was prevented by coating the surface with a thin film of hard CrN. Using this strategy, wear resistant and self-healing tribological surfaces could be created.

Shaw et al. used the shape memory effect for high-density data storage. Data bits were stored by indentation and deleted by heating, due to the OWSME and the self-healing behavior of indents.[70-71]

Fei et al. showed that TWSME surfaces could also perform mechanical work with sufficient energy to induce localized plastic deformation in a strong base metal substrate. In planar contact, the formation of protrusions on a NiTi TWSME surface was able to deform stainless steel (304) under compressive loading. Considering that this process works robustly at the nanoscale, the authors emphasized its possible application in the field of MEMS micro assembly, nanolithography or thermally variable friction surfaces. [40]

The previously mentioned studies have focused on binary NiTi alloys, no research has been conducted on further alloys such as ternary or quaternary shape memory alloys. This could lead to different mechanical properties of the surface, enable increased actuation forces or the use of different external stimuli. A transfer of the indentation induced TWSME onto alloys with different phase transformation temperatures would enable an adaptation to the required activation temperatures. For example, an alloy with a phase transformation near body temperature could enable an activation of the TWSME by body heat, leading to new applications in biomedicine. Although not investigated in this thesis, a transfer of the TWSME topographies onto magnetic shape memory alloys could enable switching by a magnetic field.

2.2 Functional microstructures and microtopographies

Apart from the wear resistant coating on a TWSME surface,[69] no research has been carried out combining functional surface structures or other coatings with switchable topographies in NiTi. For many properties, the surface topography at micro- and nanometer scale plays an important role and induces macroscopic effects.[72] As schematically shown in Figure 2.10, functional coatings or micro- and nanostructures could influence effects, such as thermal radiation, wettability, reflectivity or friction and drag reduction.[47, 73-77]

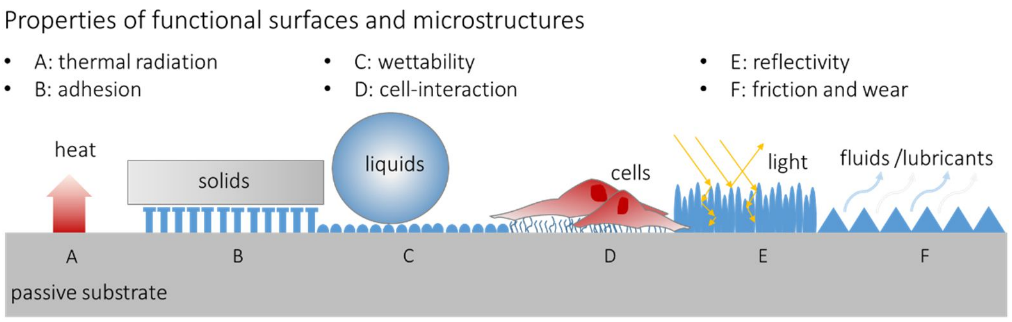

Figure 2.10: Schematic of different surface properties induced by the interaction of functional surface structures and coatings with external factors. The microtopography plays an important role for macroscopic effects such as (A) heat transfer,[73] (B) dry adhesion,[78] (C) superhydrophobicity,[74] (D) cell-response,[79] (E) anti-reflectivity[75-76] and (F) drag[80] as well as wear reduction.[47]

Microdroplets coupled with specific surface textures were used to promote spreading and evaporation for cooling in high heat flux MEMS.[73]

Many superhydrophobic surfaces were induced using microstructures mimicking the lotus-effect.[81] Lotus plants, possess hierarchically structured waxy crystals on their leaves, which lead to very little adhesion of water droplets to the surface.[74] Also anti-reflective coatings were mostly inspired by nature and make use of the interaction of light with different microstructures.[75-76] For example, nipple arrays, multilayer systems or microlense arrays in natural photonic structures induce optical effects such as reduced-reflectivity, structural colors or collection of light. [82-84] Other research showed that friction and drag could be reduced using scales and rib-like microstructures. [85] Such riblet surfaces, which were also found in shark skin, reduce turbulent skin friction if they are aligned parallel to the direction of flow.[80] Aircraft drag is shown to be reduced by up to 8% using a riblet foil.[86] Another example from nature using specific microtopographies to reduce friction is found in the skin of sandfishes and snakes.[87-89] Saw-tooth shaped ridges and bumps on the skin lead to a reduced friction coefficient and increased abrasion resistance, along the animals longitudinal axis and higher friction in the opposite direction. Thus, these nano-to microstructures provide friction anisotropy for locomotion. Recently, Greiner and Schäfer showed a reduction of dry sliding forces by more than 40% using such a bioinspired morphological surface texture.[89] They anticipate that these results could have a significant impact on all applications with dry sliding contacts. Other microstructures and topographies with a specific morphology were used to induce adhesive properties or to control cell-alignment on biomedical surfaces.[79, 90-91]

Accordingly, the combination of such functional surface structures with a TWSME surface or substrate material would enable control and switch the specific properties related to the surface structures by temperature.

2.2.1 Bioinspired dry adhesives and switchable adhesion

The ability of a surface to adhere to a substrate depends on chemical interaction, proximity and area of contact. The latter two are strongly influenced by surface topography. Inspired by the attachment devices of natural prototypes, such as spiders and geckos (see Figure 2.11), dry adhesives usually use functional microstructures to enhance van der Waals interactions in order to get robust adhesion on various surfaces.[92]

By the use of fibrillar structures, the contact area is split into many single contacts, the short-range Van-der-Waals forces are enhanced and adhesion is increased.[93] Kamperman et al. summarized different mechanisms interacting with the topography of the substrate to promote dry-adhesion by contact splitting (Figure 2.12).[90]

The hierarchical fibrils on the micro- and nanometer scale allow conformal contact with the substrate to increase adhesion.[93-94] The flexibility of the fibrillar structures enables enhanced adaptability to smooth, but also to rough, substrates.[95] Furthermore, the high number of separated contact elements leads to higher defect tolerance and redundancy.[96]

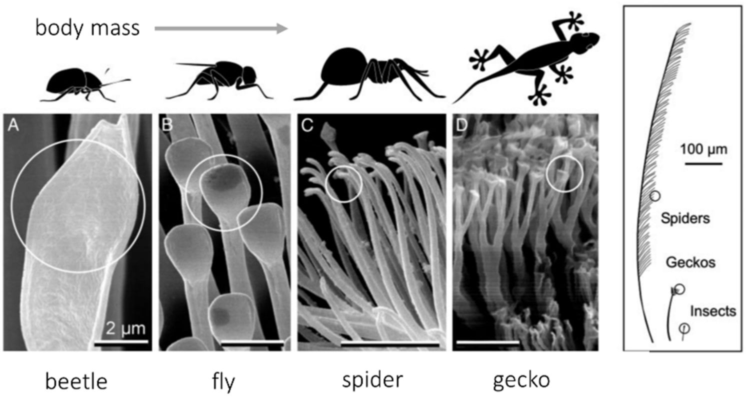

Figure 2.11: Terminal elements (circles) of hairy attachment pads in animals of different size. With increasing body weight, finer fibrillary structures to enhance adhesion are shown.[93]

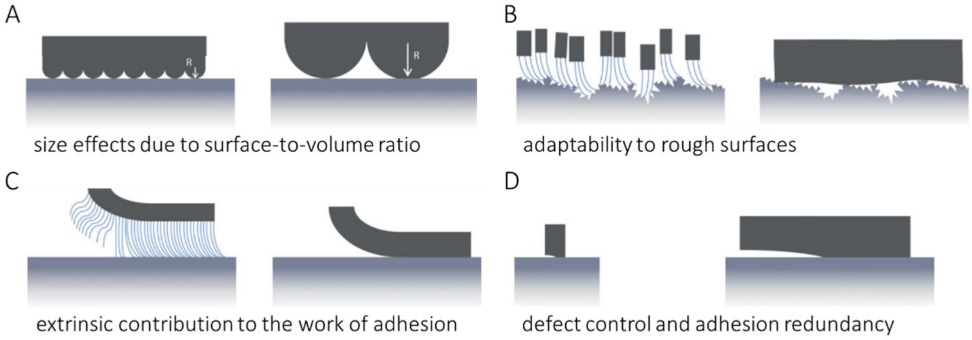

Figure 2.12: Schematic illustration of mechanisms, which enhance adhesion by contact splitting in fibrillary dry adhesive surfaces. (A) The reduced radius and increased number of contact elements induced a size effect enhancing the short-range van der Waals forces. (B) highly flexible features enable adaptability to rough topographies. (C) Increase in work of adhesion due to discontinuous crack propagation. (D) low susceptibility to interfacial defects. Modified after Kamperman et al. [90]

In the last decade, many different surface structures were developed as synthetic dry adhesives to benefit from nature's contact-splitting principle.[90, 97-98] Greiner et al. performed a systematic study on elastomeric pillars with a variation in aspect-ratio, tip shape, and backing layer thickness.[99-100] Fibrillar structures terminated with flanged ends, so called mushroom tips, received particular interest due to their strong adhesive behavior. The detachment of such bioinspired microstructures usually requires peeling or shear movements, which are difficult to adapt to industrial fabrication processes.

For industrial applications, the release from the substrate by detachment of the dry adhesive structures is as important as the increase in adhesion, to allow attachment. The ability to attach to, and detach from various surfaces without leaving residues or causing any mechanical damages is highly beneficial for many industry processes.

For example, in pick-and-place processes and for the handling of sensitive products, a reliable short time attachment is required. Thus, more recently, switchable adhesive systems have been developed.[101-106]

In many of these studies a change in topography leads to an increase or decrease in contact area, and subsequently, to a change in the adhesive performance (Figure 2.13). Northen et al. combined an adhesive polymer with magneto-sensitive Ni-cantilevers for reversible adhesion (Figure 2.13, A).[101] They applied a magnetic field to change the orientation of the cantilevers that induced a change in contact area and subsequently in adhesion. Their system showed excellent switchability, but the complicated fabrication process and the low adhesive strength limited its application. Reddy et al. used a temperature triggered thermoplastic elastomer in order to change the tilting angle of fibrils (Figure 2.13, B). Mechanical tilting of these structures led to an adhesion loss, and subsequent heating recovered the original orientation of the structures and by this the adhesive state.[102] A one-time switch in adhesion was possible, but no reversibility of the effect could be obtained. Kim et al. developed a mechanism based on a temporary, metastable contact for picking up and releasing small objects (Figure 2.13, C).[107] This system lacked active control in adhesion, which significantly limits the process reliability and maximum weight of the objects. Paretkar et al. presented a reversible pressure actuated adhesive system (Figure 2.13, D).[103] They triggered the loss in adhesion by mechanical loading, causing a reversible buckling and subsequent loss of intimate contact of the structures with the testing surface. Accordingly, when a threshold compressive load was applied to the fibrillar system, adhesion dropped significantly. In comparison to cylindrical structures, the mushroom structures required higher preload to force buckling. This is plausible, because their flanged ends increase contact adaptability.[108]

Other systems were triggered by light or humidity.[109-110] Boyne et al. found a reduction of peel strength dependent on light intensity and irradiation time in a pressure sensitive adhesive.[109] Humidity triggered the adhesion in porous polymer pads presented by Xue et al.[110] In the sponge-like structures adhesion increased due to a humidity-induced decrease in the elastic modulus of the polymer.

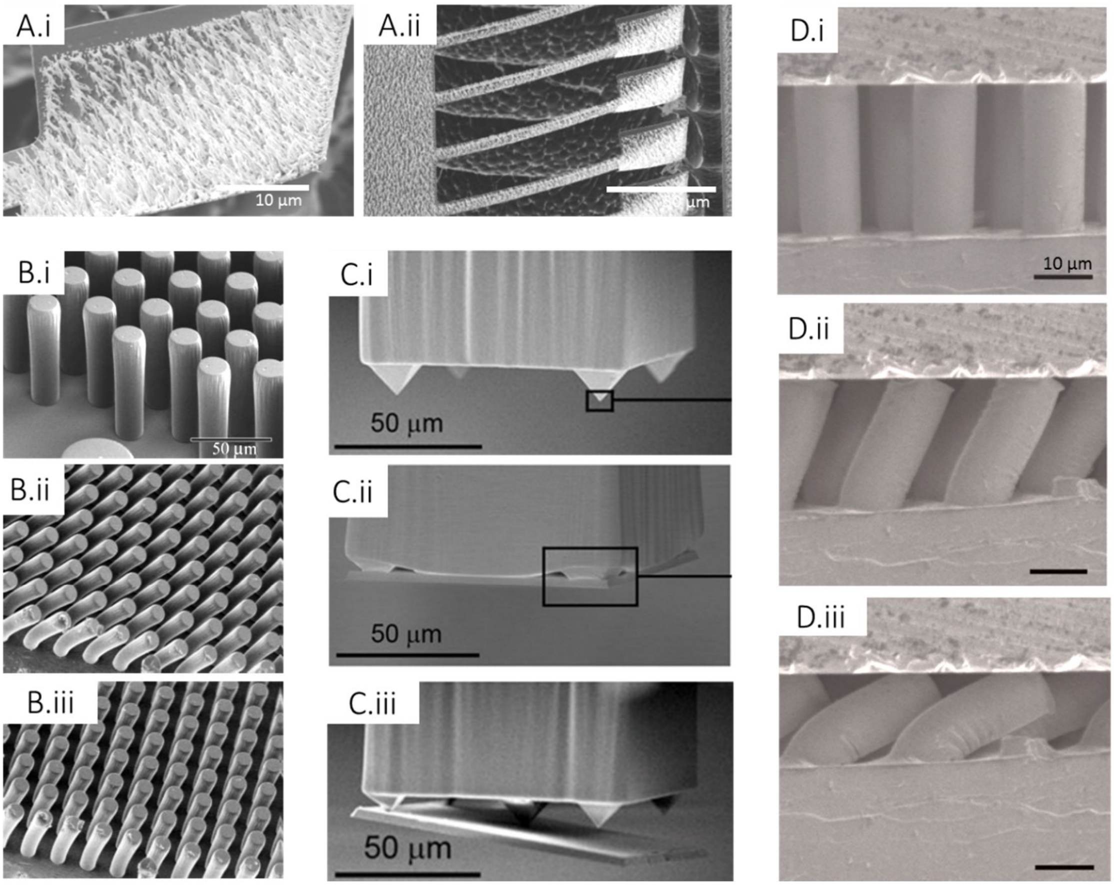

Figure 2.13: Overview on switchable adhesive systems. (A) Freestanding nickel cantilevers with paddles of nanorods for switchable adhesion stimulated using a magnetic field.[101] (B) Shape memory polymer pillars were bend and triggered by temperature to change contact area. (C) Elastomeric micropyramidal structures for use in assembly by transfer printing.[111] (D) Switching behavior due to bending and buckling of pillars.[112]

Most approaches in switchable adhesion induce a change of the adhesive structures themselves. Only few took advantage to change the shape or topography of the backing layer in order to switch adhesion (Figure 2.14).[105-106]

Xie et al. induced a peeling motion, analogue to the detachment movement in gecko toes, in a double layer system of a shape memory polymer with an elastomeric adhesive polymer. Due to a slight curvature of the shape memory polymer, the compliance to the substrate was reduced and the sample detached.

Jeong et al. presented a similar approach. They used the formation of wrinkles on a polymer sheet to misalign fibrillar adhesive structures positioned on top of the sheet.[106] By stretching the backing layer, the fibrils oriented in a normal direction to the surface of contact and, by relaxing the backing layer, the wrinkled topography led to misalignment with respect to the surface of contact. Thus, a control of adhesion in normal and shear direction was achieved.

2.2.2 Influence of (active) topographies on cells

The interface between tissue and an implant surface plays a crucial role during the integration and healing process in a body. Therefore, the cell-surface interaction of implant materials and different cell cultures has been investigated for years. Curtis and Varde showed, already in 1964, how the topography of an implant surface controls the interaction with cells and contributes positively to tissue repair.[113]

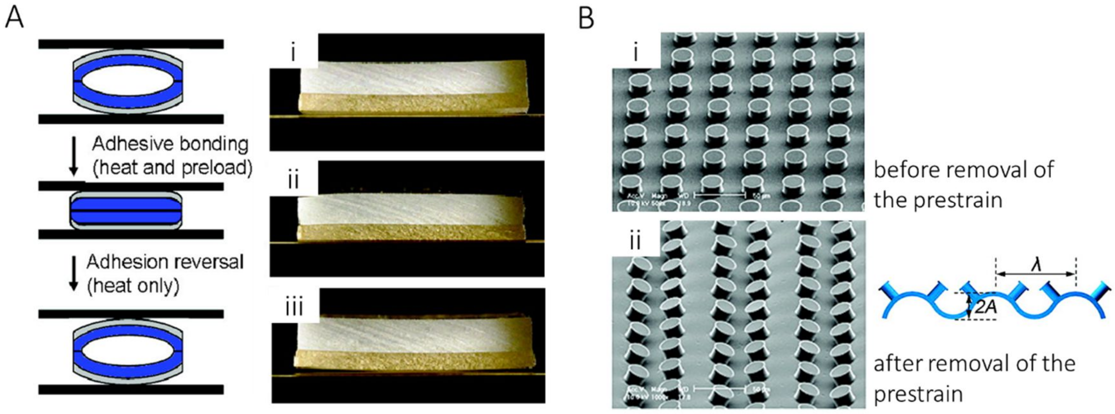

Figure 2.14: Two examples for switchable adhesives using a topographic change of the backing layer to control the area of contact to the substrate surface. (A) A self-peeling dry adhesive is build using a two layer composite with a dry adhesive layer and a shape memory polymer.[105] (B) Surface wrinkling was controlled by an applied strain. In the stretched state the pillars are in contact and adhesion increases, in the released state the pillars tilt and adhesion is reduced.[106]

Beside mechanical properties and surface chemistry, the substrate topography has a direct impact on cell-adhesion, orientation and activity.

Curtis and Wilkinson elaborated a remarkable overview on the topic of cell-topography interactions.[91] Starting with various types of topographies and cell reactions, their work covers the fundamentals and guides the reader up to therapies using cell-guiding topographies.[79, 91]

Fused silica is the most frequently used substrate material for the analysis of cell-topography interactions.[114] It can be structured using photolithography and reactive ion etching. In addition, the structured silica substrates can be used as a dye and mold for embossing and casting of polymer substrates. Both techniques enable a high accuracy of the reproduced structures.[115] Metallic substrates are structured by laser ablation, sandblasting or acid-etching, whereby the latter two lead to arbitrary surface structures.[116-117] Wilkinson et al. recommend to seed cells at least on 10 mm^2 of a structured substrate to obtain adequate statistics.[79]

Due to the strong correlation between preparation processes and surface chemistry, it is hardly distinguishable whether a cellular response comes from topography or chemistry. Britland et al. showed that topographic guidance overcomes chemical (adhesive) guidance for cells, if a minimum feature size is reached, although both aspects influence the cell orientation simultaneously.[118-119] The localization of extending cells along discontinuities and transition zones, such as chemical interfaces and geometric boundaries, has been consistently observed in numerous investigations.[91] The influence of topography was found to be more pronounced for features in the range of cell size. Geometric parameters that affect cell-response are: feature size, curvature radius, edges and step-size to groove width, and random roughness.

For example, cardiomyocytes, which aid tissue repair in heart disease, show a highly aligned cell growth in order to facilitate integration and contraction in living tissue. They align along grooves on a patterned substrate, if cultivated in vitro, which is close to the native myocardium.[120] The cells were found to grow with great alignment along grooves with a periodic distance from 2 to 4 µm.

An increase in the average surface roughness is correlated to an enhanced cytocompatibility in biomedical NiTi.[121] Zheng et al. used three different surface treatments, leading to an increase in average surface roughness (R_a) from 0.03 µm to 1.8 µm. With increasing roughness they observed a promoted cell proliferation.[122] Ponsonnet et al. showed higher proliferation of fibroblasts for NiTi samples if the roughness, which was defined in this study as the peak-to-valley roughness (R_z), is lower than 1 μm (Figure 2.15).

They conclude that the higher the roughness, the lower is the cell proliferation.[123] On the contrary, the surface with the highest roughness showed stronger alignment of the cells.[124] After 2h of culture onto a biomedical nickel-titanium alloy, NiTi80, with a R_z of ~5.8 μm, and NiTi2400 with R_z of ~0.5μm, the fibroblasts adhered to the substrate by cytoplasmic extensions and adapted to the roughness. After four days of culturing on NiTi400 with and R_z value of ~1.3 μm and NiTi2400, the cells were proliferated and aligned along the deeper grooves of the rougher surface.

So far, no guideline has been established for optimal surface design for biomedical devices. This is mainly due to the complex response behavior of different cells. The existence of an interaction between cells and topography has been confirmed, but 'how' they interact has yet to be explained. [119]

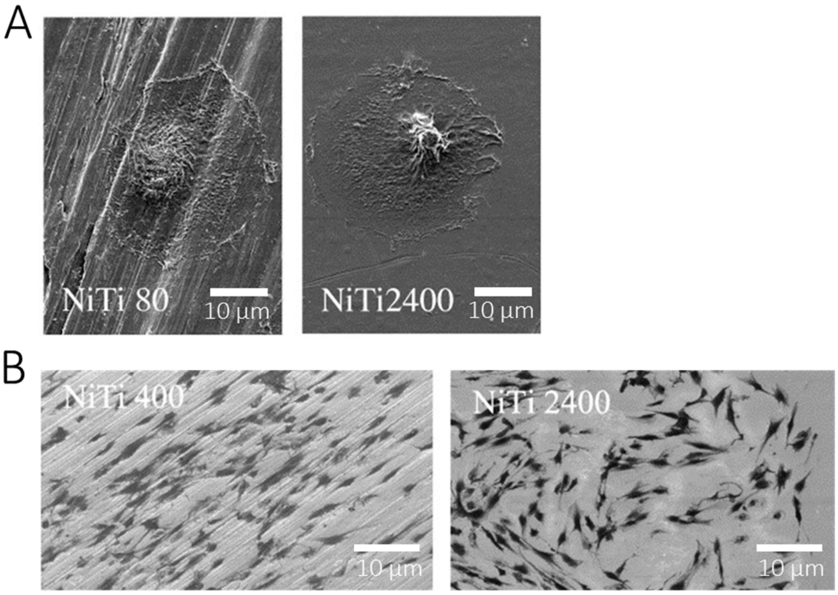

Figure 2.15: Effect of different surface roughness in NiTi on cell adhesion and orientation. (A) Cell attachment after 2h of culture onto a biomedical nickel-titanium alloy. (B) cell proliferation after four days of culture onto NiTi400 The cells were aligned along the deeper grooves of the rougher surface. Modified after Ponsonnet et al.[124]

The microenvironment of implant materials with growing tissue is highly dynamic. Therefore, the demands for modern implants go far beyond the mechanical support of damaged structures. In addition to the mechanical stability, biocompatibility, biodegradation, the possibility for medication and an active stimulation are in the focus of recent developments in biomedical research.

In particular, research in active implant materials has more recently emerged. Hereby, the main goal is the development of an implant with a dynamic switchable topography, which provides physiomechanical cues to guide cell growth in vitro or even in vivo. Active spatial control of cell-growth through switchable nano- and micropatterned substrates gives the opportunity to gain deeper insights into adhesion-mediated cell signaling and adds another dimension to the mechanobiology of the cells.[125-127] Most stimuli responsive substrates use humidity or temperature to induce a change in the materials chemical configuration, leading to a change in topography or a change in the molecular configuration of the interface.[128] As presented by Ebara et al., the use of polymeric shape memory surfaces is often restricted to a one-time change in topography, from a temporary state into a permanent state (Figure 2.16). For biomedical applications, the adaptation of phase transition temperatures of shape memory materials to physiological temperatures as well as constant and non-cytotoxic surface chemistry is an important challenge.[129]

Lam et al. presented a reconfigurable microtopography system without any significant changes in surface chemistry.[130] They used compression-induced buckling to form an undulated polymer surface. The wavy topography recovered to a flat surface by releasing the compressive strain and vice versa. The wavelength in the compressed state was around 5-7 µm and recovered to 0.6 µm without loading. This reversible change in topography was used to align and re-align myoblast cells, to promote an alignment for healthy muscosceletal genesis (Figure 2.17). This approach enabled reversible cell-alignment by material manipulation and compression. However, the mechanics of the material system limited the topography patterns to wavy geometries.

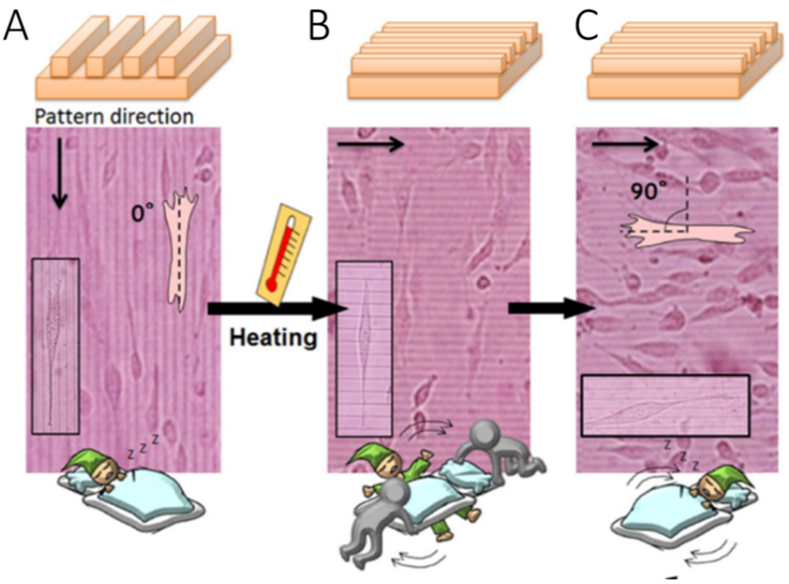

Figure 2.16: Shape memory surface for cell mechanobiology. Phase contrast images of fibroblasts seeded on a shape memory biopolymer (polycaprolactone). (A) The height of the temporal grooves was 300 nm. (B) For the surface shape memory experiment, cells were heat treated at 37 °C for 1h. After hating, the grooves show a 90° rotation. (C) Finally the cells were allowed to equilibrate at 32 °C for 48 h. After 36h 70% of the cells realigned with the permanent topography.[125]

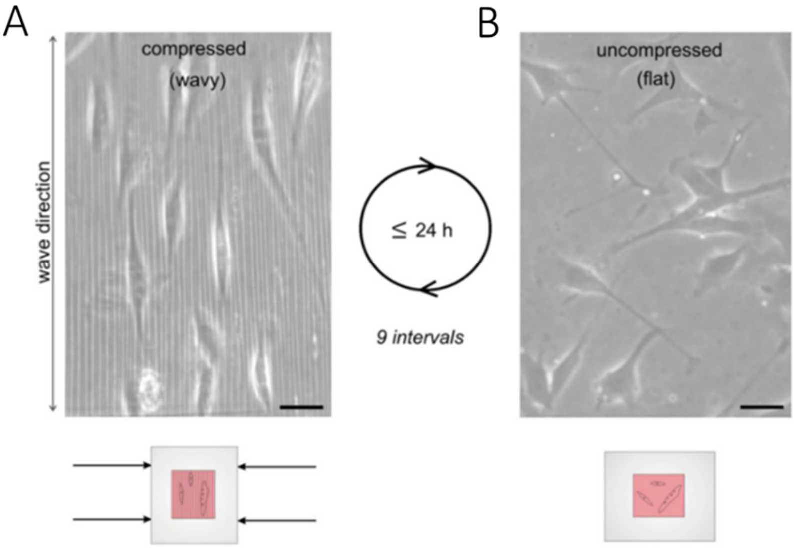

Figure 2.17: Optical microscopy images of muscle cells on the reversible wavy surface. (A) Cells aligned along the waves with an amplitude of 5-7 μm and (B) returned to random orientation on the flat surface within 24h. Scale bar 100 μm.[130]

Most investigations have focused on switchable topographies in single material systems. Switchable surface functions on metallic implant materials and metal-polymer hybrid systems can extend customization of an implant and promote fast integration into living tissue. Skorb and Andreeva already prognosticated the potential of such hybrid systems. Although their focus lies on surface functionalization by organic molecules, the combination of an alternating morphology of a responsive NiTi implant with an elastic biochemical surface layer is seen as a very promising.[128]

2.3 Motivation

In summary, only a few studies have focused on the indentation induced two-way shape memory effect in NiTi shape memory alloys. Most of these studies have investigated the extend and the reversibility of the TWSME by analyzing the indentation depth and protrusion height as a function of the cycling temperature and indentation parameter. However, no microstructural characterization was performed so far. Thus, the microstructural mechanisms behind the indentation induced TWSME remain unclear. Michutta et al. observed that during aging, the precipitates arrange in preferential orientations relative to the applied stress. They proposed that during the phase transformation the surrounding stress fields of the precipitates stimulate the growth of preferentially oriented martensite variants leading to a shape change upon cooling.[33] However, the influence of preexisting precipitates on the TWSME is still not very well understood and current models are based on cause-and-effect experimental relationships. Therefore, the effect of pre-existing Ti_3Ni_4 precipitates on the TWSME will be fundamentally investigated in this thesis. For this purpose the aging time will be systematically varied leading either to solutionized, semi-coherent, or incoherent precipitates. A detailed analysis of the two-way deformation recovery behavior of the differently heat-treated samples will give insight into the underlying microstructural mechanisms affecting the indentation induced TWSME and will pave the way for the creation of shape memory surfaces.

Apart from a study by Fei et al., previous studies used the same indentation preparation technique firstly proposed by Zhang et al., which is rather complex and time consuming.[38, 41] Neither single indentation, nor stepwise planarization is an adequate texturing technique for large scale training of switchable topographies. Therefore, two different sample preparation techniques are tested within the present work: Embossing and pulse electrochemical machining. Both processes are widely used in industry and if larger areas can be textured in a parallel manner, applications for switchable topographies using the TWSME may extend considerably.

Inducing switchable surface structures on shape memory alloys gives rise to a range of new applications, allowing for example the control of surface properties such as hydrophobicity and reflectivity, to name just a few. Apart from a wear resistant coating, no research has been carried out on the combination of metallic switchable topographies with other functional structures.[69] A reasonable combination of a TWSME surfaces with one or more functional microstructures in a hybrid system has a high synergetic potential. Existing functional surfaces with super-hydrophobic, (anti)-reflective, bioactive or (anti)adhesive properties might obtain additional functionality by the switchability of the TWSME, e.g. switchable adhesion or dynamic cell growth.

Therefore, the aims of this study are:

(i) *The investigation of the influence of pre-existing precipitates on the TWSME indentation induced TWSME. The effect of heat treatment and cycling temperature in order to enhance the size of switchable surface structures and increase the reversibility.*

(ii) *The development of large area texturing processes for the training of the two-way shape memory effect leading to switchable metallic topographies.*

(iii) *The combination of functional microstructures and switchable topographies based on the two-way shape memory effect - an approach to encounter new hybrid systems and temperature adaptation.*

2.4 References

1. Duerig, T.; Pelton, A.; Stöckel, D., An overview of nitinol medical applications. *Materials Science and Engineering: A* **1999,** *273*, 149-160.
2. Gill, J. J.; Ho, K.; Carman, G. P., Three-dimensional thin-film shape memory alloy microactuator with two-way effect. *Journal of Microelectromechanical Systems* **2002,** *11* (1), 68-77.
3. Bellouard, Y., Shape memory alloys for microsystems: A review from a material research perspective. *Materials Science and Engineering a-Structural Materials Properties Microstructure and Processing* **2008,** *481*, 582-589.
4. Otsuka, K.; Wayman, C. M., *Shape memory materials*. Cambridge university press: **1999**.
5. Buehler, W. J.; Gilfrich, J. V.; Wiley, R. C., Effect of Low-Temperature Phase Changes on the Mechanical Properties of Alloys near Composition TiNi. *Journal of Applied Physics* **1963,** *34* (5), 1475-1477.
6. Shaw, J. A.; Kyriakides, S., Thermomechanical aspects of NiTi. *Journal of the Mechanics and Physics of Solids* **1995,** *43* (8), 1243-1281.
7. Wever, D.; Veldhuizen, A.; De Vries, J.; Busscher, H.; Uges, D.; Van Horn, J., Electrochemical and surface characterization of a nickel–titanium alloy. *Biomaterials* **1998,** *19* (7), 761-769.
8. Shabalovskaya, S. A., On the nature of the biocompatibility and on medical applications of NiTi shape memory and superelastic alloys. *Bio-medical materials and engineering* **1995,** *6* (4), 267-289.
9. Bastin, G. F.; Rieck, G. D., Diffusion in the titanium-nickel system: I. occurrence and growth of the various intermetallic compounds. *Metallurgical Transactions* **1974,** *5* (8), 1817-1826.
10. Gall, K.; Sehitoglu, H.; Chumlyakov, Y. I.; Kireeva, I. V.; Maier, H. J., The influence of aging on critical transformation stress levels and martensite start temperatures in NiTi: Part I - Aged microstructure and micro-mechanical modeling. *Journal of Engineering Materials and Technology - Transactions of the ASME* **1999,** *121* (1), 19-27.
11. Tadaki, T.; Nakata, Y.; Shimizu, K. i.; Otsuka, K., Crystal structure, composition and morphology of a precipitate in an aged Ti-51 at% Ni shape memory alloy. *Transactions of the Japan institute of metals* **1986,** *27* (10), 731-740.
12. Tang, W.; Sundman, B.; Sandström, R.; Qiu, C., New modelling of the B2 phase and its associated martensitic transformation in the Ti–Ni system. *Acta Materialia* **1999,** *47* (12), 3457-3468.
13. Miyazaki, S.; Wayman, C. M., The R-phase transition and associated shape memory mechanism in Ti-Ni single crystals. *Acta Metallurgica* **1988,** *36* (1), 181-192.
14. Saburi, T.; Tatsumi, T.; Nenno, S., Effects of heat treatment on mechanical behavior of Ti-Ni alloys. *Le Journal de Physique Colloques* **1982,** *43* (C4), C4-261-C4-266.
15. Miyazaki, S.; Ohmi, Y.; Otsuka, K.; Suzuki, Y., Characteristics of deformation and transformation pseudoelasticity in Ti-Ni alloys. *Le Journal de Physique Colloques* **1982,** *43* (C4), C4-255-C4-260.
16. Miyazaki, S.; Otsuka, K., Deformation and transition behavior associated with theR-phase in Ti-Ni alloys. *Metallurgical Transactions A* **1986,** *17* (1), 53-63.
17. Frenzel, J.; George, E. P.; Dlouhy, A.; Somsen, C.; Wagner, M.-X.; Eggeler, G., Influence of Ni on martensitic phase transformations in NiTi shape memory alloys. *Acta Materialia* **2010,** *58* (9), 3444-3458.

18. Wollants, P.; De Bonte, M.; Roos, J., Thermodynamic analysis of the stress-induced martensitic-transformation in a single-crystal. *Zeitschrift fur metallkunde* **1979,** *70* (2), 113-117.
19. Otsuka, K.; Ren, X., Physical metallurgy of Ti-Ni-based shape memory alloys. *Progress in Materials Science* **2005,** *50* (5), 511-678.
20. Lagoudas, E. P. D. C.; Brinson, L. C.; Gao, X., Shape Memory Alloys—Part I: General Properties and Modeling of Single Crystals. **2004**.
21. Otsuka, K.; Kakeshita, T., Science and technology of shape-memory alloys: new developments. *MRS Bulletin* **2002,** *27* (02), 91-100.
22. Nagasawa, A.; Enami, K.; Ishino, Y.; Abe, Y.; Nenno, S., Reversible shape memory effect. *Scripta Metallurgica* **1974,** *8* (9), 1055-1060.
23. Perkins, J., Residual stresses and the origin of reversible (two-way) shape memory effects. *Scripta Metallurgica* **1974,** *8* (12), 1469-1476.
24. Van Humbeeck, J.; Chandrasekaran, M.; Delaey, L., Shape memory alloys: materials in action. *Endeavour* **1991,** *15* (4), 148-154.
25. Gall, K.; Maier, H. J., Cyclic deformation mechanisms in precipitated NiTi shape memory alloys. *Acta Materialia* **2002,** *50* (18), 4643-4657.
26. Lahoz, R.; Puertolas, J. A., Training and two-way shape memory in NiTi alloys: influence on thermal parameters. *Journal of Alloys and Compounds* **2004,** *381* (1-2), 130-136.
27. Favier, D.; Liu, Y., Restoration by rapid overheating of thermally stabilised martensite of NiTi shape memory alloys. *Journal of Alloys and Compounds* **2000,** *297* (1–2), 114-121.
28. Liu, Y.; Favier, D., Stabilisation of martensite due to shear deformation via variant reorientation in polycrystalline NiTi. *Acta Materialia* **2000,** *48* (13), 3489-3499.
29. Nishida, M.; Honma, T., All-round shape memory effect in Ni-rich TiNi alloys generated by constrained aging. *Scripta Metallurgica* **1984,** *18* (11), 1293-1298.
30. Miller, D. A.; Lagoudas, D. C., Influence of cold work and heat treatment on the shape memory effect and plastic strain development of NiTi. *Materials Science and Engineering a-Structural Materials Properties Microstructure and Processing* **2001,** *308* (1-2), 161-175.
31. Zhang, Y.; Cheng, Y.-T.; Grummon, D. S., Two-way indent depth recovery in a NiTi shape memory alloy. *Applied Physics Letters* **2006,** *88* (13), 131904-131904-3.
32. Gall, K.; Sehitoglu, H.; Chumlyakov, Y. I.; Kireeva, I. V., Tension–compression asymmetry of the stress–strain response in aged single crystal and polycrystalline NiTi. *Acta Materialia* **1999,** *47* (4), 1203-1217.
33. Michutta, J.; Somsen, C.; Yawny, A.; Dlouhy, A.; Eggeler, G., Elementary martensitic transformation processes in Ni-rich NiTi single crystals with Ni4Ti3 precipitates. *Acta Materialia* **2006,** *54* (13), 3525-3542.
34. Norfleet, D. M.; Sarosi, P. M.; Manchiraju, S.; Wagner, M. F. X.; Uchic, M. D.; Anderson, P. M.; Mills, M. J., Transformation-induced plasticity during pseudoelastic deformation in Ni–Ti microcrystals. *Acta Materialia* **2009,** *57* (12), 3549-3561.
35. Frick, C. P.; Ortega, A. M.; Tyber, J.; Maksound, A. E. M.; Maier, H. J.; Liu, Y. N.; Gall, K., Thermal processing of polycrystalline NiTi shape memory alloys. *Materials Science and Engineering a-Structural Materials Properties Microstructure and Processing* **2005,** *405* (1-2), 34-49.
36. Liu, Y.; McCormick, P., Factors influencing the development of two-way shape memory in NiTi. *Acta Metallurgica Et Materialia* **1990,** *38* (7), 1321-1326.

37. Ni, W.; Cheng, Y.-T.; Grummon, D. S., Recovery of microindents in a nickel–titanium shape-memory alloy: a "self-healing" effect. *Applied Physics Letters* **2002,** *80* (18), 3310-3312.
38. Zhang, Y.; Cheng, Y. T.; Grummon, D. S., Shape memory surfaces. *Applied Physics Letters* **2006,** *89*, 041912.
39. Zhang, Y. J.; Cheng, Y. T.; Grummon, D. S., Understanding indentation-induced two-way shape memory effect. *Journal of Materials Research* **2007,** *22* (10), 2851-2855.
40. Fei, X. L.; Zhang, Y. J.; Grummon, D. S.; Cheng, Y. T., Indentation-induced two-way shape memory surfaces. *Journal of Materials Research* **2009,** *24* (3), 823-830.
41. Fei, X.; Grummon, D. S.; Ye, C.; Cheng, G. J.; Cheng, Y.-T., Surface form memory in NiTi shape memory alloys by laser shock indentation. *Journal of Materials Science* **2012,** *47* (5), 2088-2094.
42. Altintas, Y., Manufacturing automation: metal cutting mechanics, machine tool vibrations, and CNC design. Cambridge university press: **2012.**
43. Bizi-Bandoki, P.; Benayoun, S.; Valette, S.; Beaugiraud, B.; Audouard, E., Modifications of roughness and wettability properties of metals induced by femtosecond laser treatment. *Applied Surface Science* **2011,** *257* (12), 5213-5218.
44. Vollertsen, F.; Niehoff, H. S.; Hu, Z., State of the art in micro forming. *International Journal of Machine Tools and Manufacture* **2006,** *46* (11), 1172-1179.
45. Reyntjens, S.; Puers, R., A review of focused ion beam applications in microsystem technology. *Journal of Micromechanics and Microengineering* **2001,** *11* (4), 287.
46. Schuster, R.; Kirchner, V.; Allongue, P.; Ertl, G., Electrochemical micromachining. *Science* **2000,** *289* (5476), 98-101.
47. Pettersson, U.; Jacobson, S., Textured surfaces for improved lubrication at high pressure and low sliding speed of roller/piston in hydraulic motors. *Tribology International* **2007,** *40* (2), 355-359.
48. Pettersson, U.; Jacobson, S., Influence of surface texture on boundary lubricated sliding contacts. *Tribology International* **2003,** *36* (11), 857-864.
49. Pettersson, U.; Jacobson, S., Tribological texturing of steel surfaces with a novel diamond embossing tool technique. *Tribology International* **2006,** *39* (7), 695-700.
50. Geiger, M.; Kleiner, M.; Eckstein, R.; Tiesler, N.; Engel, U., Microforming. *CIRP Annals-Manufacturing Technology* **2001,** *50* (2), 445-462.
51. Böhm, J.; Schubert, A.; Otto, T.; Burkhardt, T., Micro-metalforming with silicon dies. *Microsystem Technologies* **2001,** *7* (4), 191-195.
52. Hornbogen, E., Strengthening and embossment of final shape in NiTi shape memory alloys (SMA). *Advanced Engineering Materials* **2004,** *6* (4), 214-218.
53. Bradley, J. R.; Krajewski, P. E.; Cheng, Y. T. Embossed shape memory sheet metal article. US8266938B2, **2012.**
54. Hocheng, H.; Wen, T.-T., Electromagnetic force-assisted imprint technology for fabrication of submicron-structure. *Microelectronic engineering* **2008,** *85* (7), 1652-1657.
55. Weinert, K.; Petzoldt, V., Machining of NiTi based shape memory alloys. *Materials Science and Engineering: A* **2004,** *378* (1–2), 180-184.
56. Weinert, K.; Petzoldt, V., Machining NiTi micro-parts by micro-milling. *Materials Science and Engineering: A* **2008,** *481–482* (0), 672-675.
57. Lin, H.; Lin, K.; Chen, Y., A study on the machining characteristics of TiNi shape memory alloys. *Journal of Materials Processing Technology* **2000,** *105* (3), 327-332.
58. Wu, S.; Lin, H.; Chen, C., A study on the machinability of a Ti 49.6 Ni 50.4 shape memory alloy. *Materials Letters* **1999,** *40* (1), 27-32.

59. Bhattacharyya, B.; Munda, J.; Malapati, M., Advancement in electrochemical micro-machining. *International Journal of Machine Tools and Manufacture* **2004,** *44* (15), 1577-1589.
60. Weinmann, M., Elektrochemische Erzeugung dreidimensionaler Strukturen. **2015**.
61. Trimmer, A. L.; Hudson, J. L.; Kock, M.; Schuster, R., Single-step electrochemical machining of complex nanostructures with ultrashort voltage pulses. *Applied Physics Letters* **2003,** *82* (19), 3327-3329.
62. Kozak, J.; Rajurkar, K.; Wei, B., Modelling and analysis of pulse electrochemical machining (PECM). *Journal of Manufacturing Science and Engineering* **1994,** *116* (3), 316-323.
63. Rajurkar, K. P.; Zhu, D.; McGeough, J. A.; Kozak, J.; De Silva, A., New Developments in Electro-Chemical Machining. *CIRP Annals - Manufacturing Technology* **1999,** *48* (2), 567-579.
64. Weinmann, M.; Weber, O.; Bähre, D.; Munief, W.; Saumer, M.; Natter, H., Photolithography–Electroforming–Pulse Electrochemical Machining: An Innovative Process Chain for the High Precision and Reproducible Manufacturing of Complex Microstructures. *International Journal of Electrochemical Science* **2014,** *9*, 3917-3927.
65. Elahinia, M. H.; Hashemi, M.; Tabesh, M.; Bhaduri, S. B., Manufacturing and processing of NiTi implants: A review. *Progress in Materials Science* **2012,** *57* (5), 911-946.
66. Manjaiah, M.; Narendranath, S.; Basavarajappa, S., Review on non-conventional machining of shape memory alloys. *Transactions of Nonferrous Metals Society of China* **2014,** *24* (1), 12-21.
67. Lee, E.-S.; Shin, T.-H.; Kim, B.-K.; Baek, S.-Y., Investigation of short pulse electrochemical machining for groove process on Ni-Ti shape memory alloy. *International Journal of Precision Engineering and Manufacturing* **2010,** *11* (1), 113-118.
68. Maurer, J. J.; Hudson, J. L.; Fick, S. E.; Moffat, T. P.; Shaw, G. A., Electrochemical Micromachining of NiTi Shape Memory Alloys with Ultrashort Voltage Pulses. *Electrochemical and Solid-State Letters* **2011,** *15* (2), D8-D10.
69. Ni, W.; Cheng, Y.-T.; Grummon, D. S., Wear resistant self-healing tribological surfaces by using hard coatings on NiTi shape memory alloys. *Surface and Coatings Technology* **2006,** *201* (3), 1053-1057.
70. Shaw, G.; Stone, D.; Johnson, A.; Ellis, A.; Crone, W., Shape memory effect in nanoindentation of nickel–titanium thin films. *Applied Physics Letters* **2003,** *83* (2), 257-259.
71. Shaw, G. A.; Trethewey, J. S.; Johnson, A. D.; Drugan, W. J.; Crone, W. C., Thermomechanical High-Density Data Storage in a Metallic Material Via the Shape-Memory Effect. *Advanced Materials* **2005,** *17* (9), 1123-1127.
72. Assender, H.; Bliznyuk, V.; Porfyrakis, K., How Surface Topography Relates to Materials' Properties. *Science* **2002,** *297* (5583), 973-976.
73. Amon, C. H.; Yao, S.-C.; Wu, C.-F.; Hsieh, C.-C., Microelectromechanical system-based evaporative thermal management of high heat flux electronics. *Journal of heat transfer* **2005,** *127* (1), 66-75.
74. Barthlott, W.; Neinhuis, C., Purity of the sacred lotus, or escape from contamination in biological surfaces. *Planta* **1997,** *202* (1), 1-8.
75. Raut, H. K.; Ganesh, V. A.; Nair, A. S.; Ramakrishna, S., Anti-reflective coatings: A critical, in-depth review. *Energy & Environmental Science* **2011,** *4* (10), 3779-3804.

76. Vukusic, P.; Sambles, J. R., Photonic structures in biology. *Nature* **2003,** *424* (6950), 852-855.
77. Walsh, M. J., Riblets as a viscous drag reduction technique. *AIAA journal* **1983,** *21* (4), 485-486.
78. del Campo, A.; Greiner, C.; Arzt, E., Contact Shape Controls Adhesion of Bioinspired Fibrillar Surfaces. *Langmuir* **2007,** *23* (20), 10235-10243.
79. Wilkinson, C.; Riehle, M.; Wood, M.; Gallagher, J.; Curtis, A., The use of materials patterned on a nano-and micro-metric scale in cellular engineering. *Materials Science and Engineering: C* **2002,** *19* (1), 263-269.
80. Bechert, D.; Hoppe, G.; Reif, W., On the drag reduction of the shark skin. *AIAA paper* **1985,** *85*, 0546.
81. Fürstner, R.; Barthlott, W.; Neinhuis, C.; Walzel, P., Wetting and self-cleaning properties of artificial superhydrophobic surfaces. *Langmuir* **2005,** *21* (3), 956-961.
82. Parker, A. R.; Hegedus, Z.; Watts, R. A., Solar–absorber antireflector on the eye of an Eocene fly (45 Ma). *Proceedings of the Royal Society of London B: Biological Sciences* **1998,** *265* (1398), 811-815.
83. Vukusic, P.; Sambles, J.; Lawrence, C.; Wootton, R., Quantified interference and diffraction in single Morpho butterfly scales. *Proceedings of the Royal Society of London B: Biological Sciences* **1999,** *266* (1427), 1403-1411.
84. Aizenberg, J.; Tkachenko, A.; Weiner, S.; Addadi, L.; Hendler, G., Calcitic microlenses as part of the photoreceptor system in brittlestars. *Nature* **2001,** *412* (6849), 819-822.
85. Bechert, D.; Bruse, M.; Hage, W.; Van der Hoeven, J. T.; Hoppe, G., Experiments on drag-reducing surfaces and their optimization with an adjustable geometry. *Journal of Fluid Mechanics* **1997,** *338*, 59-87.
86. Ball, P., Engineering shark skin and other solutions. *Nature* **1999,** *400* (6744), 507-509.
87. Rechenberg, I.; El Khyari, A. R., Reibung und Verschleiß am Sandfisch der Sahara. Bericht zum beglegitenden Forschungsvorhaben im Rahmen des Festo-Stipendiums für Herrn AR El Khyari, TU Berlin **2004**.
88. Baumgartner, W.; Saxe, F.; Weth, A.; Hajas, D.; Sigumonrong, D.; Emmerlich, J.; Singheiser, M.; Böhme, W.; Schneider, J. M., The sandfish's skin: morphology, chemistry and reconstruction. *Journal of bionic engineering* **2007,** *4* (1), 1-9.
89. Greiner, C.; Schäfer, M., Bio-inspired scale-like surface textures and their tribological properties. *Bioinspiration & Biomimetics* **2015,** *10* (4), 044001.
90. Kamperman, M.; Kroner, E.; del Campo, A.; McMeeking, R. M.; Arzt, E., Functional adhesive surfaces with “gecko” effect: the concept of contact splitting. *Advanced Engineering Materials* **2010,** *12* (5), 335-348.
91. Curtis, A.; Wilkinson, C., Topographical control of cells. *Biomaterials* **1997,** *18* (24), 1573-1583.
92. Autumn, K.; Liang, Y. A.; Hsieh, S. T.; Zesch, W.; Chan, W. P.; Kenny, T. W.; Fearing, R.; Full, R. J., Adhesive force of a single gecko foot-hair. *Nature* **2000,** *405* (6787), 681-685.
93. Arzt, E.; Gorb, S.; Spolenak, R., From micro to nano contacts in biological attachment devices. *Proceedings of the National Academy of Sciences* **2003,** *100* (19), 10603-10606.
94. Arzt, E.; Enders, S.; Gorb, S., Towards a micromechanical understanding of biological surface devices. *Zeitschrift fur metallkunde* **2002,** *93* (5), 345-351.

95. Persson, B.; Gorb, S., The effect of surface roughness on the adhesion of elastic plates with application to biological systems. *The Journal of chemical physics* **2003,** *119* (21), 11437-11444.
96. McMeeking, R. M.; Arzt, E.; Evans, A. G., Defect dependent adhesion of fibrillar surfaces. *The Journal of Adhesion* **2008,** *84* (7), 675-681.
97. Boesel, L. F.; Greiner, C.; Arzt, E.; del Campo, A., Gecko-Inspired Surfaces: A Path to Strong and Reversible Dry Adhesives. *Advanced Materials* **2010,** *22* (19), 2125-2137.
98. Del Campo, A.; Arzt, E., Design parameters and current fabrication approaches for developing bioinspired dry adhesives. *Macromolecular bioscience* **2007,** *7* (2), 118-127.
99. Greiner, C.; del Campo, A.; Arzt, E., Adhesion of Bioinspired Micropatterned Surfaces: Effects of Pillar Radius, Aspect Ratio, and Preload. *Langmuir* **2007,** *23* (7), 3495-3502.
100. Greiner, C.; Spolenak, R.; Arzt, E., Adhesion design maps for fibrillar adhesives: the effect of shape. *Acta Biomaterialia* **2009,** *5* (2), 597-606.
101. Northen, M. T.; Greiner, C.; Arzt, E.; Turner, K. L., A Gecko-Inspired Reversible Adhesive. *Advanced Materials* **2008,** *20* (20), 3905-3909.
102. Reddy, S.; Arzt, E.; del Campo, A., Bioinspired Surfaces with Switchable Adhesion. *Advanced Materials* **2007,** *19* (22), 3833-3837.
103. Paretkar, D.; Kamperman, M.; Schneider, A. S.; Martina, D.; Creton, C.; Arzt, E., Bioinspired pressure actuated adhesive system. *Materials Science and Engineering: C* **2011,** *31* (6), 1152-1159.
104. Kim, S.; Sitti, M.; Xie, T.; Xiao, X., Reversible dry micro-fibrillar adhesives with thermally controllable adhesion. *Soft Matter* **2009,** *5* (19), 3689-3693.
105. Xie, T.; Xiao, X., Self-Peeling Reversible Dry Adhesive System. *Chemistry of Materials* **2008,** *20* (9), 2866-2868.
106. Jeong, H. E.; Kwak, M. K.; Suh, K. Y., Stretchable, Adhesion-Tunable Dry Adhesive by Surface Wrinkling. *Langmuir* **2010,** *26* (4), 2223-2226.
107. Kim, S.; Carlson, A.; Cheng, H.; Lee, S.; Park, J.-K.; Huang, Y.; Rogers, J. A., Enhanced adhesion with pedestal-shaped elastomeric stamps for transfer printing. *Applied Physics Letters* **2012,** *100* (17), 171909.
108. Paretkar, D.; Kamperman, M.; Martina, D.; Zhao, J.; Creton, C.; Lindner, A.; Jagota, A.; McMeeking, R.; Arzt, E., Preload-responsive adhesion: effects of aspect ratio, tip shape and alignment. *Journal of The Royal Society Interface* **2013,** *10* (83), 20130171.
109. Boyne, J.; Millan, E.; Webster, I., Peeling performance of a novel light switchable pressure-sensitive adhesive. *International Journal of Adhesion and Adhesives* **2001,** *21* (1), 49-53.
110. Xue, L.; Kovalev, A.; Dening, K.; Eichler-Volf, A.; Eickmeier, H.; Haase, M.; Enke, D.; Steinhart, M.; Gorb, S. N., Reversible adhesion switching of porous fibrillar adhesive pads by humidity. *Nano letters* **2013,** *13* (11), 5541-5548.
111. Kim, S.; Wu, J.; Carlson, A.; Jin, S. H.; Kovalsky, A.; Glass, P.; Liu, Z.; Ahmed, N.; Elgan, S. L.; Chen, W.; Ferreira, P. M.; Sitti, M.; Huang, Y.; Rogers, J. A., Microstructured elastomeric surfaces with reversible adhesion and examples of their use in deterministic assembly by transfer printing. *Proceedings of the National Academy of Sciences* **2010,** *107* (40), 17095-17100.
112. Paretkar, D.; Schneider, A. S.; Kroner, E.; Arzt, E., In situ observation of contact mechanisms in bioinspired adhesives at high magnification. *MRS Communications* **2011,** *1* (01), 53-56.

113. Curtis, A.; Varde, M., Control of cell behavior: topological factors. *Journal of the National Cancer Institute* **1964,** *33* (1), 15-26.
114. Nikkhah, M.; Edalat, F.; Manoucheri, S.; Khademhosseini, A., Engineering microscale topographies to control the cell–substrate interface. *Biomaterials* **2012,** *33* (21), 5230-5246.
115. Wòjciak, B.; Crossan, J.; Curtis, A. S. G.; Wilkinson, C. D. W., Grooved substrata facilitate in vitro healing of completely divided flexor tendons. *Journal of Materials Science: Materials in Medicine* **1995,** *6* (5), 266-271.
116. Li, D.; Ferguson, S. J.; Beutler, T.; Cochran, D. L.; Sittig, C.; Hirt, H. P.; Buser, D., Biomechanical comparison of the sandblasted and acid-etched and the machined and acid-etched titanium surface for dental implants. *Journal of Biomedical Materials Research* **2002,** *60* (2), 325-332.
117. Miller, P.; Aggarwal, R.; Doraiswamy, A.; Lin, Y.; Lee, Y.-S.; Narayan, R., Laser micromachining for biomedical applications. *Jom* **2009,** *61* (9), 35-40.
118. Britland, S.; Morgan, H.; Wojiak-Stodart, B.; Riehle, M.; Curtis, A.; Wilkinson, C., Synergistic and Hierarchical Adhesive and Topographic Guidance of BHK Cells. *Experimental Cell Research* **1996,** *228* (2), 313-325.
119. Ventre, M.; Natale, C. F.; Rianna, C.; Netti, P. A., Topographic cell instructive patterns to control cell adhesion, polarization and migration. *Journal of The Royal Society Interface* **2014,** *11* (100).
120. Kiefer, K.; Lee, J.; Haidar, A.; Miró, M. M.; Akkan, C. K.; Veith, M.; Aktas, O. C.; Abdul-Khaliq, H., Alignment of human cardiomyocytes on laser patterned biphasic core/shell nanowire assemblies. *Nanotechnology* **2014,** *25* (49), 495101.
121. Samaroo, H. D.; Lu, J.; Webster, T. J., Enhanced endothelial cell density on NiTi surfaces with sub-micron to nanometer roughness. *International journal of nanomedicine* **2008,** *3* (1), 75.
122. Zheng, C. Y.; Nie, F. L.; Zheng, Y. F.; Cheng, Y.; Wei, S. C.; Valiev, R. Z., Enhanced in vitro biocompatibility of ultrafine-grained biomedical NiTi alloy with microporous surface. *Applied Surface Science* **2011,** *257* (21), 9086-9093.
123. Ponsonnet, L.; Reybier, K.; Jaffrezic, N.; Comte, V.; Lagneau, C.; Lissac, M.; Martelet, C., Relationship between surface properties (roughness, wettability) of titanium and titanium alloys and cell behaviour. *Materials Science and Engineering: C* **2003,** *23* (4), 551-560.
124. Ponsonnet, L.; Comte, V.; Othmane, A.; Lagneau, C.; Charbonnier, M.; Lissac, M.; Jaffrezic, N., Effect of surface topography and chemistry on adhesion, orientation and growth of fibroblasts on nickel–titanium substrates. *Materials Science and Engineering: C* **2002,** *21* (1), 157-165.
125. Ebara, M., Shape-memory surfaces for cell mechanobiology. *Science and Technology of Advanced Materials* **2015,** *16* (1), 014804.
126. Hook, A. L.; Voelcker, N. H.; Thissen, H., Patterned and switchable surfaces for biomolecular manipulation. *Acta Biomaterialia* **2009,** *5* (7), 2350-2370.
127. Greco, F.; Mattoli, V., Introduction to active smart materials for biomedical applications. In *Piezoelectric Nanomaterials for Biomedical Applications*, Springer: **2012**, pp 1-27.
128. Skorb, E. V.; Andreeva, D. V., Surface Nanoarchitecture for Bio-Applications: Self-Regulating Intelligent Interfaces. *Advanced Functional Materials* **2013,** *23* (36), 4483-4506.
129. Ebara, M.; Uto, K.; Idota, N.; Hoffman, J. M.; Aoyagi, T., Shape-Memory Surface with Dynamically Tunable Nano-Geometry Activated by Body Heat. *Advanced Materials* **2012,** *24* (2), 273-278.

130. Lam, M. T.; Clem, W. C.; Takayama, S., Reversible on-demand cell alignment using reconfigurable microtopography. *Biomaterials* **2008,** *29* (11), 1705-1712.

Chapter 3

Vickers indentation induced one-way and two-way shape memory effect in austenitic NiTi

Abstract - In this study, the indentation induced shape memory effect was used to create reversible protrusions on the material surface. In the austenitic nickel-titanium alloy, the shape memory behavior was investigated after Vickers indentations followed by planarization and temperature cycling. Heavily cold-drawn Ti-50.9 at.% Ni was either solutionized at 700 °C for 1.5 h or aged at 550 °C for 1.5 h. The surfaces of both variants were indented at loads ranging from 20 N to 200 N. The depth recovery ratio of the indents as well as the formation of protrusions on the surface after a re-planarization through grinding and polishing were analyzed as a function of temperature cycling above and below the phase transformation temperatures using white light interferometry. For characterization, differential scanning calorimetry, x-ray and electron backscatter diffraction, and transmission electron microscopy were employed. In the aged material, both a one-way and two-way shape memory effect were found, whereas, the solutionized sample showed a much smaller one-way and no measureable two-way shape recovery. This phenomenon is discussed in terms of martensite stabilization as observed by in situ heating transmission electron microscopy experiments.

This chapter was published in *Advanced Engineering Materials (2014), 16, 72-79.*[1]

3.1 Introduction

Nickel–titanium (NiTi) alloys are the subject of continued research due to their unique shape recovery properties. This shape memory behavior has been exploited in several fields, including biomedical devices,[2-4] civil structures,[5-7] and micro-electromechanical systems (MEMS).[8-10] The shape memory effect (SME) in NiTi is attributed to a diffusionless stress-induced martensitic phase transformation.[11-12] Relative to the phase transformation temperature NiTi deforms by martensite reorientation at low temperatures, stress-induced martensite transformation at intermediate temperatures, and plastic slip at high temperatures.[13-14] After low/intermediate temperature deformation, heating above the austenite finish temperature allows the stress-induced martensite (B19') structure to transform back into austenite (B2), thereby fully recovering the deformation. This process is referred to as the one-way shape memory effect (OWSME). By a combination of deformation processing and heat treatment, the material may be trained to elicit a two-way shape memory effect (TWSME). This effect is characterized by the alloy's memorization of both a high and low temperature shape, allowing a spontaneous change between the two shapes as a function of cycling temperature.

The three main conventional techniques used to elicit the TWSME involve: (i.) severe deformation below the martensite start temperature (M_s), e.g.[15-18], (ii.) some form of thermomechanical cycling, e.g. [19-23] and (iii.) stress-assisted aging, e.g.[24-27]. These techniques have in common that they lead to an internal stress state, which biases martensite formation of preferential orientation, thereby leading to recoverable deformation.

Recently it was shown by Zhang et al.[28-31] that indentation without repeated thermal cycling or subsequent heat treatment is capable of inducing the TWSME on the sample surface. In addition, it was shown that post-indentation grinding and polishing of the sample to form a planarized surface allowed the surface topography to be thermally switched between a patterned and a flat state. Such thermally switchable surface structures open the realm for many exciting potential functionalities, e.g. for variable tribological or self-cleaning applications. The protrusions were hypothesized to be caused by preferentially-oriented dislocation structures remaining underneath and around the indentation site after planarization.[28] Such dislocations would elicit prescribed martensite variants to form upon thermal cycling. While this explanation is reasonable as the test temperature (RT) was below M_s, direct characterization of the microstructure to visualize either the dislocation arrangement or the martensite variants formed during indentation is still lacking. Furthermore, testing was limited to spherical indenters and equiatomic composition of the NiTi alloy, leaving the effects of indenter shape and phase composition unexplored.

In this paper, we demonstrate that a TWSME and thus switchable micropatterned surfaces can also be obtained if predominantly austenitic NiTi is trained by Vickers indentation. The NiTi alloy chosen for this study is slightly nickel-rich, which allows for heat treatment to create Ti_3Ni_4 precipitates known to influence the SME.[13, 32-33] The internal stress associated with these coherent precipitates has been shown to increase the phase transformation temperatures.[34-35] This makes both austenite and martensite stable at room temperature, which has the distinct advantage that both the flat surface and the protrusions are stable under ambient conditions. Furthermore, the coherency stress associated with the precipitates can be tailored to optimize the TWSME surface by deriving a better understanding of the underlying microstructural mechanisms influencing the phase transformation.

3.2 Experimental

The material used in this study was a commercial polycrystalline alloy with a nominal composition of Ti- 50.9 at% Ni (Ti-55.7wt% Ni). The initial melt was poured into a cylindrical steel mold under vacuum and allowed to solidify. The ingot was then sectioned, and hot-rolled at temperatures between 845 °C and 955 °C. Subsequently, the bar was heavily cold-drawn by approximately 30%. Several samples were machined from this bar by electro-discharge and used as the as-received material in this study. Initial microstructure and mechanical behavior of the cold-drawn material have been thoroughly characterized in previous work.[35]

To investigate the effect of microstructure on the shape memory behavior, two different heat treatments were applied to the cold-drawn samples. One sample was heat treated at 550 °C for 1.5 h (referred to as the 'aged' sample) and the other one solutionized at 700 °C for 1.5 h (referred to as the 'solutionized' sample). Both samples were quenched in water to room temperature and cut into pieces with a rectangular cross-section, where the long axis was parallel to the drawing direction. The final dimensions of the samples were approximately 5 mm x 5 mm x 24 mm. For the indentation experiments, the sample surfaces perpendicular to the drawing direction were prepared by grinding down to 2400 grade SiC paper, followed by electropolishing with a solution composed of 20 vol% H2SO4 and 80 vol% methanol at a voltage of 8 V for 30 s.

Vickers indentation was performed on a LecoV-100 indenter at room temperature. Loads of 20 N, 100 N, and 200 N were applied and then held for 10 s before unloading. For each load, indents were made in 3 x 3 matrices with a spacing of approximately twice the indent width. Cross-sectional profiles of the indents were obtained after initial indentation at room temperature, after heating to 80 °C, and after cooling with liquid nitrogen, using a ZygoNewView 5000 white-light interferometer (WLI). To assess the cyclic reversibility of the temperature-induced topographical changes, three further heating and cooling cycles were applied to both samples. Profiles of the indents were recorded after each cycle. The indents were removed by carefully grinding the samples after cooling. In order to avoid artifacts from the damage layer induced by the grinding, an additional electropolishing step with the same solution and parameters as for the initial material was applied to the sample surface. The precise depth of the removed material was a function of the indentation depth, with the aim to result in a flat surface. The root mean squared value of surface roughness (R_{ms}) after electropolishing was approximately 70 nm as determined by the WLI. After planarization, the samples were subjected to the same temperature cycles as previously described, and the resulting surface morphologies were characterized using the WLI.

The phase transformation temperatures of the solutionized and aged samples were measured by differential scanning calorimetry (DSC) at a heating/cooling rate of 20 Kmin^{-1} using a Mettler Toledo DSC1 Star System. For these experiments, small pieces with masses of approximately 10 g –20 g were machined from the bulk samples and subsequently mechanically polished and electrochemically etched to remove the surface damage layer.

The microstructure of the NiTi samples was analyzed through a combination of X-ray diffraction and electron microscopy. The X-ray diffraction patterns were recorded with Θ/2Θ scans using a Bruker AXS D8 X-ray diffractometer (XRD) to determine the phase composition. Identification of the phases was achieved by comparing the sample diffractograms with the International Center for Diffraction Database (ICDD). For the aged sample the fractions of the phases were further analyzed by electron backscatter diffraction (EBSD) using a JEOL JSM 7000F scanning electron microscope (SEM) equipped with an EDAX detector for Kikuchi patterns at a voltage of 20 kV and a working distance of 15 mm. The data was collected with a step size of 50 nm and then analyzed with the TSL software unit. In addition, the microstructure was characterized with a Philips CM200 transmission electron microscope (TEM). Electron transparent samples were obtained by grinding discs of the differently treated alloys with a diameter of 3 mm to a final thickness of 50 μm and subsequent twin-jet polishing at 20 V using the same electrolyte as for the electropolishing. In order to characterize the mechanisms responsible for the TWSME, a TEM lamella was machined with a focus ion beam (FIB) from the material underneath an indent, which had been made with a load of 100 N. The ion beam cuts were performed using an FEI HeliosNanoLab Dual Beammicroscope. This lamella was subjected to in situ heating cycles inside the TEM using a Gatan Model 652 double-tilt heating holder equipped with a Model 901 stage controller.

3.3 Results

Figure 3.1a shows the phase transformation behavior as characterized by DSC measurements: For the solutionized sample, only one peak is observed during either heating or cooling. Such behavior is typical for solutionized NiTi, strongly indicating that this alloy transforms in one step from martensite to austenite. The transformation to martensite starts at -36 °C (M_s) and finishes at -60 °C (M_f), while for the austenite formation a start temperature of -18 °C (A_s) and a finish temperature of -10 °C (A_f) are observed. These values are consistent with solutionzied 50.9 at% Ni used in a previous study.[35] In comparison, the transformation temperatures for the aged sample are shifted to higher values and the appearance of a second peak during heating and cooling indicates the occurrence of the intermediate R-phase.[36] As the peaks are overlapping, partial DSC cycles would be needed to precisely characterize the transformation temperatures. However, the curves clearly show an R-phase peak upon both cooling and heating, and therefore it is appropriate to estimate the transformation temperatures; for the aged material upon cooling, we found the values R_s = 22 °C and M_f = -25 °C. R_f and M_s are at approximately 5 °C, but are difficult to resolve individually. Upon heating the aged material, R_s =5 °C and A_f = 44 °C; R_f and A_s also overlap, estimated to be at approximately 27 °C.

XRD profiles for the two NiTi variants are shown in Figure 3.1b. For the solutionized sample, the profile shows only austenite peaks, indicating that the sample contains no other phases at room temperature. For the aged variant, the profile indicates mainly austenite peaks alongside other less pronounced peaks, which are highlighted in the inset graph covering the 2Θ-range of 38 - 48°. Comparing the diffractogram with the ICDD, it was determined that these less pronounced peaks were attributed to R-phase, martensite, and Ti_3Ni_4 precipitates.

To quantitatively analyze phase constituents in the aged variant, EBSD measurements were carried out. Figure 3.1c shows the phase distribution for a representative area on the sample. It is mainly composed of austenite (red) and precipitates (blue), with volume fractions measured to be 96.5% and 2.5%, respectively. The rod-shaped Ti_3Ni_4 precipitates have a typical length of approximately 520 nm, a width of about 150 nm, and are often situated at or near grain boundaries (marked by arrows in the inset). In addition, 0.1% of martensite and 0.7% of R-phase are observed, almost always in relative proximity to the grain boundaries.

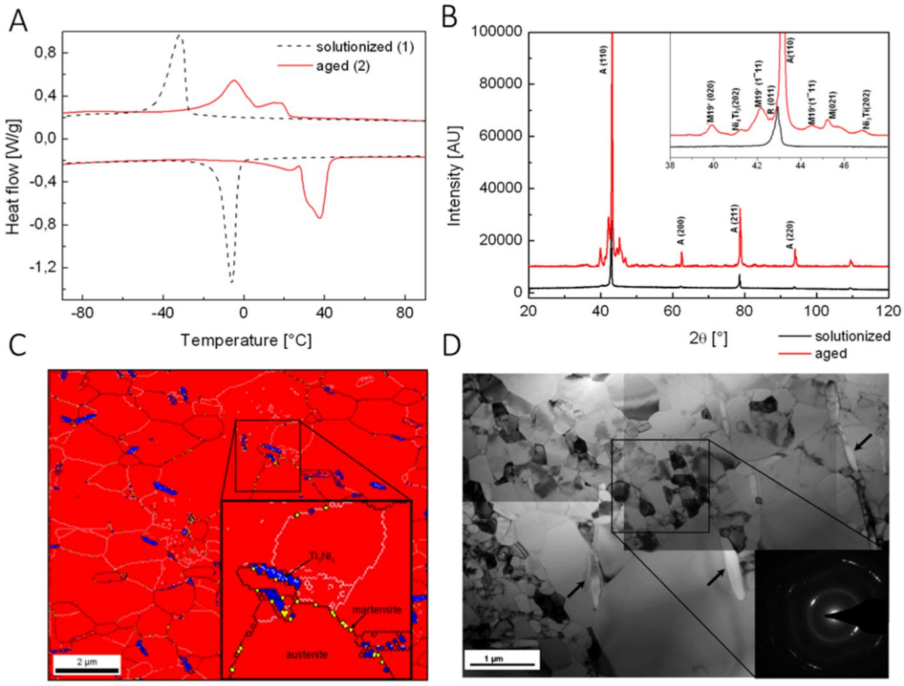

Figure 3.1: Microstructure characterization: (A) DSC curves showing the distinct phase transformation behavior in the two NiTi variants during thermal cycling. (B) XRD profiles indicating that the solutionized sample is austenitic at room temperature whereas the aged sample exhibits also other peaks attributed to R-Phase, martensite, and Ti_3Ni_4 precipitates (inset graph). (C) EBSD map of the phase distribution for a representative area of the aged sample composed of austenite (red), Ti_3Ni_4 precipitates (blue), martensite (yellow) and small amounts of R-phase. (D) Bright field image of a TEM analysis showing the bimodal grain size distribution and rod-shaped Ti_3Ni_4 precipitates (black arrows) in the aged sample. The diffraction pattern of a selected area indicates the mainly austenitic state of the sample (inset).

Additional insight into the microstructure of the aged material was obtained by TEM. The bright field image in Figure 3.1d shows that this sample has a bimodal grain size distribution with grains in the sub-micron and micron range. In the larger grains, the dislocation density is observed to be relatively low, and few rod-shaped Ti_3Ni_4 precipitates can be detected (exemplary precipitates are marked by black arrows). A selected area diffraction pattern in the inset of Figure 3.1d indicates that the sample is mainly in the austenitic state. The relative strain contrast frequently observed in the sub-micron grains is attributed to a residual dislocation structure.

Figure 3.2a and b shows depth profiles of representative Vickers indents performed with a load of 100 N on the aged and the solutionized variants, respectively. In order to visualize the indentation induced shape recovery due to a temperature change, the profiles are shown in the as-indented state as well as after heating and subsequent cooling. The indent widths were also optically measured and the corresponding depths for a Vickers indenter geometry calculated. This calculation of the theoretical indent depth demonstrates that the obtained WLI data points in the indentation groove are reasonable and reliable.

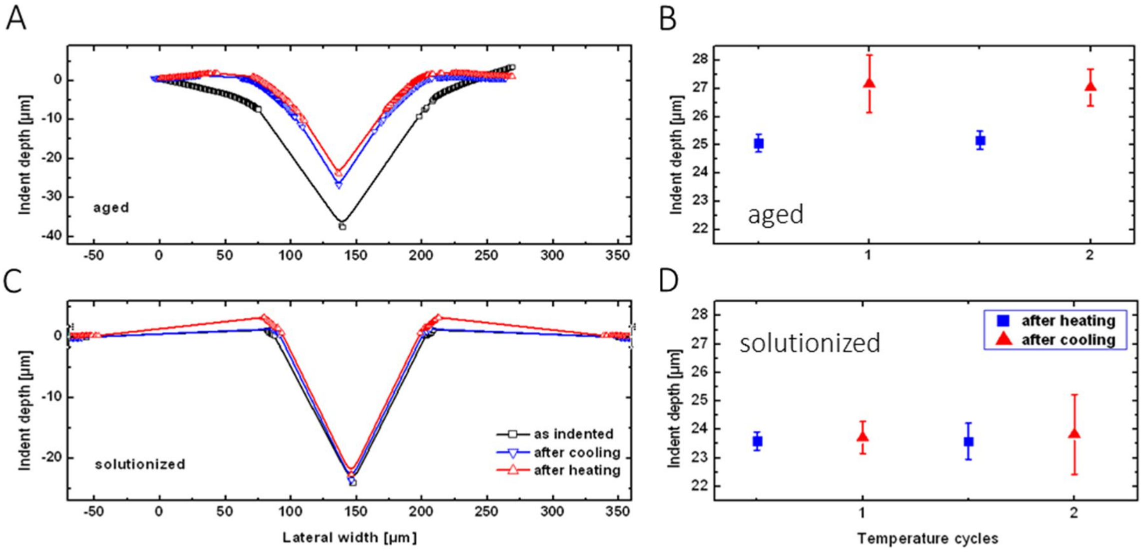

Figure 3.2: Change of indentation depth initially after indentation, after heating and second cooling. The Vickers indent was performed with a load of 100 N. The profiles show the indentation induced shape recovery according to the existing OWSME and TWSME in the aged (A) and solutionized (B) sample. Reversibility and shape recovery of indentation depth after thermal cycling are shown in the aged (C) and solutionized (D) material.

Figure 3.2 indicates that the indent morphology experienced two types of changes during thermal cycling above and below the transformation temperatures. First, both the lateral width and the depth of the indents on the aged variant decreased during the first heating step above the austenitic finish temperature. In particular, the average and standard deviation of the depth decreased from initially 39.7 ±0.3 µm to 25.1 ±0.4 µm (Figure 3.2a). Second, subsequent cooling below M_f led to an increase in depth, which was shown to be repeatable over several thermal cycles (Figure 3.2c). However, the reversible change in depth during these subsequent temperature cycles was much smaller than that observed for the first heating step, measuring approximately 2 µm. The irreversible shape recovery induced by the first heating is related to the OWSME, while the reversible change in depth during subsequent temperature cycles is a result of the TWSME. In contrast, the solutionized variant recovered only from 27.3 ±1.5 µm to 23.7 ±0.7 µm in depth during the first heating as shown in Figure 3.2b, and remained nearly unchanged during further cooling or heating cycles (Figure 3.2d).

The recovery ability of the indentation induced OWSME and TWSME are quantitatively evaluated by the depth recovery ratio.[35, 37-38] For the OWSME, it is defined as:

$$RR_{OW} = \frac{d_i - d_h}{d_i} \tag{3.1}$$

Whereas for the TWSME the recovery ratio is:

$$RR_{TW} = \frac{d_c - d_h}{d_c} \tag{3.2}$$

where d_i is the as-indented depth upon unloading, d_h is the depth after heating above A_f, and d_c is the depth after cooling below M_f. Previous studies investigating fully martensitic NiTi using Berkovich or Vickers indentation showed a RR_{OW} of 20 - 40%.[37-38] In the present study, the solutionized NiTi indents showed a RR_{OW}=13%, and no measurable RR_{TW}. The aged NiTi demonstrated significantly increased recovery, with a RR_{OW}=37%, and RR_{TW}=7%.

After the depth recovery of the indents had been fully characterized, the aged NiTi variant was planarized and subjected to the same temperature cycles as described previously. Figure 3.3 shows representative WLI images of the planarized surface for the aged variant at room temperature.

Initially, the sample was cooled below M_s, and then allowed to heat up to room temperature, leading to a relatively flat surface (Figure 3.3a). Afterwards, it was heated above A_f and allowed to cool down back to room temperature, creating a pattern of surface protrusions (Figure 3.3b). After cooling with liquid nitrogen, it can be seen that the indents were almost completely removed; heating of the sample above the transformation temperature led to the formation of protrusions at the former positions of the indents. This switchable morphology was repeatable over three cooling and heating cycles. Furthermore, it was observed that protrusion height was dependent on the indentation load, which is highlighted in Figure 3.3c, where the height of the protrusions after successive heating and cooling steps is plotted as a function of the indentation load. The height of the protrusions after heating increased from 0.70 ±0.20 μM to 2.31 ±0.12 μm as the indentation load increased from 20 N to 200 N. In addition, it is observed that the protrusions did not disappear completely after cooling and that the height of the remaining protrusions also increased with the indentation load. In particular, the residual height increased slightly from 0.26 ±0.10 μm to 0.54 ±0.15 μm, as the indentation load increased from 20 N to 200 N.

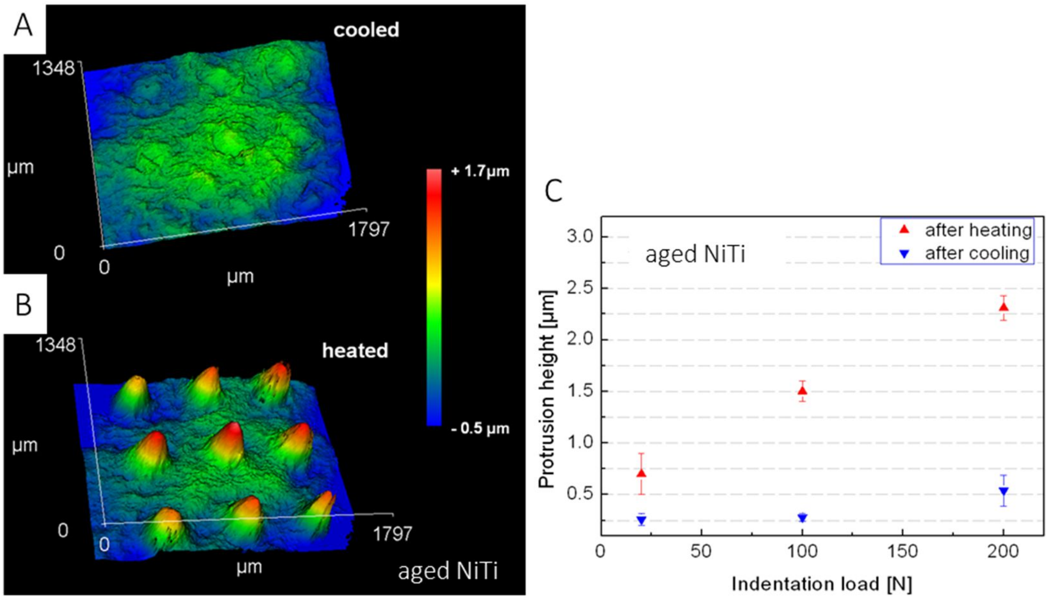

Figure 3.3: 3D – white light interferometry images of the surface topography at room temperature after cooling (A) or heating (B). The reversible formation of surface protrusions due to indentation induced TWSME is shown. Dependence of protrusion height on the indentation load (C) and their recovery behavior after cooling.

In order to better understand the microstructural mechanisms, which influence the TWSME observed in the aged indented material, a TEM lamella was cut beneath a representative 100N indent. The TEM images of the areas are shown in Figure 3.4.

It is important to note that the right hand side of the image captures the material directly beneath the indent as schematically indicated in Figure 3.4a. However, the total width of the indent is much larger than the lamella.

The bright field TEM image (Figure 3.4b) reveals preferentially oriented martensitic plates that mirror the general shape of the Vickers indenter, as well as dislocations. The specific alignment of the martensite indicates that these variants were preferentially induced by the stress field.

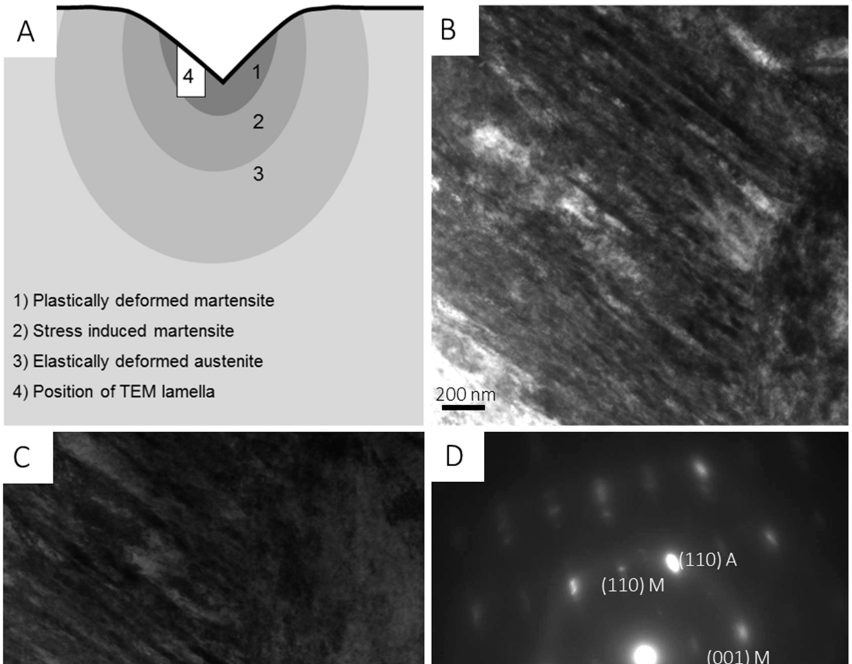

Figure 3.4: Sketch of the existing phase compositions beneath the indent and the surrounding area (a, 1–3). Position of the tested TEM lamella (A, 4). Bright field TEM images of the lamella cut from the indentation-deformed volume, at room temperature (B) and after in situ heating to 120 °C (C). The preferentially oriented martensitic plates and dislocations remain during heating. The diffraction pattern reveals the presence of austenite and martensite at elevated temperature (D).

Similar sized regions of aligned martensite were not observed in the original microstructure (Figure 3.1d). In situ heating of the lamella to 120 °C, which is well above the A_f temperature, showed that a significant portion of the martensitic plates remained stable (Figure 3.4c). The diffraction pattern in Figure 3.4d confirms the presence of both austenite and martensite in the lamella at the elevated temperature.

3.4 Discussion

The purpose of this study is to better understand the underlying microstructural mechanisms, which dictate the indentation induced TWSME in NiTi. The material chosen for this study was slightly nickel-rich (50.9 at% Ni) and is known to have relatively low transformation temperatures (Figure 3.1a).[12] Based on previous work, the solutionized variant is believed to have a relatively low dislocation density and homogeneous grain size distribution.[35] DSC measurements confirm that only austenite is stable at room temperature. The aged sample exhibits a more complicated microstructure and transformation behavior. Previous studies show that aging Ni-rich material elicits Ti_3Ni_4 precipitates.[35-36, 39] The stress-state around the precipitates is known to assist in the martensitic phase transformation, effectively increasing the phase transformation temperatures, as shown by DSC on our aged material.[13] Strong stress fields induced by the Ti_3Ni_4 precipitates are also known to stimulate the intermediate transformation of the rhombohedric R-phase consistent with the observations in Figure 3.1.[17, 39] Depending on the transformation temperatures (Figure 3.1a), martensite, austenite, or the R-phase may be stable at RT. However, all indentations were performed after a heating cycle above A_f, and therefore the microstructure was primarily austenitic as confirmed by EBSD and TEM investigation (Figure 3.1c and d).

Under the conditions used in this study, both the solutionized and the aged NiTi should deform by a stress-induced formation of martensite. This can be rationalized by the thermo mechanical nature of the martensite/austenite phase transformation and the Clausius–Clapeyron type relationship between the transformation stress and temperature.[12] Because the phase transformation temperatures of the aged material are much closer to RT, a lower stress is required to produce stress-induced martensite. This is, in part, reflected by the larger initial indentation depths observed in the aged NiTi for a given load (Figure 3.2a and b). Previous studies have also shown indentation depth is a function of transformation temperatures.[40] However, analysis is complicated by the spatially dependent strain gradient beneath the indenter and the differences in the inherent microstructure between the aged and solutionized materials. Continued deformation beyond that which can be accommodated by the phase transformation is expected to result in plastic deformation of the martensite.

It is also important to consider that the stress state beneath the indenter is not homogeneous; there exists a complicated three-dimensional strain gradient. The volume of material directly beneath the indent will experience the most deformation, tapering off for material that is further away. For example, Chaudhri[41] estimated a maximum of 25 - 36% strain for Vickers indentation. Adjacent to this highly deformed volume is a strong gradient of plastic strain. Beyond that, the surrounding material that only experiences elastic deformation will act as a hydrostatic constraint. For Vickers indents into NiTi, deformation behavior is further complicated by the phase transformation, which acts as an intermediate deformation mechanism.

We propose that the OWSME and TWSME results shown in this study can be best understood by considering the strain distribution beneath the indent. This approach is analogous to that taken by Su et al.[42] We believe that three regions exist after indentation: (i) plastically deformed martensite, (ii) stressinduced martensite, and (iii) elastically deformed austenite. The high strains directly beneath the indent lead to plastically deformed martensite. This is substantiated by the TEM images shown in Figure 3.4b-d. Beneath this lies a much larger volume of stress-induced martensite, surrounded by elastically deformed austenite. There is also likely a region of R-phase material for the aged NiTi. However, this phase transformation is associated with a relatively small amount of strain of approximately 1%.[12] A schematic overview of the regions is presented in Figure 3.4a.

It is important to note that indents in both materials partially recovered their depth during the first heating as is evidenced by the value of RR_{OW}=13% for the solutionized and RR_{OW}=31% for the aged material. This is not intuitive, as the solutionized material is expected to exhibit pseudoelastic behavior at RT. However, previous research has observed similar behavior for pseudoelastic NiTi.[35] It is believed that the plastically deformed martensite directly beneath the indent partially inhibits the reverse phase transformation of the surrounding stressinduced martensite. Upon heating well above A_f, the martensite is able to overcome this barrier and transforms to austenite, also exhibiting the OWSME for the solutionized NiTi. This is consistent with the observed high work output of NiTi.[43] The aged NiTi is expected to show shape memory behavior, which is consistent with the much larger OWSME observed (RR_{OW}=37%). Previous research using finite element analysis to estimate the indentation stress profile relative to the critical stress for dislocation slip and martensite reorientation estimated that the recovery ratio could be approximately 40% for pyramidal indenters.[38]

The disparity of the recovery ratios observed for the aged and the solutionized material is also an indication that Vickers indentation induces different amounts of stress induced/stabilized martensite in both samples. This is related to the lower phase transformation temperature of the solutionized material (Figure 3.1a). According to the Clausius–Clapeyron relationship between transformation stress and temperature, higher transformation stresses are required in the material with the lower transformation temperature relative to the test temperature to start the martensite formation. Therefore, for a given indentation load, the solutionized NiTi shows a much smaller fraction of martensite compared to the aged NiTi.

The TWSME observed for the indents and the planarized surface of the aged sample is related to the stabilized martensite directly beneath the indent (Figure 3.4). The thermally stabilized martensite can act as nucleation site of thermal martensite during cooling and by this enhance the growth of preferentially oriented martensite variants. In contrast, the stress-induced martensite in the solutionized sample is not thermally stable. Therefore, the sample is fully transformed into austenite by the first heating and the selfaccommodation of the martensitic variants circumvents a shape change during cooling.[44]

The TEM results in Figure 3.4 shows stabilized martensite at RT and at high temperatures beneath an indent, which mirrors the shape of the Vickers indenter. This observation is a notable variation from conclusions drawn by Zhang et al. [28-31] that the preferential dislocation structure due to indentation leads to thermall-induced preferentially oriented martensite. Rather, the TEM data from this study shows that a significant portion of the martensite remains stable even at very high temperatures relative to A_f. This indicates that the dislocations and/or the high internal stress stabilize the stress-induced martensite remaining at higher temperatures. Previous studies have shown that NiTi under constraint requires higher temperatures for reverse phase transformation.[45-46] Further TEM studies using NiTi of different compositions, microstructures, and indentation conditions are currently underway in order to draw more global conclusions about the microstructural mechanisms which dictate the TWSME surfaces.

3.5 Conclusions

We studied the SME of heavily cold drawn NiTi (50.9 at% Ni). Our experiments can be summarized as follows:

» A solutionizing heat treatment resulted in an austenitic NiTi material at RT with a relatively low dislocation density and homogeneous grain distribution, and is expected to show pseudoelastic behavior. Aging elicits Ti_3Ni_4 precipitates, which are known to assist in the martensitic phase transformation, effectively increasing the phase transformation temperatures. Based on the transformation temperatures, the aged NiTi is likely to show shape memory behavior. Both solutionized and aged samples were mostly austenitic during indentation.

» The strain gradient beneath the indentation probe results in three deformation zones: (i) plastically deformed martensite, (ii) stress-induced martensite, and (iii) elastically deformed austenite. Relative to the solutionized material, the aged material is expected to have a larger region of stress-induced martensite.

» Indentations in the solutionized NiTi show some recovery during the first heating, which is related to the OWSME. It is concluded that the plastically deformed martensite directly beneath the indent inhibits spontaneous recovery of the stress-induced martensite expected from this pseudoelastic material. Heating well above A_f, ultimately results in some reverse phase transformation and deformation recovery. The aged NiTi shows a much higher RR_{OW} as it is in the shape memory regime.

» The solutionized NiTi did not exhibit any TWSME, while the aged NiTi did. TEM imaging of material directly beneath the indent for the aged NiTi shows preferentially oriented thermally stabilized martensite. It is believed that this region acts as a nucleation site for martensite during cooling and guides the growth of preferentially oriented martensite variants.

In summary, this work clarified that both the initial microstructure and the indenter shape play a strong role in the indentation induced TWSME. The significant influence of the precipitates opens promising possibilities to tailor the indentation induced TWSME, even in austenitic matrix material showing increased mechanical properties compared to martensitic NiTi.

3.6 Acknowledgments

The authors are grateful to Jörg Schmauch, Rudolf Karos, and Birgit Heiland for help in the experiments. CPF gratefully acknowledges support of this work from the National Science Foundation (NSF) CAREER award (Grant No. DMR- 1255603), as well as the University of Wyoming International Travel Grant.

3.7 References

1. Qin, E.; Peter, N. J.; Frensemeier, M.; Frick, C. P.; Arzt, E.; Schneider, A. S., Vickers Indentation Induced One-Way and Two-Way Shape Memory Effect in Austenitic NiTi. *Advanced Engineering Materials* **2014,** *16* (1), 72-79.
2. Duerig, T.; Pelton, A.; Stöckel, D., An overview of nitinol medical applications. *Materials Science and Engineering: A* **1999,** *273*, 149-160.
3. Morgan, N. B., Medical shape memory alloy applications - the market and its products. *Materials Science and Engineering a-Structural Materials Properties Microstructure and Processing* **2004,** *378* (1-2), 16-23.
4. Bansiddhi, A.; Sargeant, T. D.; Stupp, S. I.; Dunand, D. C., Porous NiTi for bone implants: A review. *Acta Biomaterialia* **2008,** *4* (4), 773-782.
5. DesRoches, R.; Delemont, M., Seismic retrofit of simply supported bridges using shape memory alloys. *Engineering Structures* **2002,** *24* (3), 325-332.
6. Song, G.; Ma, N.; Li, H. N., Applications of shape memory alloys in civil structures. *Engineering Structures* **2006,** *28* (9), 1266-1274.
7. Janke, L.; Czaderski, C.; Motavalli, M.; Ruth, J., Applications of shape memory alloys in civil engineering structures - Overview, limits and new ideas. *Materials and Structures* **2005,** *38* (279), 578-592.
8. Bellouard, Y., Shape memory alloys for microsystems: A review from a material research perspective. *Materials Science and Engineering a-Structural Materials Properties Microstructure and Processing* **2008,** *481*, 582-589.
9. Fu, Y. Q.; Du, H. J.; Huang, W. M.; Zhang, S.; Hu, M., TiNi-based thin films in MEMS applications: a review. *Sensors and Actuators A - Physical* **2004,** *112* (2-3), 395-408.
10. Gill, J. J.; Ho, K.; Carman, G. P., Three-dimensional thin-film shape memory alloy microactuator with two-way effect. *Journal of Microelectromechanical Systems* **2002,** *11* (1), 68-77.
11. Otsuka, K.; Wayman, C. M., *Shape memory materials*. Cambridge university press: **1999**.
12. Otsuka, K.; Ren, X., Physical metallurgy of Ti-Ni-based shape memory alloys. *Progress in Materials Science* **2005,** *50* (5), 511-678.
13. Gall, K.; Sehitoglu, H.; Chumlyakov, Y. I.; Kireeva, I. V.; Maier, H. J., The influence of aging on critical transformation stress levels and martensite start temperatures in NiTi: Part I - Aged microstructure and micro-mechanical modeling. *Journal of Engineering Materials and Technology - Transactions of the ASME* **1999,** *121* (1), 19-27.
14. Eggeler, G.; Hornbogen, E.; Yawny, A.; Heckmann, A.; Wagner, M., Structural and functional fatigue of NiTi shape memory alloys. *Materials Science and Engineering a-Structural Materials Properties Microstructure and Processing* **2004,** *378* (1-2), 24-33.
15. Nagasawa, A.; Enami, K.; Ishino, Y.; Abe, Y.; Nenno, S., Reversible shape memory effect. *Scripta Metallurgica* **1974,** *8* (9), 1055-1060.
16. Perkins, J., Residual stresses and the origin of reversible (two-way) shape memory effects. *Scripta Metallurgica* **1974,** *8* (12), 1469-1476.
17. Liu, Y. N.; Liu, Y.; Van Humbeeck, J., Two-way shape memory effect developed by martensite deformation in NiTi. *Acta Materialia* **1998,** *47* (1), 199-209.
18. Benafan, O.; Padula, S. A.; Noebe, R. D.; Sisneros, T. A.; Vaidyanathan, R., Role of B19 ' martensite deformation in stabilizing two-way shape memory behavior in NiTi. *Journal of Applied Physics* **2012,** *112* (9).

19. Lahoz, R.; Puertolas, J. A., Training and two-way shape memory in NiTi alloys: influence on thermal parameters. *Journal of Alloys and Compounds* **2004,** *381* (1-2), 130-136.
20. Miller, D. A.; Lagoudas, D. C., Influence of cold work and heat treatment on the shape memory effect and plastic strain development of NiTi. *Materials Science and Engineering a-Structural Materials Properties Microstructure and Processing* **2001,** *308* (1-2), 161-175.
21. Filip, P.; Mazanec, K., The two way memory effect in TiNi alloys. *Scripta Materialia* **1996,** *35* (3), 349-354.
22. Guilemany, J.; Fernandez, J., Effect of training time on two way shape memory effect obtained by stabilised stress induced martensite. *Scripta Metallurgica Et Materialia* **1994,** *30* (1), 59-61.
23. Liu, Y.; McCormick, P., Factors influencing the development of two-way shape memory in NiTi. *Acta Metallurgica Et Materialia* **1990,** *38* (7), 1321-1326.
24. Fukuda, T.; Deguchi, A.; Kakeshita, T.; Saburi, T., Two-way shape memory properties of a Ni-rich Ti-Ni alloy aged under tensile-stress. *Materials Transactions Jim* **1997,** *38* (6), 514-520.
25. Fukuda, T.; Takahata, M.; Kakeshita, T.; Saburi, T., Two-way shape memory properties of a Ti-51Ni single crystal including Ti3Ni4 precipitates of a single variant. *Materials Transactions Jim* **2001,** *42* (2), 323-328.
26. Sato, M.; Ishida, A.; Miyazaki, S., Two-way shape memory effect of sputter-deposited thin films of Ti 51.3 at% Ni. *Thin Solid Films* **1998,** *315* (1-2), 305-309.
27. Nishida, M.; Honma, T., All-round shape memory effect in Ni-rich TiNi alloys generated by constrained aging. *Scripta Metallurgica* **1984,** *18* (11), 1293-1298.
28. Zhang, Y.; Cheng, Y. T.; Grummon, D. S., Shape memory surfaces. *Applied Physics Letters* **2006,** *89*, 041912.
29. Fei, X. L.; Zhang, Y. J.; Grummon, D. S.; Cheng, Y. T., Indentation-induced two-way shape memory surfaces. *Journal of Materials Research* **2009,** *24* (3), 823-830.
30. Zhang, Y.; Cheng, Y.-T.; Grummon, D. S., Two-way indent depth recovery in a NiTi shape memory alloy. *Applied Physics Letters* **2006,** *88* (13), 131904-131904-3.
31. Zhang, Y. J.; Cheng, Y. T.; Grummon, D. S., Understanding indentation-induced two-way shape memory effect. *Journal of Materials Research* **2007,** *22* (10), 2851-2855.
32. Gall, K.; Sehitoglu, H.; Chumlyakov, Y. I.; Kireeva, I. V., Tension–compression asymmetry of the stress–strain response in aged single crystal and polycrystalline NiTi. *Acta Materialia* **1999,** *47* (4), 1203-1217.
33. Sehitoglu, H.; Karaman, I.; Anderson, R.; Zhang, X.; Gall, K.; Maier, H. J.; Chumlyakov, Y., Compressive response of NiTi single crystals (vol 48, pg 3311, 2000). *Acta Materialia* **2001,** *49* (4), 747-747.
34. Frick, C. P.; Ortega, A. M.; Tyber, J.; Gall, K.; Maier, H. J., Multiscale structure and properties of cast and deformation processed polycrystalline NiTi shape-memory alloys. *Metallurgical and Materials Transactions a-Physical Metallurgy and Materials Science* **2004,** *35A* (7), 2013-2025.
35. Frick, C. P.; Ortega, A. M.; Tyber, J.; Maksound, A. E. M.; Maier, H. J.; Liu, Y. N.; Gall, K., Thermal processing of polycrystalline NiTi shape memory alloys. *Materials Science and Engineering a-Structural Materials Properties Microstructure and Processing* **2005,** *405* (1-2), 34-49.
36. Liu, Y.; Kim, J. I.; Miyazaki, S., Thermodynamic analysis of ageing-induced multiple-stage transformation behaviour of NiTi. *Philosophical Magazine* **2004,** *84* (20), 2083-2102.

37. Ni, W.; Cheng, Y.-T.; Grummon, D. S., Recovery of microindents in a nickel–titanium shape-memory alloy: a “self-healing” effect. *Applied Physics Letters* **2002,** *80* (18), 3310-3312.
38. Shaw, G.; Stone, D.; Johnson, A.; Ellis, A.; Crone, W., Shape memory effect in nanoindentation of nickel–titanium thin films. *Applied Physics Letters* **2003,** *83* (2), 257-259.
39. Khalil-Allafi, J.; Dlouhy, A.; Eggeler, G., Ni 4 Ti 3-precipitation during aging of NiTi shape memory alloys and its influence on martensitic phase transformations. *Acta Materialia* **2002,** *50* (17), 4255-4274.
40. Huang, W.; Su, J.; Hong, M.; Yang, B., Pile-up and sink-in in micro-indentation of a NiTi shape-memory alloy. *Scripta Materialia* **2005,** *53* (9), 1055-1057.
41. Chaudhri, M., Subsurface strain distribution around Vickers hardness indentations in annealed polycrystalline copper. *Acta Materialia* **1998,** *46* (9), 3047-3056.
42. Su, J.; Huang, W. M.; Hong, M. H., Indentation and two-way shape memory in a NiTi polycrystalline shape-memory alloy. *Smart Materials and Structures* **2007,** *16* (1), S137.
43. Krulevitch, P.; Lee, A. P.; Ramsey, P. B.; Trevino, J. C.; Hamilton, J.; Northrup, M. A., Thin film shape memory alloy microactuators. *Microelectromechanical Systems, Journal of* **1996,** *5* (4), 270-282.
44. Liu, Y.; Favier, D., Stabilisation of martensite due to shear deformation via variant reorientation in polycrystalline NiTi. *Acta Materialia* **2000,** *48* (13), 3489-3499.
45. Kato, H.; Inagaki, N.; Sasaki, K., A one-dimensional modelling of constrained shape memory effect. *Acta Materialia* **2004,** *52* (11), 3375-3382.
46. Tanaka, K.; Kobayashi, S.; Sato, Y., Thermomechanics of transformation pseudoelasticity and shape memory effect in alloys. *International Journal of Plasticity* **1986,** *2* (1), 59-72.

Chapter 4

Indentation induced two-way shape memory effect in aged Ti-50.9 at.% Ni

Abstract - In this study, Vickers indentation was used to investigate the two-way shape memory effect (TWSME) in an austenitic Ti-50.9 at.% Ni alloy, exposed to different heat treatments. Three aging treatments were used to manipulate the size of Ti_3Ni_4 precipitates. All samples were Vickers indented, and the indent depth was investigated as function of thermal cycling. The TWSME was found only in the material aged at 400 °C, which contained coherent precipitates. Thermal cycling shows stable TWSME, however, heating well above the austenite finish temperature lead to permanent austenitic protrusions. The results indicate that stabilized martensite plays a critical role in creating TWSME surfaces.

This chapter was published in *MRS Communications (2015), 5, 77-82.*[1]

4.1 Introduction

Nickel–titanium (NiTi) shape memory alloys are capable of recovering their previously defined shape after certain deformation upon the application of heat. This recovery, called one-way shape memory effect (OWSME), is due to a stress-induced martensitic phase transformation, i.e., a coordinated shift in atomic structure, that is completely reversible even for large strains up to approximately 8–12%.[2] Through an appropriate combination of deformation processing and/or heat treatment, it is possible to elicit a switchable TWSME.[3] This effect is characterized by the alloy's memorization of the high- and low temperature shape, allowing for spontaneous change between these shapes as a function of cycling temperature. The intrinsic mechanism that dictates the TWSME remains a subject of research interest.

Recent studies have shown that a TWSME surface can be induced in NiTi using an indentation method.[4-6] The near equiatomic NiTi samples were indented to high strains, thermally cycled, then planarized, and re-polished. When the sample was reheated into the austenite phase, protrusions formed on the sample surface, a phenomenon found to be repeatable over multiple heating cycles. The protrusions were hypothesized to be caused by preferentially oriented dislocation structures, which remained underneath and around the indentation site after planarization. A more recent microstructural characterization performed on Ti-50.9 at.% Ni shape memory surfaces after Vickers indentation revealed both dislocations and thermally stabilized martensitic plates parallel to the indents.[7] It was theorized that this stabilized martensite may act as nucleation seed for the TWSME. However, more detailed testing is necessary for a deeper understanding of these TWSME surfaces.

The purpose of this study is to expand the limited experimental studies on TWSME surfaces by investigating the effect of pre-existing Ti_3Ni_4 precipitates. For slightly Ni-rich NiTi, precipitates are well known to influence the martensitic phase transformation. It has been shown by Gall and colleagues that coherent Ti_3Ni_4 precipitates increase the stress necessary for plastic flow and decrease the martensite transformation stress (e.g., [8-9]). Essentially, local stress fields caused by precipitates act in addition to an applied external stress, and become the location of the phase transformation. Thus, the transformation stress scales inversely with the precipitate coherency. Unfortunately, the role of preexisting precipitates on the indentation induced TWSME is not well understood. Therefore our approach was to vary the aging time systematically, leading to either: (i.) solutionized, (ii.) coherent, or (iii.) incoherent Ti_3Ni_4 precipitates. TWSME surfaces were then created via Vickers indentation followed by planarization. The results show that coherent precipitates were critical for good TWSME behavior and the protrusion height as well as the two-way deformation recovery were sensitive to the re-heat temperature. The observed behavior is discussed in terms of the underlying microstructural mechanisms.

4.2 Experimental

Three bulk samples were electro-discharge machined from rod stock of a cold-drawn Ti-50.9 at.% Ni alloy, used in previous studies.[7, 10] These samples were oven heated to 700 °C for 1.5 h and then immediately water quenched, which is well known to lead to a solutionized microstructure. The solutionized NiTi has an austenitic B2 structure at room temperature. Two of the solutionized samples were aged for 1.5 h and water quenched at 400 °C and at 550 °C, respectively. These aging treatments were explicitly aimed at generating either coherent (400 °C) or incoherent precipitates (550 °C).

Using a wire-cutting saw, slices weighing approximately 10 mg were prepared for thermal analysis by differential scanning calorimetry (DSC) using a Mettler Toledo DSC1 Star System. The heating/cooling rate was set as 20 °C/min. The phase transformation temperatures were obtained by the tangent methods and listed in Table 4.1.

The microstructures of the aged specimens were investigated via a Philips CM200 transmission electron microscope (TEM). Electron transparent samples were prepared by grinding (down to 4000 grade SiC paper) discs of 3 mm diameter to a final thickness of 50 μm and subsequent twin jet polishing at 20 V using an electrolyte of 20 vol.% sulfuric acid and 80 vol.% methanol.

Deformation recovery was investigated by measuring the depth of Vickers indents, as a function of thermal cycling. Samples were grinded down to 4000 grade SiC paper, followed by electropolishing with an electrolyte solution composed of 20 vol.% sulfuric acid and 80 vol.% methanol, leading to a final average roughness (R_a) of approximately 0.15 μm. Indentation was performed with a Leco v-100 indenter at room temperature with a load of 20 N, a loading time of approximately 5 s and a holding time of 10 s. The depth of the indents was measured via white-light interferometry (Zygo NewView 5000) at room temperature, after subsequent heating above the transformation temperature, and after cooling with liquid nitrogen (ln) at room temperature. Measurements of the indent depth in the initial and heated state were taken in situ using a custom-built heating stage.

To generate the TWSME surface for the protrusion analysis an array of six Vickers indents with an interspacing of 900 µm from center to center was indented into a polished surface. A maximum load of 200 N, a loading time of approximately 5 s, and a holding time of 10 s was used. The higher load was chosen to increase the size of the protrusions, which correlates with the indentation diameter and depth. Thus, the indent diameter of approximately 300 µm leads to protrusions of approximately 300 µm in diameter. Based on preliminary analysis, the large interspace between the indents was chosen to avoid any interaction of the intrinsic stress fields induced by the indents.

The residual indents were removed via grinding and electropolishing, to a depth just below the indents as estimated optically. The re-planarized and trained surface showed reversible protrusions of several microns upon heating and re-flattening after cooling. Measurements of the protrusion height at different maximum temperatures of 80, 100, 120, 160, and 200 °C and subsequent cooling with ln in between each cycle, were carried out.

4.3 Results and discussion

The characteristic phase transformation temperatures of the three investigated materials, shown in Figure 4.1 were measured by DSC. The specific transformation temperatures are listed in Table 4.1. The solutionized material exhibits a one-step transformation from austenite to martensite, with all transformation temperatures well below room temperature.

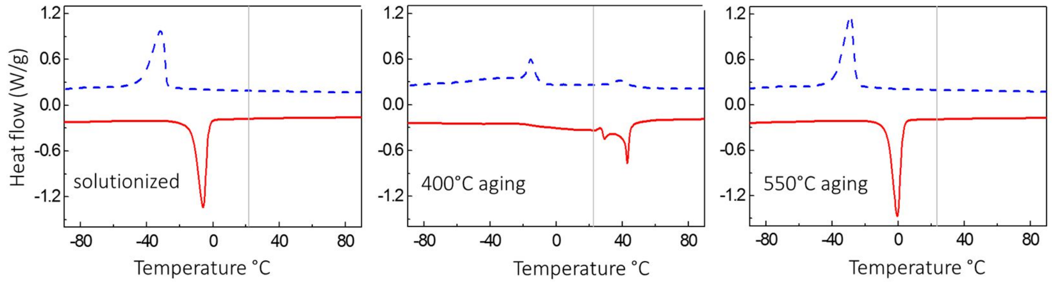

Figure 4.1: Representative DSC curves for the three tested NiTi samples: (A) solutionized, (B) solutionized then aged at 400 °C for 1.5 h, (C) solutionized then aged at 550 °C for 1.5 h. The dashed line indicates cooling and the vertical line represents room temperature, where all indentation testing was performed.

This is expected due to the excess Ni content above equiatomic.[3] Upon aging at 400 °C for 1.5 h, the transformation temperatures increase. Notably, a secondary peak appears for both heating and cooling. This is associated with an intermediate orthorhombic phase, termed the R-phase. The presence of the R-phase is typical for aged, Ni-rich, NiTi.[10-11] The specimen aged at 550 °C for 1.5 h resembles more closely the solutionized NiTi, although the phase transformation temperatures are significantly higher. The microstructure of the two aged NiTi samples used in this study is shown in the representative bright-field TEM images in Figure 4.2.The solutionized NiTi was not explicitly investigated as thermal history and DSC measurements strongly indicate that the material has been solutionized.[12]

The sample aged at 400 °C (Figure 4.2,a) shows precipitates with a length of approximately 100 nm, leading to strong internal strain fields in the microstructure due to their coherency.[12] These homogenously distributed precipitates lead to intrinsic stress fields by means of austenitic lattice distortion. The strain fields assist in the stress-induced martensitic phase transformation, and effectively increase the phase transformation temperatures. [8-9, 12] The primary and brightest pattern observed in the selected area diffraction pattern (Figure 4.2, a, inset) are from the $[\overline{111}]$ B2 zone axis confirming the presence of austenite. The secondary, weak reflections stem from the R-phase at 1/3 [110] B2 positions, and from the Ti_3Ni_4 precipitates lying at 1/7 [321] B2 positions.

Table 4.1: Transformation temperatures derived from DSC curves for the tested NiTi materials (A, austenite; M, martensite; R, R-phase).

^{f}Finish temperature	Heating (°C)				Cooling (°C)			
^{s}Start temperature	R_s	R_f	A_s	A_f	R_s	R_f	M_s	M_f
Solutionized	---	---	-13	-3	---	---	-28	-43
400°C aging	26	35	37	45	50	35	47	-20
550°C aging	---	---	-8	4	---	---	-26	-39

The DSC curves (Figure 4.1) are consistent with the assumption of the presence of the R-phase; however, it is clear that the 400 °C aged material is mostly austenite. TEM images of the 550 °C aged specimen (Figure 4.2, b) show that the lenticular Ti_3Ni_4 precipitates have increased in size to several hundred nanometers. The inset in Figure 4.2, b illustrates a stress induced fringe contrast in proximity to a precipitate. Nonetheless, the 550 °C aged specimens show a lower overall internal distortion compared with the 400 °C aging, which is consistent with overaging. Thus, the microstructural features of the different samples have to be considered as a fully austenitic lattice for the solutionized material, high amount of intrinsic stress fields induced by coherent precipitates of mid-size precipitates for the 400 °C aged material, and overaged precipitates leading into semi/non-coherent interface to the austenitic phase for the 550 °C aged material.

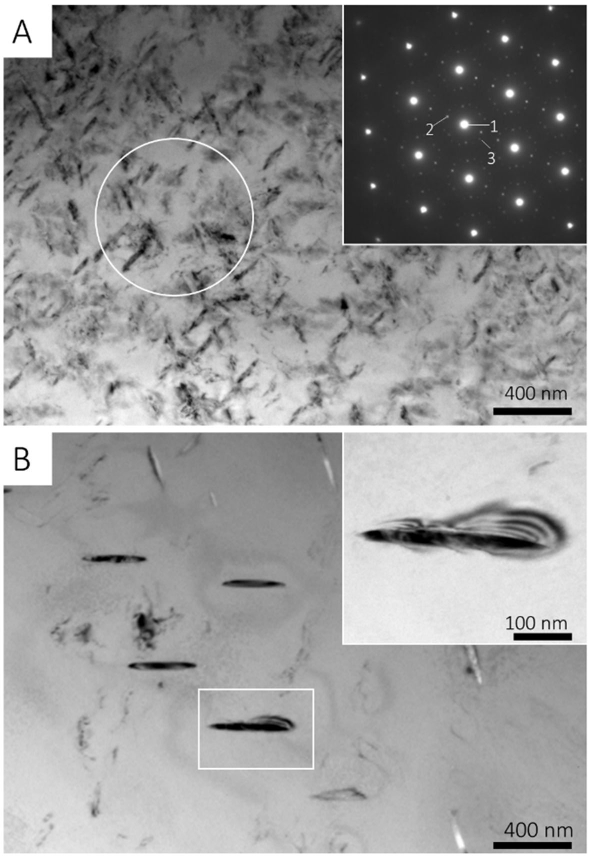

Figure 4.2. Bright-field TEM images of NiTi aged at (A) 400 °C and (B) 550 °C. Both heat treatments lead to lenticular-shaped Ti_3Ni_4 precipitates. The diffraction pattern [(A), inset, aperture 800 nm] shows mainly austenitic phase (1,$[\overline{111}]$ B2) with weak reflections at the 1/3 [110] B2 positions, revealing the presence of the R-phase (2) and Ti_3Ni_4 precipitates lying at 1/7 [321] B2 (3). Further heat treatment shows increasing precipitation size with stress-induced fringe contrast [(B), inset].

Each of the three samples was deformed via Vickers indentation with a load of 20 N, which was performed at room temperature. The indent depth was quantified in the heated and the cooled states by white-light interferometry, as tabulated in Table 4.2. Previous studies have shown that the TWSME effect can be directly observed by measuring repeated indentation depth recovery.[4-7] The results show depths taken immediately after indentation, after first heating to 80 °C, after cooling with ln, then after reheating to 80 °C. The OWSME recovery ratio (RR_{OW}) and TWSME recovery ratio (RR_{TW}) can be calculated using the respective changes in indentation depth.[12-14] For the OWSME the recovery ratio is defined as:

$$RR_{OW} = \frac{(d_i - d_h)}{d_i} \tag{4.1}$$

and for the TWSME it is:

$$RR_{TW} = \frac{(d_c - d_h)}{d_c} \tag{4.2}$$

where d_i is the initial depth, d_h is the depth after heating above A_f(austenite finish temperature), and d_c is the depth after cooling below M_f (martensite finish temperature).

Table 4.2: White light interferometry measurements of indentation depths. All measurements were taken at room temperature, prior to either heating above 80°C or prior to cooling with liquid nitrogen.

		solutionized	400°C aging	550°C aging
One-Way Shape Memory	Initial indent (μm)	12.0	15.5	12.0
	After 1st heating (μm)	10.3	9.1	11.0
	Recovery (μm)	1.7	6.4	1.0
	Recovery ratio (%)	14.0	41.0	8.0
Two-Way Shape Memory	Repeated cooling (μm)	9.0	10.0	9.0
	Repeated heating (μm)	9.0	9.1	9.0
	Recovery (μm)	0.0	0.9	0.0
	Recovery ratio (%)	0.0	9.0	0.0

The results in Table 4.2 illustrate that all three materials show some permanent deformation and some indent recovery upon the first heating (i.e., the OWSME). Therefore, a combination of martensite and plasticity must exist in the deformed material beneath the residual indent. The solutionized and 550 °C aged samples exhibit similar RR_{OW} values of 14 and 8%, respectively. The 400 °C aged sample exhibits a larger RR_{OW} of 41%. Similar values have been reported in literature[12, 14] and can be best understood by considering the Clausius–Clapeyron relationship.[15] For conventional uniaxial testing, deformation at temperatures below A_s leads to shape memory and above A_f to pseudoelastic behavior. With increasing strain beyond what can be accommodated by martensitic phase transformation and reorientation, plasticity of the martensite is expected. A_s Vickers indentation leads to a complex threedimensional (3D) stress-state, with a strong spatial strain gradient beneath the indent, it is not as straightforward to characterize; however, the same basic relationship holds true.

For the solutionized and 550 °C aged materials, indentation at room temperature is well-above A_f, and therefore a significant fraction of the phase transformation deformation is expected to be pseudoelastic (i.e., will spontaneously recover upon unloading). The presence of any RR_{OW} is an indication that martensite is stabilized due to deformation beneath the indent, even though the testing temperature is well above A_f.

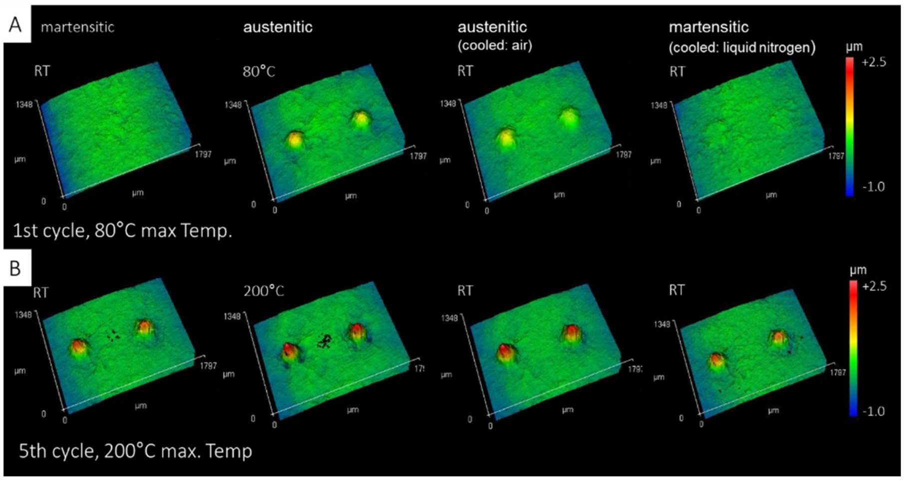

Figure 4.3: 3D Surface topography changes during subsequent temperature cycles taken via white-light-interferometry with 80, 100, 120, 160, 200 °C maximum temperature. Representative results are shown for the initial cycle with 80 °C maximum and the last cycle with 200 °C maximum temperature. A high ratio of the TWSME recovery is shown at maximum temperature of 80 °C, (A), and almost no TWSME remains after reaching the upper ‘transformation-temperature-threshold’, in this case 200 °C (B).

Several studies have shown stabilized martensite due to plastic deformation (e.g., [16-20]). It is theorized that additional heating is required to overcome a frictional effect associated with residual plasticity which prevents the deformation stabilized martensite from fully returning to austenite. For the 400 °C aged material, the volume of deformation stabilized martensite is expected to be much larger, subsequently a larger shape memory effect and RR_{OW} is found.

With additional heating and cooling cycles the reversible TWSME was only observed in the 400 °C aged sample; thus, only this material was used for the analysis of TWSME surfaces. To create TWSME surface protrusions, the sample was deformed with an array of six Vickers indents at a load of 200 N. Afterwards the deformed surface was ground and re-planarized. An interferometer was used to quantify this TWSME surface as a function of thermally cycling between ln and progressively increasing temperatures of 80, 100, 120, 160, and 200 °C. The temperature-dependent shape recovery behavior for two representative protrusions is shown in Figure 4.3. For example, only the first cycle where the sample is exposed to a maximum temperature of 80 °C (top row) and the progressively last cycle with 200 °C (bottom row) maximum temperature are shown. For the first cycle the replanarized flat sample was heated up to 80 °C, and protrusions arise after exceeding the transformation temperature. They reach approximately 1.3 µm in height and exhibit reversible TWSME behavior (Figure 4.4).

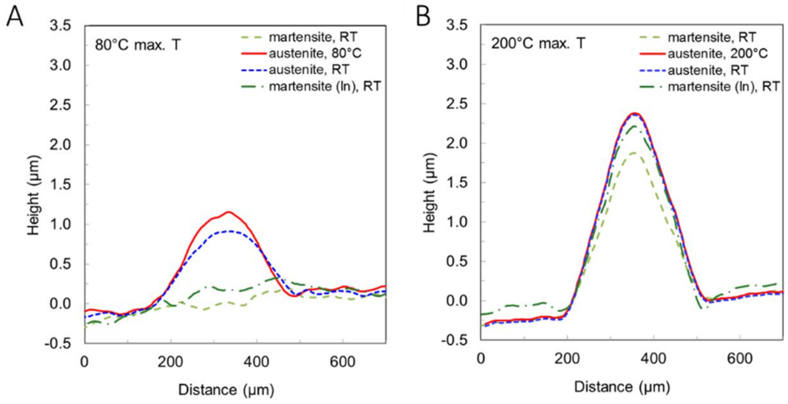

Figure 4.4. Cross-section profiles of surface protrusions after different temperature cycles. Shown are profiles of the initial martensitic state, after heating (austenitic state), after subsequent cooling in air to room temperature (austenitic state) and again after cooling with liquid nitrogen (martensitic state). (A) High reversibility is shown for lower maximum temperatures like 80 °C. (B) Increasing protrusion height is shown for higher maximum temperatures such as 200 °C. Low reversibility and remaining TWSME is shown by second cycling with 200 °C max. temperature.

They remain stable when allowed to cool in air to room temperature and disappear after cooling with ln. This phenomenon was observed to be repeatable over ten cycles. After being exposed to progressively increasing thermal cycles with a maximum temperature of 200 °C, the same protrusions become stable upon temperature cycling and did no longer illustrate the TWSME (Figure 4.3, bottom row). Owing to this no flat surface is regained after cooling with lN. Furthermore, the protrusion height in the high-temperature state at 200 °C increased to approximately 2.4 µm. The progression of the protrusion height and the protrusion height recovery as a function of the thermal cycling is summarized in Figure 4.5. It is observed that the increase in height and decrease in recovery scales with the maximum temperature until the TWSME is virtually no longer present.

To interpret the results, shown in Figure 4.4 and Figure 4.5 studies, which have investigated the TWSME have to be considered. The TWSME can be induced via preferential orientation of precipitates or thermo-mechanical training over several cycles, neither of which has been performed in this study. It can also be induced by severe plastic deformation of martensite. For indentation induced TWSME surfaces, the underlying mechanism has been hypothesized to be dislocation arrays beneath the indent, which lead to preferential martensite orientation.[4-6]

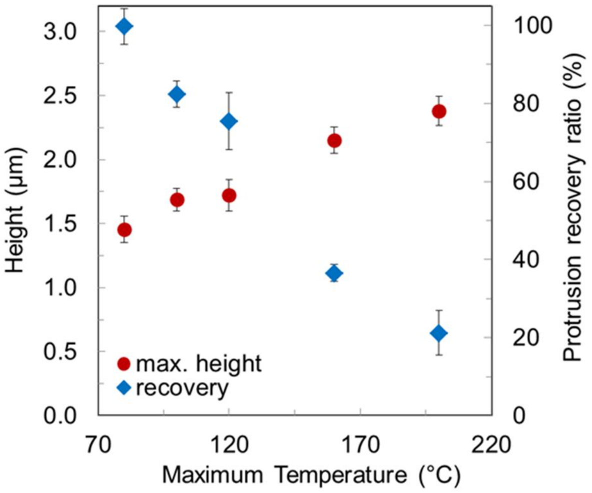

Figure 4.5. Comparison of protrusion height and recovery ratio during thermal cycling. Within increasing maximum cycle temperature, protrusion height steadily increases, while the TWSME decreases.

This hypothesis has been supported by recent TEM observations of patterns formed in NiTi via laser shock-assisted direct imprinting,[21] where a significant increase in the dislocation density is shown. However, current investigations have shown both dislocations and stabilized martensite beneath residual indents, even after thermal cycling from room temperature to 120 °C.[7] Dislocation-induced stabilized martensite has also been observed in previous work.[16-19] For the TWSME surfaces, it was theorized that the stabilized martensite acts as a nucleation point for the phase transformation, which is supported by the results shown in Figure 4.3. Although cycling progressively from 80 °C to 200 °C is not sufficient to cause significant dislocation annihilation or precipitate growth, it would be appropriate for overcoming internal friction due to dislocations structures and transforming the stabilized martensite back to austenite. Also, it is important to note that the height of the protrusions becomes larger with increasing cycle temperature (Figure 4.5), which is consistent with dislocation-stabilized martensite returning back to austenite. Consequently, it remains our belief that the stabilized martensite plays a critical role in indentation induced TWSME surfaces.

In comparison to the present work, previous investigations on TWSME surfaces have been carried out exclusively on Ti-50.3 at.% Ni material, where only martensite is stable at room temperature. It is therefore possible that the combination of testing temperature and composition may lead to different mechanisms which dictate the TWSME surfaces. Systematic investigation into the effect of composition and indentation temperature is currently underway.

4.4 Conclusions

In summary, indentation induced TWSME is only shown in the material, which was solutionized and subsequently aged at 400 °C, containing semi-coherent Ti_3Ni_4 precipitates with a size of about 100 nm. The indentation induced stress fields contribute to the activation of corresponding martensite variants.

Within thermal cycling up to moderate temperatures no tendency of fatigue was shown, the surface protrusions are highly reversible. Stepwise thermal cycling high above the transformation temperature leads to an increase of the protrusion’s heights and simultaneously to a decrease and elimination in their reversibility. Thus, the TWSME disappears at high temperatures, which lead to the assumption that stabilized martensite is critical to generate TWSME surfaces from aged Ti-50.9 at.% Ni.

4.5 Acknowledgments

The research leading to these results has received funding from the European Research Council, ERC Advanced Grant “Switch2Stick”, Agreement No. 340929, awarded to E. Arzt. CPF gratefully acknowledges support of this work from the National Science Foundation (NSF) CAREER award (grant no. DMR-1255603), as well as the University of Wyoming International Travel Grant.

4.6 References

1. Frensemeier, M.; Arzt, E.; Qin, E.; Frick, C. P.; Schneider, A. S., Indentation-induced two-way shape-memory effect in aged Ti-50.9 at.% Ni. *MRS Communications* **2015,** *5* (01), 77-82.
2. Shaw, J. A.; Kyriakides, S., Thermomechanical aspects of NiTi. *Journal of the Mechanics and Physics of Solids* **1995,** *43* (8), 1243-1281.
3. Otsuka, K.; Ren, X., Physical metallurgy of Ti-Ni-based shape memory alloys. *Progress in Materials Science* **2005,** *50* (5), 511-678.
4. Zhang, Y.; Cheng, Y. T.; Grummon, D. S., Shape memory surfaces. *Applied Physics Letters* **2006,** *89*, 041912.
5. Zhang, Y. J.; Cheng, Y. T.; Grummon, D. S., Understanding indentation-induced two-way shape memory effect. *Journal of Materials Research* **2007,** *22* (10), 2851-2855.
6. Fei, X. L.; Zhang, Y. J.; Grummon, D. S.; Cheng, Y. T., Indentation-induced two-way shape memory surfaces. *Journal of Materials Research* **2009,** *24* (3), 823-830.
7. Qin, E.; Peter, N. J.; Frensemeier, M.; Frick, C. P.; Arzt, E.; Schneider, A. S., Vickers Indentation Induced One-Way and Two-Way Shape Memory Effect in Austenitic NiTi. *Advanced Engineering Materials* **2014,** *16* (1), 72-79.
8. Gall, K.; Sehitoglu, H.; Chumlyakov, Y. I.; Kireeva, I. V., Tension–compression asymmetry of the stress–strain response in aged single crystal and polycrystalline NiTi. *Acta Materialia* **1999,** *47* (4), 1203-1217.
9. Gall, K.; Sehitoglu, H.; Chumlyakov, Y. I.; Kireeva, I. V.; Maier, H. J., The influence of aging on critical transformation stress levels and martensite start temperatures in NiTi: Part I - Aged microstructure and micro-mechanical modeling. *Journal of Engineering Materials and Technology - Transactions of the ASME* **1999,** *121* (1), 19-27.
10. Liu, Y.; Yang, H.; Voigt, A., Thermal analysis of the effect of aging on the transformation behaviour of Ti–50.9 at.% Ni. *Materials Science and Engineering: A* **2003,** *360* (1), 350-355.
11. Khalil-Allafi, J.; Dlouhy, A.; Eggeler, G., Ni 4 Ti 3-precipitation during aging of NiTi shape memory alloys and its influence on martensitic phase transformations. *Acta Materialia* **2002,** *50* (17), 4255-4274.
12. Frick, C. P.; Ortega, A. M.; Tyber, J.; Maksound, A. E. M.; Maier, H. J.; Liu, Y. N.; Gall, K., Thermal processing of polycrystalline NiTi shape memory alloys. *Materials Science and Engineering a-Structural Materials Properties Microstructure and Processing* **2005,** *405* (1-2), 34-49.
13. Ni, W.; Cheng, Y.-T.; Grummon, D. S., Recovery of microindents in a nickel–titanium shape-memory alloy: a “self-healing” effect. *Applied Physics Letters* **2002,** *80* (18), 3310-3312.
14. Shaw, G.; Stone, D.; Johnson, A.; Ellis, A.; Crone, W., Shape memory effect in nanoindentation of nickel–titanium thin films. *Applied Physics Letters* **2003,** *83* (2), 257-259.
15. Otsuka, K.; Wayman, C. M., *Shape memory materials*. Cambridge university press: **1999**.
16. Lin, H.; Wu, S.; Chou, T.; Kao, H., The effects of cold rolling on the martensitic transformation of an equiatomic TiNi alloy. *Acta Metallurgica Et Materialia* **1991,** *39* (9), 2069-2080.
17. Liu, Y.; Favier, D., Stabilisation of martensite due to shear deformation via variant reorientation in polycrystalline NiTi. *Acta Materialia* **2000,** *48* (13), 3489-3499.

18. Mahmud, A. S.; Yang, H.; Tee, S.; Rio, G.; Liu, Y., Effect of annealing on deformation-induced martensite stabilisation of NiTi. *Intermetallics* **2008,** *16* (2), 209-214.
19. Laplanche, G.; Pfetzing-Micklich, J.; Eggeler, G., Orientation dependence of stress-induced martensite formation during nanoindentation in NiTi shape memory alloys. *Acta Materialia* **2014,** *68*, 19-31.
20. Pfetzing, J.; Schaefer, A.; Somsen, C.; Wagner, M. F.-X., Nanoindentation of pseudoelastic NiTi shape memory alloys: Thermomechanical and microstructural aspects. *International Journal of Materials Research* **2009,** *100* (7), 936-942.
21. Ye, C.; Cheng, G. J., Scalable patterning on shape memory alloy by laser shock assisted direct imprinting. *Applied Surface Science* **2012,** *258* (24), 10042-10046.

Chapter 5

Shape memory topographies on nickel-titanium alloys trained by embossing and pulse electrochemical machining

Abstract - Nickel-titanium (NiTi) shape memory alloys are of strong interest for applications in aerospace, for biomedical purposes, and in general micro engineering technologies due to their pseudoelastic and shape recovery properties. While the pseudoelastic and the one-way shape memory effect are both already in application, less emphasis has been placed on the reversible intrinsic two-way shape memory effect (TWSME), which requires complicated training procedures. In this study we demonstrate two approaches to obtain switchable surface structures using the TWSME in a martensitic Ti-50.3 at. % Ni alloy. NiTi samples were structured using two different surface geometries by either cold embossing, or by pulse electrochemical machining (PECM). After planarization of the structures, a change of the topography from optically smooth to structured and vice versa is observed using white light interferometry. The switch is induced via heating and cooling of the sample above and below the phase transformation temperature. The emerging protrusions reflect the characteristic pattern applied by the embossing and the PECM process. Both methods are promising for preparation of switchable metallic surfaces on larger areas.

This chapter was published in *Advanced Engineering Materials (2016)*,[1]

5.1 Introduction

Nickel-titanium (NiTi) shape memory alloys are capable of recovering their previously defined shape after certain deformation at temperatures above their characteristic transformation temperature. This shape change is due to the one-way shape memory effect (OWSME), which has its origin in a stress-induced martensitic phase transformation below the austenite start temperature and the reverse transformation upon heating.[2] Due to a coordinated displacement in the atomic structure, a completely reversible deformation, even for large strains up to approximately 3-8%, can be induced.[3] By combining deformation processing and specific heat treatment it is possible to induce an intrinsic two-way shape memory effect (TWSME).[4-5] This effect allows a reversible shape change as a function of cycling temperature without external restoring force.

Studies by Zhang et al. have shown that a TWSME can be induced on a NiTi surface using an indentation method, which leads to switchable surface protrusions.[6-8] Near equiatomic NiTi samples were indented, heated above the transformation temperature, cooled down again and then planarized by grinding and polishing. When the planarized sample was heated above the transformation temperature, protrusions formed on the sample surface and disappeared after the sample was cooled back to room temperature. This phenomenon was found to be repeatable over multiple temperature cycles. The protrusions were attributed to preferentially oriented dislocation structures in proximity to the former indentation site. We recently performed a microstructural study of Ti-50.9 at. % Ni shape memory surfaces after indentation and found both dislocations and thermally stabilized martensitic plates oriented along to the indents.[10] It was proposed that the stabilized martensite acts as a nucleation site for the TWSME and is crucial for inducing reversible surface protrusions. All these studies suggest that alloys with a TWSME are, in principle, able to reversibly change their surface topography as a function of temperature. As many physical properties depend on the surface structure of a material, a switchable surface geometry may be used to achieve a switchable functionality.

A TWSME surface with a reversible change from flat to a structured topography may lead to new applications in the field of tribology, in microfluidics and in biomedical devices.[10-12] However, implementation and testing of new functionalities usually requires larger surface areas. The conventional preparation technique via individual indents or scratches is time-consuming and difficult to scale up.[6] Liu et al. used a layer of packed soda lime glass balls to indent an array of holes simultaneously into a shape memory polymer leading to an array of micro protrusions.[13] This cost and time-efficient method is limited to spherical protrusion geometry and may only be applied to soft polymeric shape memory materials. NiTi shape memory alloys, in contrast, show poor formability[14-15], which is counterproductive for achieving a precise deformation geometry and subsequently a well-defined shape change of the NiTi surface. Therefore, the purpose of this study is to expand the limited preparation techniques on TWSME surfaces to methods which can be applied on larger scales and allow high localized deformation at the same time.

In this study, two plastic forming approaches are pursued to facilitate and optimize the preparation of surfaces with TWSME in a martensitic Ti-50.3 at. % Ni alloy. In the first approach, the NiTi alloy is trained by cold embossing using a metallic micro-mesh as a template. The remaining deformation after embossing is removed by mechanical grinding. In the second approach, the NiTi alloy is pre-patterned using pulse electrochemical machining (PECM) and subsequent planarization via compression with a smooth work piece. The PECM process allows comparatively fast formation of stress-free surface structures with high accuracy and without generation of heat,[16] which is beneficial for large area training of the indentation induced TWSME of NiTi alloys.[17-19]

5.2 Experimental

Embossing: A polycrystalline NiTi shape memory alloy composed of Ti-50.3 at.% Ni (Ti- 55.47 wt.% Ni) was procured from Memry GmbH (Germany). The phase transformation temperatures were measured by differential scanning calorimetry (DSC) using a Mettler Toledo DSC1 Star System. The martensite finish temperature (M_f) is about 25°C, and the austenite finish temperature (A_f) is about 76°C. A two-millimeter thick NiTi sheet was cut into pieces of 10 x 10 mm and discs of 10 mm diameter. The NiTi samples were ground using 2500 grade SiC paper, followed by several mechanical polishing steps down to 1 µm diamond paste, and oxide polishing with an OP-S suspension (Struers, Germany). The resulting average surface roughness (R_a) was 0.04±0.006 µm, measured by white light interferometry (Zygo NewView 5000, Kyoto, Japan).

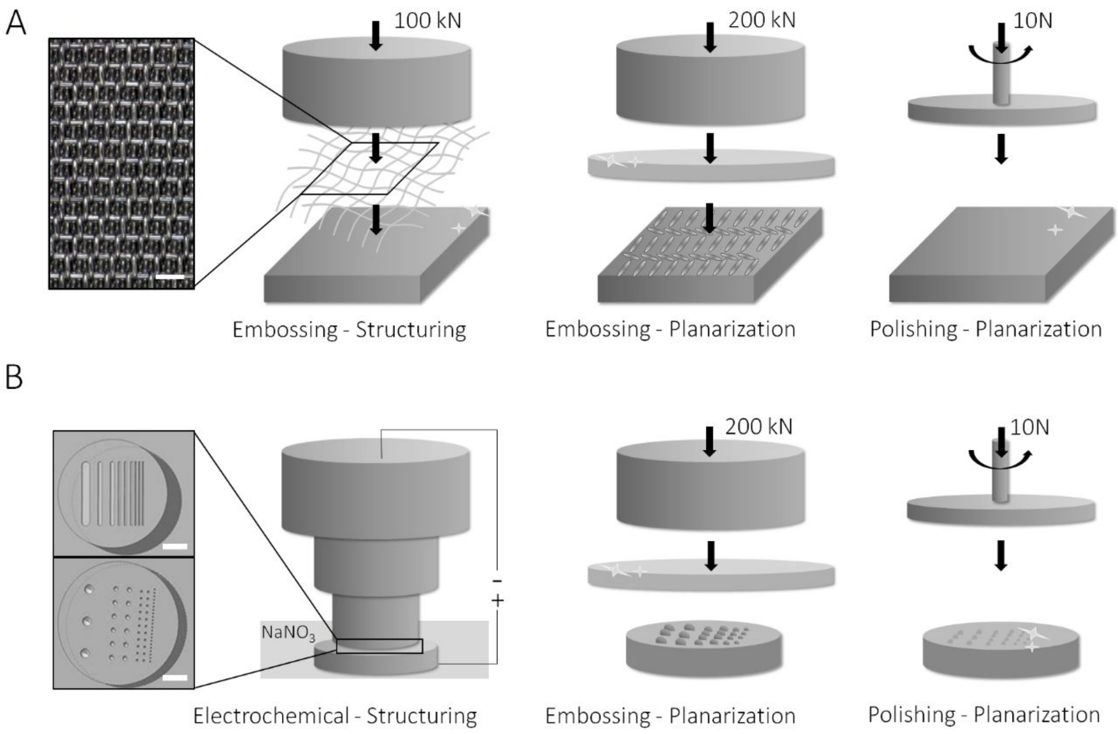

Figure 5.1: Schematic of the two preparation techniques for shape memory surfaces. (A), cold embossing using a metallic micro-mesh, the result of which is demonstrated in the optical micrograph (inset). (B), pulse electrochemical micromachining of a NiTi surface with two structured tools with grooves and with holes of different sizes.

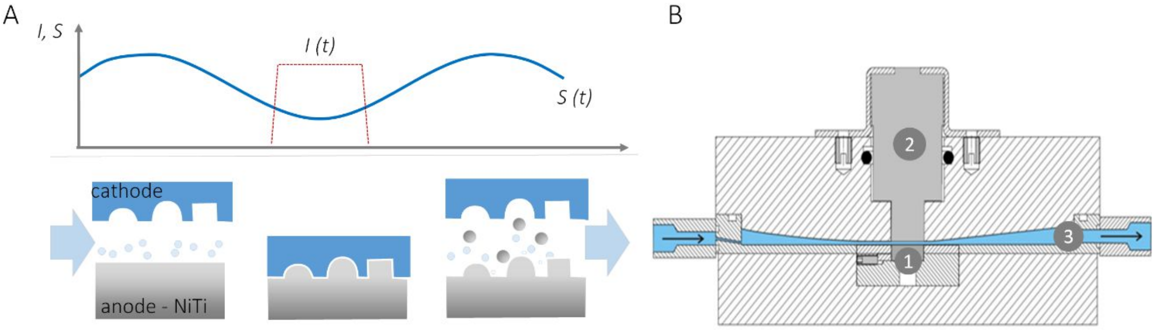

Figure 5.2: Schematic drawing of the PECM process and resulting surface texture. (A) The cathode is moved in a sinusoidal manner to widen the interelectrode-gap (S, gap distance) to the anode. A short pulse (I, current pulse) is applied at the lower turning point. (B) Experimental PECM-Setup. 1: NiTi sample, 2: tool cathode, 3: electrolyte flow. Modified after [20],[21].

Cold embossing was performed in a hydraulic press (Paul-Otto-Weber GmbH) using a metallic micro-mesh. The cloth-like mesh was made from fine stainless steel wires, procured from Haver & Boecker (TRD 75) with a mesh size of 75 µm and cloth thickness of 260 µm, (Figure 5.1, A). Three samples were embossed with at a load of 100 kN for 10 s. The samples were then planarized in two steps, using an optically smooth hard metal work piece and an active oxide suspension for polishing (OP-S Suspension, Struers, Germany) to regain an average roughness of 0.05±0.005 µm.

Pulse Electrochemical Machining: The polished NiTi discs, representing the anode of the setup, were fixated in the flushing chamber of a PEMCenter8000 (PEMTec SNC, France). Two different tools, one with a pattern of grooves and one with holes as shown in Figure 5.1, (B) were prepared via drilling and milling from stainless steel and were used as a cathode. The faces of the two stainless steel tools had a diameter of 12 mm. The holes of 1 cm depth had diameters 150, 250, 500, and 1000 µm; the size of the grooves was 120, 150, 250 and 500 µm at a depth of 250 µm. The electrolyte was axially fed up through a flushing chamber (Figure 5.2) so that uniform flushing conditions were obtained in the interelectrode gap, which was set at an initial size of 30 µm. A sodium nitrate ($NaNO_3$) electrolyte, with an electrical conductivity of 72 $mScm^{-1}$ at 21 °C and a pH value of 7.2, was pumped into the gap at a flow rate of 10 $Lmin^{-1}$ and a pressure of 250 kPa. The amplitude of the cathode vibration was 373 µm. The applied voltage amplitude was set to 12.8 V, the electrical pulse on-time to 2.5 ms, the electrical and mechanical pulse frequencies to 50 Hz and the cathode feed rate to 0.27 $mmmin^{-1}$. The angular phase shift between the bottom dead center of the mechanical vibration and the triggering of the electrical current impulse was set to 0.65. During the machining process, the surface patterns of the cathode were negatively transferred to the anode.

The surface morphology of the PECM samples was analyzed by scanning electron microscopy using an FEI Versa 3D Dual Beam (Oregon, USA) microscope. Topography measurements were carried out by white-light interferometry in a 3-D optical microscope (Keyence, VHX 2000D, Japan).

Subsequently, the surface structures on the NiTi surface were compressed with the smooth hard metal work piece at a load of 200 kN. The remaining surface roughness was mechanically and chemically polished as described above for cold embossing.

The shape memory behavior was investigated by thermal cycling and in-situ characterization of the surface topography. Heating and cooling was conducted with a Peltier heating and cooling stage (Linkam, PE 120, UK), which was installed in the white light interferometer for in situ topography measurements. Experiments were made at room temperature (23°C), at 80°C, and again after cooling down to room temperature. The temperatures were chosen to be above and below the phase transformation temperatures of the alloy. White light interferometry images were taken after hold times of one minute to ensure a homogenous temperature distribution.

5.3 Results and discussion

Cold Embossing: Figure 5.3 shows optical micrographs of the micro-mesh, before (A) and after (B) embossing, and of the deformed NiTi substrate (C). The high compression force and the hardness of the NiTi surface have led to the deformation of both, mesh and sample surface. The NiTi sample shows a clear surface deformation in form of a mesh-like pattern. White light interferometry measurements of the deformed NiTi surface exhibit a surface pattern with a peak to valley distance of about 11 µm and a width of the grooves between 100 and 200 µm.

The surface topography after planarization is shown in Figure 5.4. No clear pattern is visible at room temperature (A), after heating the sample up to 80°C a mesh-like pattern (B) appears on the surface. To test for the switchability and the reversibility, white light interferometry measurements were taken at room temperature, at 80°C, and again after cooling down to room temperature. Figure 5.4 shows the topography at room temperature (C), after heating (D), and after cooling down again (E). As soon as the temperature was increased above the phase transformation temperature, a significant mesh-like pattern appeared with structure features of approximately 2 to 3 µm in height. The average surface roughness R_a increased from 0.04±0.006 µm at room temperature to 0.69 ±0.023 µm in the heated state, and recovered to 0.08 ±0.007 µm after cooling back to room temperature. During further heating and cooling cycles, the sample switched reversibly between states (D) and (E).

The switchability and reversibility of the surface structures indicate that embossing a pattern with subsequent re-planarization by a second compression step induces a TWSME. Consequently, a relatively large area may be structured by a simple two-step process in short time compared to single indentations with subsequent grinding. Furthermore, a significant change in the average roughness was measured depending on the sample temperature.

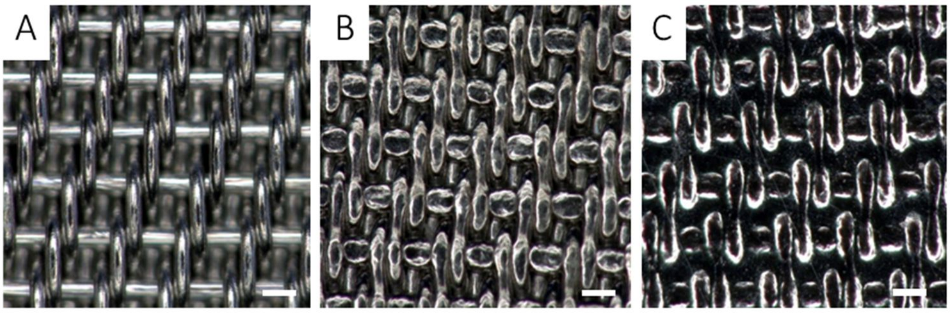

Figure 5.3: The images of the cold embossing preparation steps were taken by 3D-optical microscopy and show (A) the metallic micro-mesh before embossing, (B) the micro-mesh after embossing, and (C) the corresponding surface deformation of the NiTi sample. The scale bar corresponds to 100 µm.

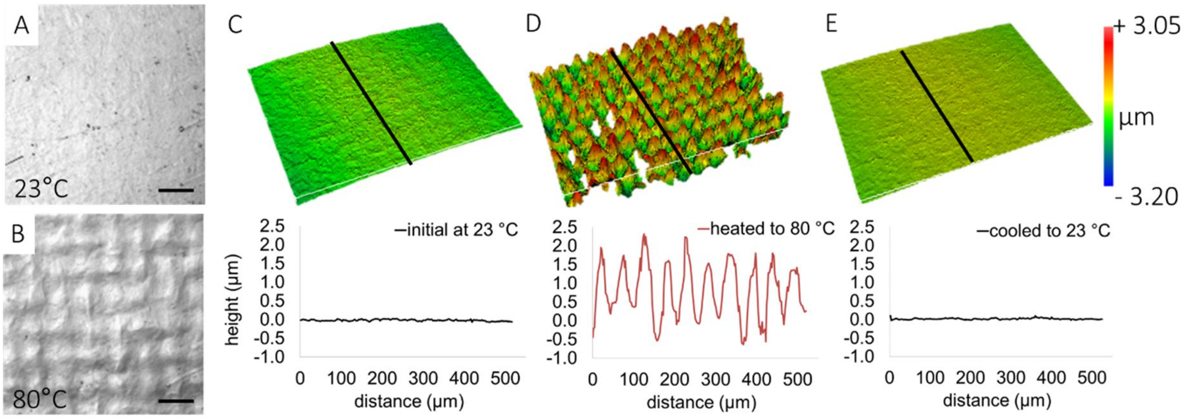

Figure 5.4: Optical micrographs and White light interferometry of switchable topography using cold embossing. (A) and (C) correspond to the embossed and re-planarized surface at room temperature,(B) and (D) exhibit the appearing mesh structure upon heating to 80°C. (E) demonstrates the recovered flat surface after cooling back to room temperature. The cross section profiles (black line) of the three different topographies are shown below. The scale bar corresponds to 100 µm.

Pulse Electrochemical Machining: The optical microscopy and SEM images in Figure 5.5 exhibit the resulting four different sizes of lines and bumps on the NiTi sample surface after the PECM process. Apart from a darker optical appearance due to oxide formation, the space between the protrusions is smooth and non-structured; a clear separation of structured and unstructured area was achieved proving that plastic deformation was highly localized and defined.

The SEM images suggest that the definition of edges of the protrusions formed decreases with decreasing feature size. The edges of the smallest protrusions are hardly visible and their dimensions are difficult to determine.

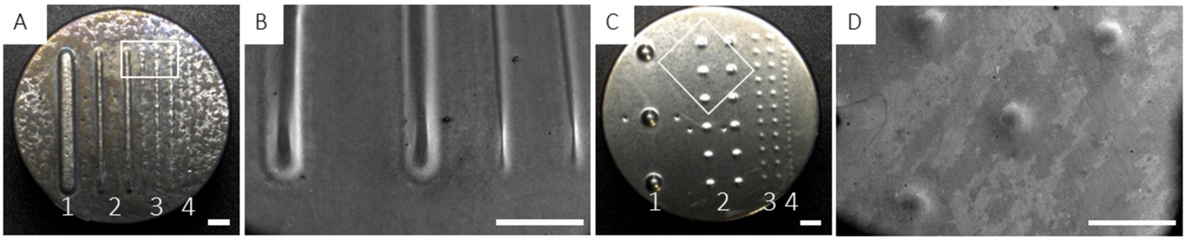

Figure 5.5: Optical and SEM micrographs of the surface structures formed by PECM. Lines and semispherical structures were transferred onto the NiTi samples by PECM. (B) and (D) show a close up of the marked section, focusing on the spherical protrusions and the edges of the linear pattern. The scale bar corresponds to 1 mm.

Table 5.1: Dimensions of the cathode structures and the electrochemically processed structures on the NiTi sample: The initial geometries made by PECM are compared to the geometries of the switchable surface structures upon heating the NiTi sample to 80°C.

structure No.	**Cathode**		**PECM**		**TWSME at 80°C**	
LINES	width	depth	width	height	width	height
1	500 ± 1 µm	250 ± 1 µm	608 ± 5 µm	190 ± 4 µm	1341 ± 5 µm	22 ± 4µm
2	250 ± 1 µm	250 ± 1 µm	310 ± 17 µm	111 ± 10 µm	775 ± 14 µm	4 ± 1 µm
3	150 ± 1 µm	250 ± 1 µm	337 ± 2 µm	49 ± 3 µm	692 ± 15 µm	3 ± 1 µm
4	120 ± 1 µm	250 ± 1 µm	207 ± 36 µm	26 ± 3 µm	368 ± 16 µm	3 ± 1 µm
BUMPS						
1	1000 µm	1000 µm	961 ± 18 µm	247 ± 4 µm	1295 ± 11 µm	9 ± 1 µm
2	500 µm	1000 µm	806 ± 64 µm	73 ± 1 µm	631 ± 24 µm	3 ± 0.3 µm
3	250 µm	1000 µm	723 ± 60 µm	15 ± 1 µm	554 ± 29 µm	2 ± 0.2 µm
4	150 µm	1000 µm	325 ± 5 µm	8 ± 0.4 µm	-	-

More precise information on the dimensions of the protrusions was obtained by white light interferometry measurements on the switchable TWSME protrusions in the heated state, and on the counterpart structure of the cathode (Table 5.1). The measurements show that the lines formed range from 26 ±3 to 190 ±4 µm in height and from 207 ±36 to 608 ±5 µm in width. The bumps range from 8 ±1 to 247 ±4 µm in height and from 372 ±5 to 1198 ±12 µm in width.

For better comparability of the PECM structuring accuracy, a form deviation Δl is defined as

$$\Delta l = \frac{|l_s - l_c|}{l_c} \tag{5.1}$$

where l_s is the length of the cross-section of the structure at the base and l_c is the length of the diameter of the cavity in the cathode. For $\Delta l = 0\%$, the protrusion exactly matches the diameter of the counterpart in the cathode (Figure 5.6, A). The results in Figure 5.6 (C) show that the form deviation increases with decreasing feature size. In most cases the structures are much larger than their counterpart, reaching values of Δl as high as 190±24 %.

The aspect ratio a_s of the structures is defined as

$$a_s = \frac{h_s}{l_s} \tag{5.2}$$

where h_s is the height of the structure (Figure 5.6, B).

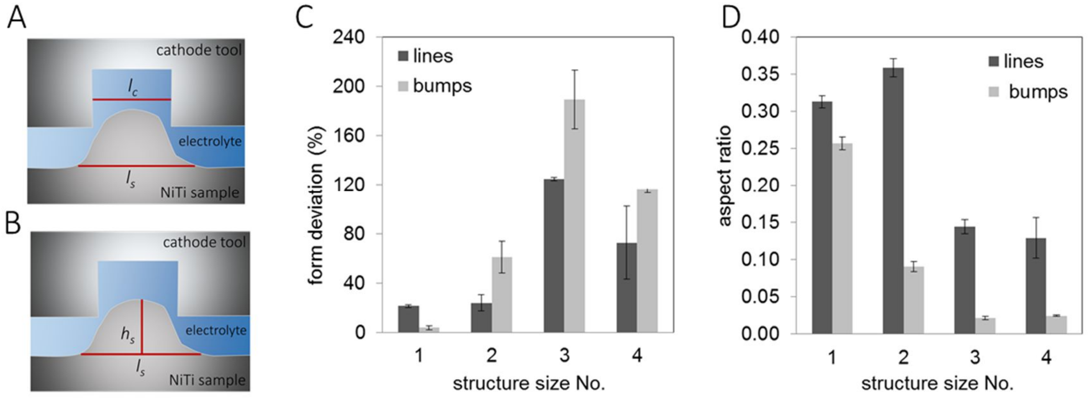

Figure 5.6: (A and B) Schematic of interelectrode gap in the PECM process. (C) Form deviation of the lines and semispherical protrusions formed by PECM, listed for each size category. (D) Aspect ratio for the structures made by PECM in each size category.

The aspect ratios of the protrusions, in this case of the lines and bumps in the four different size categories, are shown in Figure 5.6 (D): they decrease with decreasing size from 0.36 ±0.01 for lines of structure size no. 2 to 0.13 ±0.03 for size no. 4. Overall the bumps show a smaller aspect ratio compared to the cross section of the lines, which was expected because of the low contrast in the SEM and optical microscopy images. Their aspect ratio decreases from 0.26 ±0.01 to 0.02 ±0.001.

To explain the deviation between the form of the cathode and the resulting surface pattern, the following aspects have to be considered. The shape evolution on the sample depends on the current density distribution and the mass transport; to achieve a structuring effect also the current distribution on the work piece plays an important role. Therefore, a small gap size and a homogeneous flow of the electrolyte are crucial for precise manufacturing via PECM. [19, 22-23] The gap size of the cathode and the NiTi surface slightly increases during the anodization process leading to an ill- defined boundary geometry between the processed and unprocessed areas in the smaller structures. A similar deviation in processing accuracy of grooves with different size in NiTi is shown by *Lee et al.* using PECM.[18] As shown in Figure 5.6, the aspect ratios of the formed protrusions decrease with structure size, while a widening of the structures occurs. The variation of structure size and spacing on the same cathode leads to lower current densities for the smaller structures, causing a less precise material removal in comparison to the larger protrusions.[24] The smaller gap size between the edges of the cathode features and the sample surface leads to stronger anodic dissolution than the bottom of the features, with a depth of 500 and 1000 µm.[19, 25] The analysis of form deviation and aspect ratio is a convenient method to characterize the two-way shape memory effect induced by the compression of surface structures.

Subsequently the protrusions formed by PECM were compressed into the sample surface using the work piece. As shown in Figure 5.7, polishing led to an optically smooth, nearly flat surface at room temperature (A and C). During heating up to 80°C, the specific surface arrays appeared, as shown in Figure 5.7 (B) and (D). After cooling the sample back to room temperature, the arrays disappeared and the surface recovered its optically smooth state. The images in Figure 5.7 show an exemplary switch of the patterned array after ten heating and cooling cycles, indicating high reversibility.

Two exemplary white light interferometry measurements of the linear and semispherical protrusions are shown in Figure 5.8. They confirmed that both geometries deformed reversibly. The height of the two linear structures (Figure 5.5, A

No. 3; Figure 5.8 A) increased upon heating from 1.2 to 2.8 µm and 2.4 µm in height and showed a width of 690 and 675 µm. After cooling back to room temperature, the lines recovered their initial profile. The exemplary measurements of the spherical protrusions (Figure 5.5, C No. 3; Figure 5.8, B) showed a similar behavior. The bump increased from 0.7 to 2.1 µm in height with a width of 561 µm and decreased after cooling to the initial state.

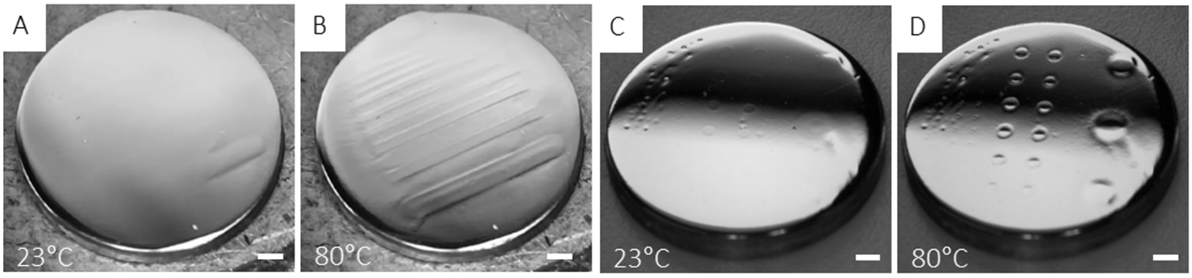

Figure 5.7: Optical micrographs showing the switchable topographies. (A and C) The planarized samples at room temperature. (B and D) A change in topography is observed in the heated state. The optically smooth surface shows a linear and spherical pattern. This change in topography can be reversibly switched by temperature cycling. Scale bar 1 mm.

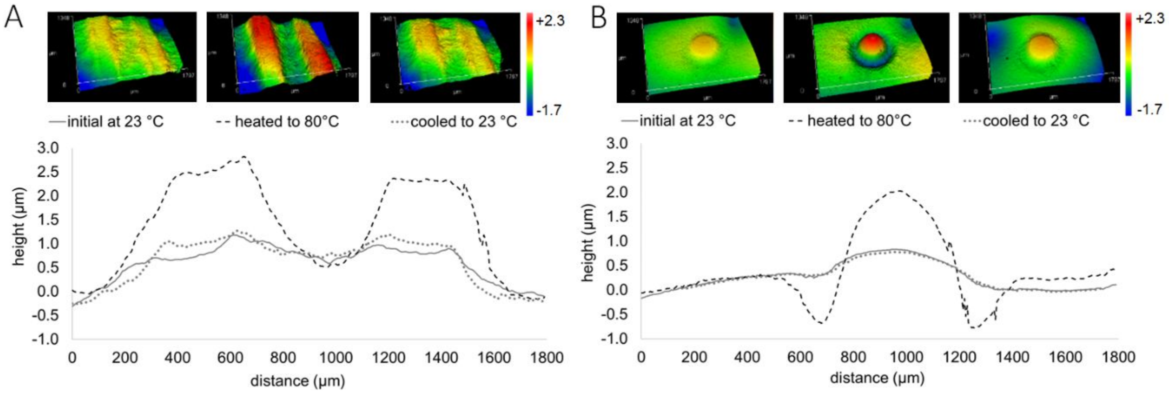

Figure 5.8: 3-D topography images and the according cross section profiles from white light interferometry measurements. An exemplary linear (A) and spherical protrusion (B) are shown for one temperature cycle. Both types of arrays, show reversible protrusions which appear in the heated state and recover in the cooled state

The dimensions of the switchable TWSME protrusions in the heated state at 80°C are listed for all four size categories in Table 5.1. Only the smallest bump structures (size No. 4) could not be detected, since no protrusions appeared in the heated state.

An interesting feature to be noted is the lowering of the edge for the spherical protrusions in the heated state, leading to a circular groove around the bump. In the displayed example the depth of the groove is about 0.7 µm leading to height change of 2.8 µm measured from peak to valley. Thus, upon heating the surface shows two different deformation directions induced by one single compressive pre-deformation.

This effect is not reported in literature so far and results from the present preparation technique. Due to the compression of material into the surface a complex deformation field is extended underneath, and surrounding, the former PECM structures, which may be considerably more complex than that of a quasi-static indentation. For simplification, we assume that the deformation field resulting from compression of the PECM structures is comparable to that of a flat punch indentation. For this case *Murthy et al.* revealed a variation of texture indicating a state of simple shear right at the corner of the flat punch, in our case the edge of the PECM structures.[25] Meanwhile, a state of plane-strain compression was observed directly underneath the flat punch. Applied to our situation, the state of plain-strain will be located centrally below the PECM structure. Based on this we assume a stagnation of material flow underneath the compressed structures, a presence and orientation of shear bands, and transitions in plastic modes between shear and compression.[25]

The deformation behavior of NiTi shape memory alloys was shown to be asymmetric in tension and compression, and intrinsic stress fields and defects, which stabilize stress induced martensite, are considered to be fundamental for the indentation induced TWSME. [27-29] Therefore it can be assumed that the change in deformation modes below the compressed PECM structures, from plane strain compression to highly strained shear mode, may influence the deformation behavior of the shape memory alloy.[30] Thus, the presence of two different deformation modes in the area of the compressed PECM structure may have led to different stress fields and defects which induce the bidirectional deformation after the phase transformation.

Consequently, the present preparation technique enables the fabrication of switchable surface arrays with a bidirectional extension of protrusions, which is promoted by high strain rates in the dynamic regime and a tailored microstructure.

Having shown that a TWSME can be induced by compression of PECM processed structures we now compare our results to other studies. *Fei et al.* reported that the average indentation depth using spherical indenters was 40 times the height of the switchable protrusions obtained by the TWSME.[29] Hence the height of switchable protrusions was found to be 2.4 % of the indentation depth. For comparison we assume, that the height of the structures formed by PECM equals the indentation depth, since the structures should be fully compressed into the surface. Following this assumption the height of the switchable protrusions was found to range from 3.4 % to 14.3 % of the indentation depth. This in turn means that a shallower deformation depth is needed to receive the same height of reversible TWSME structures by applying the present technique. Additionally, the surface structuring by PECM followed by compression allows formation of relatively large TWSME arrays at the same time compared to conventional single indentation techniques. Due to the planarization via compression of the structures, less material needs to be removed during the grinding steps. In the present case, one mechanical and chemical polishing step was sufficient to receive an optically smooth surface.

5.4 Conclusions

This study presents two approaches on the fabrication of switchable surface arrays on NiTi shape memory alloys. Based on the principle of the indentation induced two-way shape memory effect, cold embossing and pulsed electrochemical machining with subsequent structure compression, are used to simplify preparation of different reversible surface patterns. In addition patterning of larger areas at the same time was enabled.

» The two step process of embossing and re-planarization of a metallic micromesh leads to a reversible change in surface roughness on the micrometer scale with specific geometric features and stable recovery. This method facilitates the preparation technique for large areas and could enable applications of switchable surface arrays in tribology, switchable adhesion, or biomedicine.[31-33]

» Pulsed Electrochemical Machining plays in important role in NiTi processing due the oxidation and deformation free formation of complex microstructures without thermal damage or distortion.[34] In the present work we revealed that a formation of different protruding structures on a NiTi surface was possible via PECM using a tool of holes and grooves.

» We induced a TWSME by compression of surface structures. After subsequent polishing, arrays with switchable topographies were shown upon heating and cooling the sample above and below its transformation temperatures.

» Additional to a protruding deformation dimension of the topography, a 'sink-in' of the surrounding area – a bidirectional deformation – was observed. Subsequently, two different highly strained regions were induced by the compression of structures, leading to opposite deformation directions during phase transformation. This phenomenon might be attributable to the heterogenic deformation field extending below the PECM structures after compression and the asymmetric deformation behavior of NiTi on compression or shear mode. To confirm these assumptions, a detailed analysis of the microstructure and crystallographic texture in the deformation area has to be conducted.

A fundamental understanding of the factors guiding the different deformation orientations during transformation would enable a more elaborate and coordinated switching of grooves and protrusions.

As mentioned by *Zhang et al.* a switchable roughness might be of interest for applications in tribology.[10] The surface texture can be varied as a function of temperature, actively by heating above the transformation temperature, or passively for example during breaking events using the friction induced heat. The change in surface geometry can then be used to control friction. In addition to the change in topography, the phase transformation itself, from martensite to austenite, may contribute positively to increase wear resistance of the NiTi alloy.[35]

5.5 Acknowledgments

The author thanks the mechanical workshop of the INM for the tool fabrication and D. Schirra for his support with white light interferometry measurements. The PECM process was conducted at the Zentrum für Mechatronik und Automatisierungstechnik, Saarbrücken under the supervision of M. Weinmann and O. Weber.

The research leading to these results was conducted within a Grant of the European Research Council, ERC Advanced Grant "Switch2Stick", Agreement No. 340929, awarded to E. Arzt.

5.6 References

1. Frensemeier, M.; Schirra, D.; Weinmann, M.; Weber, O.; Kroner, E., Shape-Memory Topographies on Nickel–Titanium Alloys Trained by Embossing and Pulse Electrochemical Machining. *Advanced Engineering Materials* **2016**, DOI: 10.1002/adem.201600012
2. Otsuka, K.; Wayman, C. M., Shape memory materials. *Cambridge university press*: **1999**.
3. Shaw, J. A.; Kyriakides, S., Thermomechanical aspects of NiTi. *Journal of the Mechanics and Physics of Solids* **1995,** *43* (8), 1243-1281.
4. Perkins, J., Residual stresses and the origin of reversible (two-way) shape memory effects. *Scripta Metallurgica* **1974,** *8* (12), 1469-1476.
5. Otsuka, K.; Ren, X., Physical metallurgy of Ti-Ni-based shape memory alloys. *Progress in Materials Science* **2005,** *50* (5), 511-678.
6. Zhang, Y.; Cheng, Y. T.; Grummon, D. S., Shape memory surfaces. *Applied Physics Letters* **2006,** *89*, 041912.
7. Zhang, Y.; Cheng, Y.-T.; Grummom, D. S., Novel tribological systems using shape memory alloys and thin films. *Surface and Coatings Technology* **2007,** *202* (4–7), 998-1002.
8. Fei, X. L.; Zhang, Y. J.; Grummon, D. S.; Cheng, Y. T., Indentation-induced two-way shape memory surfaces. *Journal of Materials Research* **2009,** *24* (3), 823-830.
9. Qin, E.; Peter, N. J.; Frensemeier, M.; Frick, C. P.; Arzt, E.; Schneider, A. S., Vickers Indentation Induced One-Way and Two-Way Shape Memory Effect in Austenitic NiTi. *Advanced Engineering Materials* **2014,** *16* (1), 72-79.
10. Zhang, Z.; Zhu, D.; Qu, N.; Wang, M., Theoretical and experimental investigation on electrochemical micromachining. *Microsystem Technologies* **2007,** *13* (7), 607-612.
11. Sun, T.; Wang, G.; Feng, L.; Liu, B.; Ma, Y.; Jiang, L.; Zhu, D., Reversible Switching between Superhydrophilicity and Superhydrophobicity. *Angewandte Chemie International Edition* **2004,** *43* (3), 357-360.
12. Ebara, M., Shape-memory surfaces for cell mechanobiology. *Science and Technology of Advanced Materials* **2015,** *16* (1), 014804.
13. Liu, N.; Xie, Q.; Huang, W.; Phee, S.; Guo, N., Formation of micro protrusion arrays atop shape memory polymer. *Journal of Micromechanics and Microengineering* **2008,** *18* (2), 027001.
14. Li, D. Y., A new type of wear-resistant material: pseudo-elastic TiNi alloy. *Wear* **1998,** *221* (2), 116-123.
15. Jialing, J., Wear resistance of Ni-Ti alloy. *Acta Metall Sin* **1988,** *24* (1), 66-70.
16. Weber, O.; Natter, H.; Bähre, D., Pulse electrochemical machining of cast iron: a layer-based approach for modeling the steady-state dissolution current. *Journal of Solid State Electrochemistry* **2015,** *19* (5), 1265-1276.
17. Spieser, A.; Ivanov, A., Recent developments and research challenges in electrochemical micromachining (μECM). *The International Journal of Advanced Manufacturing Technology* **2013**, 1-19.
18. Lee, E.-S.; Shin, T.-H.; Kim, B.-K.; Baek, S.-Y., Investigation of short pulse electrochemical machining for groove process on Ni-Ti shape memory alloy. *International Journal of Precision Engineering and Manufacturing* **2010,** *11* (1), 113-118.

19. Kock, M.; Kirchner, V.; Schuster, R., Electrochemical micromachining with ultrashort voltage pulses–a versatile method with lithographical precision. *Electrochimica Acta* **2003,** *48* (20–22), 3213-3219.
20. Weinmann, M. Elektrochemische Erzeugung dreidimensionaler Strukturen. Dissertation, Universität des Saarlandes, Saarbrücken, **2014**.
21. Zapp, N.; Weber, O.; Natter, H., Corrosion-and Electrochemical Dissolution Behavior of Cast Iron Measured with Different Electrochemical Cell Types. *International Journal of electrochemical Science* **2015,** *10* (7), 5434-5455.
22. Rosenkranz, C.; Lohrengel, M. M.; Schultze, J. W., The surface structure during pulsed ECM of iron in NaNO3. *Electrochimica Acta* **2005,** *50* (10), 2009-2016.
23. Landolt, D.; Chauvy, P. F.; Zinger, O., Electrochemical micromachining, polishing and surface structuring of metals: fundamental aspects and new developments. *Electrochimica Acta* **2003,** *48* (20–22), 3185-3201.
24. West, A. C.; Matlosz, M.; Landolt, D., Normalized and Average Current Distributions on Unevenly Spaced Patterns. *Journal of The Electrochemical Society* **1991,** *138* (3), 728-735.
25. Datta, M.; Landolt, D., Fundamental aspects and applications of electrochemical microfabrication. *Electrochimica Acta* **2000,** *45* (15), 2535-2558.
26. Murthy, T. G.; Saldana, C.; Hudspeth, M.; M'Saoubi, R. In *Deformation field heterogeneity in punch indentation*, Proceedings of the Royal Society of London A: Mathematical, Physical and Engineering Sciences, The Royal Society: **2014**; p 20130807.
27. Gall, K.; Sehitoglu, H., The role of texture in tension–compression asymmetry in polycrystalline NiTi. *International Journal of Plasticity* **1999,** *15* (1), 69-92.
28. Frensemeier, M.; Arzt, E.; Qin, E.; Frick, C. P.; Schneider, A. S., Indentation-induced two-way shape-memory effect in aged Ti-50.9 at.% Ni. *MRS Communications* **2015,** *5* (01), 77-82.
29. Fei, X.; Grummon, D. S.; Ye, C.; Cheng, G. J.; Cheng, Y.-T., Surface form memory in NiTi shape memory alloys by laser shock indentation. *Journal of Materials Science* **2012,** *47* (5), 2088-2094.
30. Orgéas, L.; Favier, D., Stress-induced martensitic transformation of a NiTi alloy in isothermal shear, tension and compression. *Acta Materialia* **1998,** *46* (15), 5579-5591.
31. Ni, W.; Cheng, Y.-T.; Grummon, D. S., Wear resistant self-healing tribological surfaces by using hard coatings on NiTi shape memory alloys. *Surface and Coatings Technology* **2006,** *201* (3), 1053-1057.
32. Frensemeier, M.; Kaiser, J. S.; Frick, C. P.; Schneider, A. S.; Arzt, E.; Fertig, R. S.; Kroner, E., Temperature-Induced Switchable Adhesion using Nickel–Titanium–Polydimethylsiloxane Hybrid Surfaces. *Advanced Functional Materials* **2015,** *25* (20), 3013-3021.
33. Ebara, M.; Uto, K.; Idota, N.; Hoffman, J. M.; Aoyagi, T., Shape-Memory Surface with Dynamically Tunable Nano-Geometry Activated by Body Heat. *Advanced Materials* **2012,** *24* (2), 273-278.
34. Maurer, J. J.; Hudson, J. L.; Fick, S. E.; Moffat, T. P.; Shaw, G. A., Electrochemical Micromachining of NiTi Shape Memory Alloys with Ultrashort Voltage Pulses. *Electrochemical and Solid-State Letters* **2011,** *15* (2), D8-D10.
35. Yan, L.; Liu, Y., Effect of temperature on the wear behavior of NiTi shape memory alloy. *Journal of Materials Research* **2015,** *30* (02), 186-196.

Chapter 6

Temperature-induced switchable adhesion using nickel-titanium-polydimethylsiloxane hybrid surfaces

Abstract - A switchable dry adhesive based on a nickel-titanium (NiTi) shape memory alloy with an adhesive silicone rubber surface has been developed. Although several studies investigate micropatterned, bioinspired adhesive surfaces, very few focus on reversible adhesion. The system here is based on the indentation- induced two-way shape memory effect in NiTi alloys. NiTi is trained by mechanical deformation through indentation and grinding to elicit a temperature-induced switchable topography with protrusions at high temperature and a flat surface at low temperature. The trained surfaces are coated with either a smooth or a patterned adhesive polydimethylsiloxane (PDMS) layer, resulting in a temperature-induced switchable surface, used for dry adhesion. Adhesion tests show that the temperature-induced topographical change of the NiTi influences the adhesive performance of the hybrid system. For samples with a smooth PDMS layer the transition from flat to structured state reduces adhesion by 56%, and for samples with a micropatterned PDMS layer adhesion is switchable by nearly 100%. Both hybrid systems reveal strong reversibility related to the NiTi martensitic phase transformation, allowing repeated switching between an adhesive and a non-adhesive state. These effects have been discussed in terms of reversible changes in contact area and varying tilt angles of the pillars with respect to the substrate surface.

This chapter was published in *Adv. Funct. Mater. (2015), 25, 3013–3021.*[1]

6.1 Introduction

Many industrial processes require efficient adhesion systems to grip and release fragile objects such as wafers, lenses or glass plates. State-of-the-art solutions such as vacuum-based handling systems are cost-intensive and have limitations in their applicability. An alternative are micropatterned dry adhesive surfaces similar to those found in nature in various organisms. Several studies, inspired by adhesion systems of spiders and geckos, have investigated synthetic micropatterned adhesives.[2-4] These structures allow easy adaptation to a wide variety of surfaces, causing an increase in contact area at negligible elastic strain and, thus, improved adhesion.

One significant barrier for the application of micropatterned surfaces is the lack of switchability. For gecko setae, the fibrillar structures can be detached by a combination of shear- and peel-motion.[5] While it is possible to mimic the design of the gecko structures, the complex detachment mechanism is often impractical or expensive for implementation into industrial processes.[6-8] A system showing switchable adhesion will be of industrial interest as it might be capable of replacing suction systems, allow handling of fragile and sensitive objects, and can even be used in a wide variety of conditions including in vacuum.

Several studies have investigated various approaches to generate switchable adhesion. Vogel and Steen used surface tension force from liquid bridges which could be controlled by a low-voltage pulse, driving an electroosmotic flow to generate switchable adhesion.[9] Due to the use of a liquid film and its capillary forces this system is not applicable in vacuum or for very sensitive and clean products, where residual free adhesion is required.

Other studies have focused on magnetic concepts for switchable dry adhesion.[10] Northen et al. developed a hybrid-material of an adhesive polymer combined with magnetic nickel cantilevers. They used a magnetic field as trigger and were able to change the orientation of the cantilevers by magnetic fields, which induced a change in contact area and, thus, in adhesion.[11] Although the system showed good switchability, the adhesion forces were very small. Paretkar et al. presented a pressure actuated adhesive system, where adhesion can be switched by varying the compressive load.[12] Mechanical overloading caused buckling of the structures and subsequent loss of intimate contact, which resulted in adhesion loss when a threshold compressive load was applied. This system is sensitive to shear movement, which might trigger the buckling and subsequently loss in adhesion. Another switchable adhesive system, based on a change in contact area and crack-trapping, was presented by Nadermann et al.[13] A metastable film-terminated architecture is switched via air pressure between a collapsed and uncollapsed state; the two states lead to different adhesive properties. The change of the surface state was induced by mechanical loading or air pressure, and the associated critical values were unknown. Triggering this system by use of air pressure may restrict its applicability for use in vacuum. Jeong et al. also used mechanical loading or stretching as a trigger to switch adhesion in a wrinkled dry adhesive surface.[14] Other systems showing switchable adhesion are based on shape memory polymers. Due to a specific external stimulus like light or temperature a phase change in the material occurs and leads to a switch of the stiffness, geometry or surface properties.[15-16] A drawback of these systems is their reversibility. Many systems show a characteristic switch of their properties after applying the specific trigger but need another external force to return back to their initial state.[17] Thus, the combination of two stimuli such as mechanical deformation and thermal-induced recovery are frequently used.[16-18] Reddy et al. used a micropatterned shape memory polymer to change adhesion. However, this required shearing of the pillars to change the contact area and consequently the deformation of the polymer was irreversible.

NiTi alloys can be trained to elicit a reversible two-way shape memory effect, where the shape can be spontaneously changed between a high and a low temperature state.[19-20] It was shown that indentation followed by planarization yields a shape memory surface, where the topography of the NiTi surface reversibly changed from flat to bumpy by heating above, or cooling below, the austenite-martensite phase transformation temperatures.[21-24] The fundamental premise is that the localized deformation due to indentation leads to the two-way shape memory effect (TWSME). A more recent study has strongly indicated that the mechanism associated with this is deformation-stabilized martensite.[25] It is assumed that by acting as a nucleation site the deformation-stabilized martensite guides the growth of the thermally induced martensite and, consequently, the shape change during cooling. This effect has been shown to be repeatable over thermal cycling.

The present work combines the NiTi with TWSME as a functional backing layer with an adhesive polydimethylsiloxane (PDMS) top layer to achieve temperature-induced switchable adhesion. The smooth or patterned PDMS layer functions as adhesion mediating contact element. The deformation-induced TWSME is used to control the topography of the surface and, thus, the contact area of the adhesive.

6.2 Experimental

Materials: In this study, a polycrystalline NiTi shape memory alloy (Ti- 50.3 at% Ni (Ti-55.47 wt% Ni)) procured from Memry GmbH (Germany) was used. The alloy had a martensite finishing temperature (M_f) of about 25 °C and an austenite finishing temperature (A_f) of about 76 °C, as measured by differential scanning calorimetry (DSC, Figure 6.1). Thus, the material is expected to be martensite at room temperature, and austenite in the heated state at 76 °C and above. At temperatures in between, both states are stable depending on the thermal history of the material. For sample preparation, ⟨100⟩ silicon wafers were purchased from Crystec GmbH (Germany). The silanization was conducted with Hexadecafluoro-1,1,2,2-tetrahydrooctyltrichlorosilane acquired from AlfaAesar (MA, USA). Polydimethylsiloxane (PDMS, Sylgard 184) was purchased from Dow Corning (MI, USA). The negative photoresist SU8 and the developer mr-600 were procured from MicroChem GmbH (Germany).

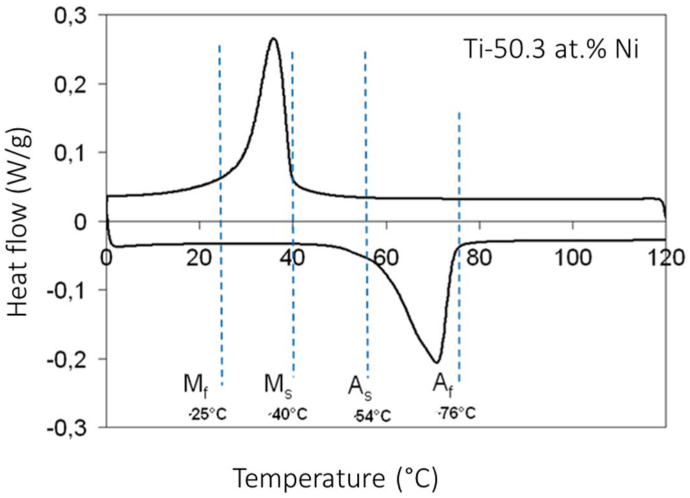

Figure 6.1: Differential scanning calorimetry curves of the NiTi shape memory alloy. The curves show the one-step transformation behavior and the characteristic transformation temperatures of the material. The martensite start and finish temperatures are 40°C and 25°C, and the austenite start and finish temperatures are 54°C and 76°C, respectively.

Sample Preparation: NiTi bulk material of 2 mm thickness was cut into pieces of 10 x 10 mm. The two-way shape memory NiTi surfaces were prepared by indentation with a hardness tester (type V-100-C1, LecoInstrumente, Germany) and a Vickers diamond indenter tip (Ahotec, Germany). A 32 x 65 matrix of indents with interspaces of 400 µm was produced with a load of 10 N. Indentation was performed at ≈-50 °C. After deformation, the samples were replanarized via multistep grinding with SiC paper and mechanical polishing down to 0.25 µm diamond paste. The remaining deformation layer was removed by electropolishing (PoliMat2, Buehler, Germany) with 20 vol% H_2SO_4 and 80 vol% methanol electrolyte solution at 13 V for 60 s. The indented and planarized NiTi samples were covered with a 10 µm - 15 µm thick layer of PDMS by spin-coating (type CT62, Karl Suss, Germany). The base and crosslinker of PDMS were mixed in a ratio of 10:1, degassed in a desiccator, and poured onto the NiTi sample with subsequent spinning at 5000 rpm for 200 s. The PDMS layer was cured for 48 h at 40 °C ($T < A_s$). As reference sample a NiTi- PDMS hybrid system without TWSME was prepared using the same protocol.

The samples with a patterned PDMS layer were prepared in a two-step process (Figure 6.2). i) The NiTi alloy was indented and polished as described above and covered with an about 10 µm PDMS layer via spincoating. ii) A silicon wafer was spin-coated with SU8, heat treated at 65 °C and 95 °C, exposed to UV-light (365 nm) through a lithography mask (ML&C Jena GmbH, Germany) and subsequently developed, resulting in arrays of holes with 50 µm diameter and a depth of 40 µm. The silicon wafer was replicated by mixing PDMS in a 10:1 ratio, degassing, pouring the liquid PDMS onto the silicon mold and curing at 75 °C for 12 h, resulting in PDMS mold (I), which was subsequently silanized. To prevent stiction to the mold and facilitate the demolding process of the hybrid system the silicon mold was silanized by vapor deposition of the silane (hexadecafluoro-1,1,2,2-tetrahydrooctyltrichlorosilane) in a desiccator for 40 min and subsequently heat treated at 95 °C for 45 min.[26] The process was repeated, using PDMS mold (I) as master mold, achieving PDMS mold (II). The PDMS mold (II) was filled with mixed and degassed PDMS, merged with the sample from process step (i) and cured in an oven at 40 °C for 48 h. Finally, the flexible PDMS mold (II) was carefully removed from the sample.

The topography of both samples was measured in the initial state at room temperature, after heating to 80 °C and after cooling again to room temperature using white light interferometry (ZygoNewView 5000, Zygo, USA) and inverse optical microscopy (Olympus PMG3, Olympus Corporation, Japan). The profiles of ten representative protrusions were measured for each sample in the heated state before and after covering the surface with PDMS. The arithmetical mean and standard deviations where calculated for their heights and diameters.

Adhesion Measurements: Adhesion was measured with a custom-built adhesion tester. The positioning stage was equipped with a heating element. A spherical 4 mm diameter glass probe was fixed to the cantilever, measuring deflection by laser interferometry, further details are described in ref.[27] The spring constants of the double beam glass spring were k =284 $\mathrm{Nm^{-1}}$ for the samples with a smooth PDMS layer and k =2475 $\mathrm{Nm^{-1}}$ for the patterned sample. All measurements were performed using a constant displacement velocity of 5 $\mathrm{\mu ms^{-1}}$. Adhesion was measured at least ten times for each temperature. The tests were performed at about 10 mN for the sample with the smooth PDMS layer and about 15 mN for the patterned sample, where pull off force was found to be independent of preload. For temperature cycling, ten measurements were performed on each sample at three positions in the cooled and heated state. An arithmetical mean and standard deviations were calculated from the pull-off forces.

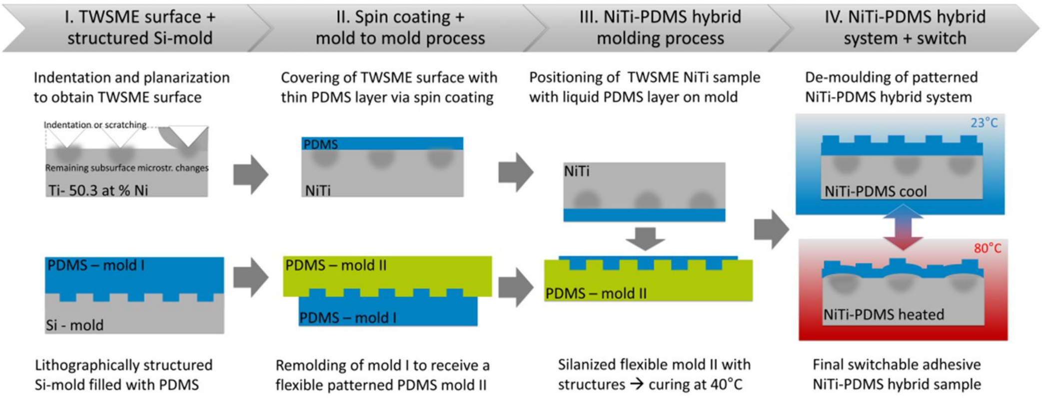

Figure 6.2: Schematic illustration of the fabrication process of the NiTi-PDMS hybrid system. The samples with a smooth PDMS layer on top were fabricated via spin coating. For the sample with a patterned PDMS layer, a multiple step process was applied. A silicon wafer was patterned by photolithography, resulting in cylindrical cavities having a diameter of 50 µm and a depth of 40 µm. A PDMS mold I was cast from the structured silicon wafer and used as template to prepare a flexible PDMS mold II. The latter was applied for the final patterning of the PDMS layer on the hybrid system. Mold II was filled with liquid PDMS, and then a previously indented and polished NiTi sample was brought into contact with the filled mold. All hybrid systems were placed in an oven at 40 °C for 48 h to ensure full curing of the PDMS. The pillar patterned samples were carefully demolded to avoid delamination of the PDMS layer from the NiTi sample.

6.3 Results and discussion

In this study, we used a polycrystalline alloy with a nominal composition of Ti-50.3 at% Ni with an austenite finish temperature of 76 °C and a martensite finish temperature of 25 °C. Thus, the material is expected to be martensitic at room temperature, and austenitic in the heated state at 80 °C and above. At temperatures in between, both states are stable depending on the thermal history of the material. The TWSME was trained using an approach similar to that outlined by Fei et al.[24] and more recently by Qin et al., [25] where semi-hemispherical protrusions are created using indentation. The plastically deformed surfaces were planarized by grinding and polishing. Subsequent heating above the austenite start temperature led to the formation of surface protrusions. Two different hybrid systems were fabricated using the indented and planarized NiTi samples: systems covered with a smooth 10 µm - 15 µm thick layer of PDMS and systems coated with a patterned PDMS layer having hexagonal arrays of pillars with 50 µm diameter and a height of 40 µm. The sample topography was characterized in the cooled (flat) state at room temperature and in the heated (structured) state at 80 °C using an optical and white light interferometric microscope equipped with a heating stage (Figure 6.3).

Figure 6.3a shows an optical image of the sample consisting of a thin layer of PDMS cast directly onto the TWSME NiTi surface in the flat state. Figure 6.3c, e shows the same sample when heated to the structured state. Similarly, Figure 6.3b, d, f) shows the sample with structured PDMS pillars cast onto a duplicate NiTi surface, in both the flat and bumpy states. The smooth sample shows protrusions in the heated state with an average and standard deviation height of 4.0 ±0.3 µm and a center-to-center distance of about 400 µm (Figure 6.3c, e). The protrusions were entirely reversible after cooling. For the sample with the patterned PDMS layer the pillars and the underlying protrusions are clearly visible in the heated state (Figure 6.3d, f). Thus, the topographic change of the NiTi can be observed also on the PDMS layer.

Adhesive Performance and Reversibility: The adhesive properties were measured 15 times at three different positions for multiple temperatures, by load-displacement tests. The sample was brought into contact with a spherical probe, loaded and unloaded again while continuously measuring forces. The maximum load is called preload and the minimum (negative) load is defined as the pull-off force (F_C). Experiments were performed at temperatures ranging from room temperature up to 100 °C in steps of 20 °C, using a constant displacement velocity. Note that the different x -axis scaling in Figure 6.4b is due to differing stiffness of the spring used in the measurement system. The displacement is including cantilever and sample. Figure 6.4 A, B shows the load-displacement curves in the heated and cooled state, with the overall displacement in the system.

For the sample with the smooth PDMS layer, the average pull-off force at room temperature is 1142 ±113 µN, and decreases to 574 ±17 µN after heating to 80 °C. The patterned sample shows an average pull-off force of 711 ±27 µN in the cooled state and nearly no adhesion in the heated state, respectively. Upon unloading multiple detachment events lead to several detachment-peaks, which are typical for structured surfaces if tested with spherical probes.[28-29]

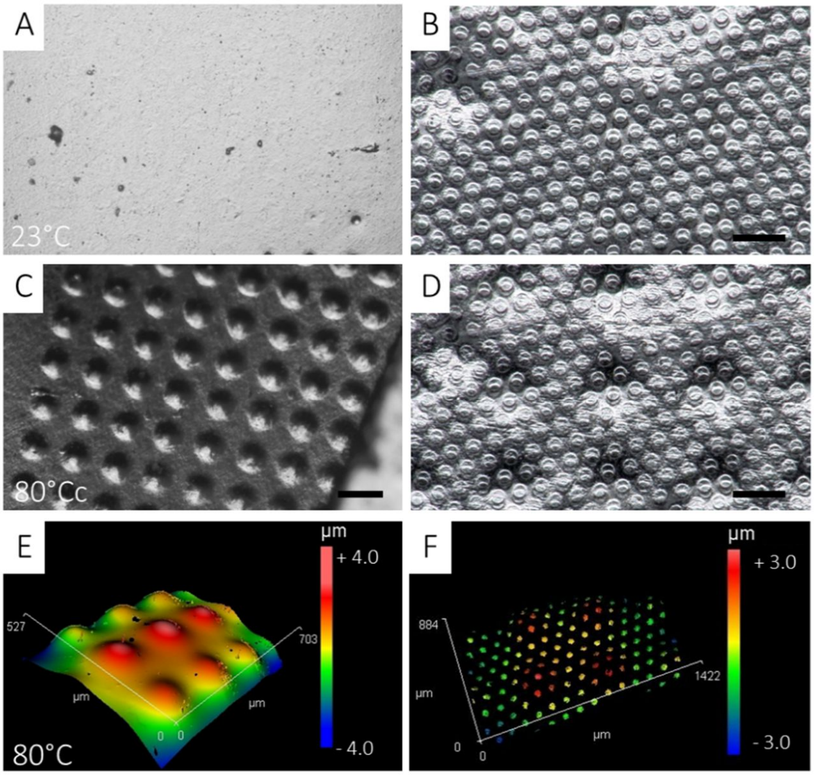

Figure 6.3: Topographic change of the surface for the two NiTi-PDMS hybrid systems with a smooth PDMS layer (left column) and patterned PDMS layer (right column). (A, B) At room temperature (23 °C) both systems are in a flat state. (C, D) In the heated state (80 °C) both systems show a characteristic surface structure induced by the TWSME in the NiTi surface. Pictures are taken via optical microscopy. (E, F) The topography in the heated state, imaged and quantified by white light interferometry. Scale bar 200 µm.

Adhesion measurements were performed for ten temperature cycles to investigate the reversibility of the shown effects. The results in Figure 6.4 C, D indicate no significant loss in adhesion and the switching performance for both hybrid systems. While the patterned sample switches continuously between ‘on’ and ‘off’, the adhesion of the sample with the smooth PDMS layer drops to 54% of the initial pull-off force at room temperature.

The velocity of switching is restricted by heating and cooling, since the transition of the topography switches instantaneous once the transformation temperature is reached. For better comparability a switching efficiency S is defined as

$$\mathrm{S} = 1 - \frac{F_{CB}}{F_{CF}} \tag{6.1}$$

where F_{CF} is the pull-off force in the flat (adhesive, room temperature) state, and F_{CB} is the pull-off force in the bumpy (non-adhesive, heated) state, with $F_{CF} > F_{CB}$ and $0 \leq S \leq 1$. For $S = 0$, there is no change in pull-off force, while $S = 1$ corresponds to an optimal switching action.

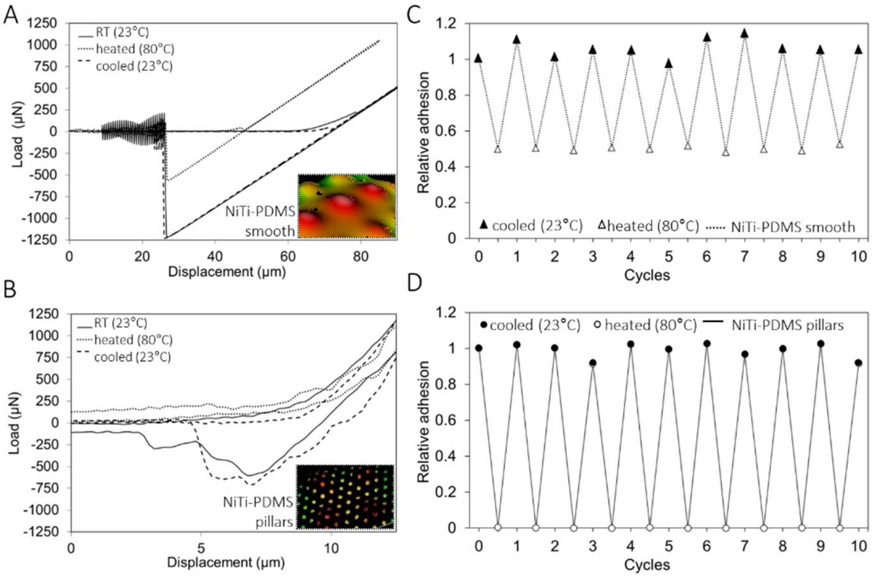

Figure 6.4: Adhesive performance and reversible switching of the two PDMS-hybrid systems. (A, B) Representative load-displacement measurements for each system taken at room temperature, in the heated state at 80 °C and after cooling again to room temperature; the insets represent the topography of the samples in the heated state. (C, D) The repeatability of switching between the adhesive and less/non-adhesive state. Adhesion is measured for 10 cycles from 23 °C to 80 °C. The value for relative adhesion is obtained by dividing the adhesion values by the initial adhesion value prior to thermal cycling.

The normalized pull-off forces (relative adhesion) and the switching efficiency were evaluated for all samples and tested temperatures, and are shown in Figure 6.5.

As can be seen in Figure 6.5a the relative adhesion remains within one standard deviation of 1.00 for all samples up to temperatures of 60 °C. Increasing the temperature to 80 °C leads to a large drop in relative adhesion for both of the TWSME surfaces. This corresponds directly with the formation of protrusions on the NiTi TWSME surfaces at A_f (76 °C), which is just below 80 °C. The drop in relative adhesion remains stable up to 100 °C. The structured hybrid system shows no remaining adhesion force after the topographic change and the smooth hybrid system drops to half of its former adhesive force.

In contrast to these TWSME hybrid systems, the reference system without TWSME, meaning without any switchable topography, shows no significant change in adhesion for all temperatures.

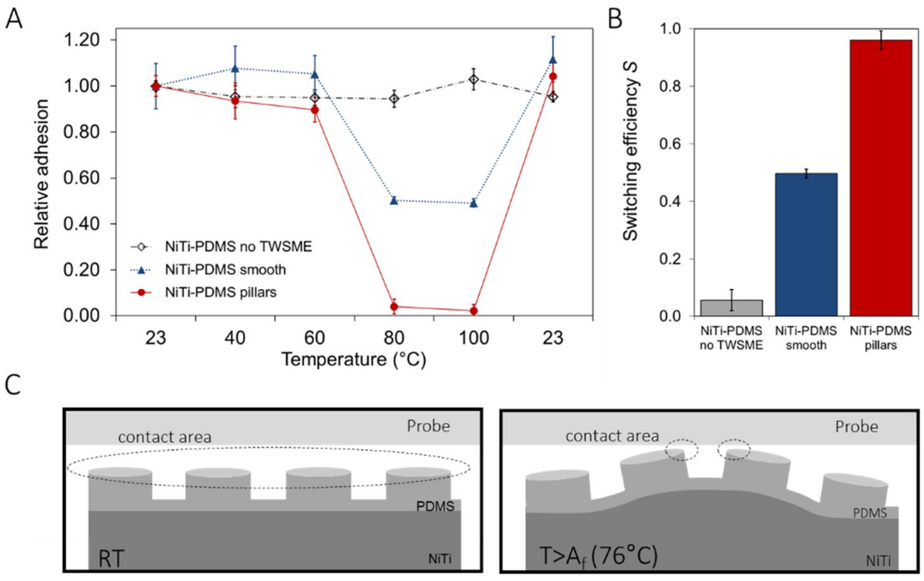

Figure 6.5: (A) Change in adhesion with temperature. The relative adhesion, normalized by the room temperature value, is shown for the tested NiTi-PDMS hybrid systems and compared to the reference sample NiTi-PDMS hybrid without a TWSME. Adhesion is shown at different temperatures relative to the initial adhesion force. The lines are added to guide the eye. (B), The calculated switching efficiency *S* for the three tested systems. (C) Schematic illustration of a patterned sample in the cooled and heated stage during adhesion test with a spherical probe, exemplifying the decrease in contact area. The dimensions of the protrusions are not to scale.

Upon cooling and acclimating to room temperature, the NiTi TWSME surfaces return to ≈1.0 relative adhesion, corresponding to the protrusions returning to a flat surface. Figure 6.5b shows the sample with the smooth PDMS layer has a switching efficiency S of 0.5 ±0.02, while the patterned sample shows the strongest effect with a switching efficiency of 0.95 ±0.05, resembling a near perfect switch within the measurement accuracy. The reference measurement with the NiTi-PDMS sample without TWSME demonstrates a low switching efficiency of 0.06 ±0.03.

Modeling and Finite Element Analysis (FEA): Multiple adhesion theories are available for the contact of elastic spheres.[30] The primary approaches have been proposed by Hertz,[31] Johnson et al. (JKR),[32] Derjauguin et al. (DMT),[33] Maugis,[34] and Bradley.[35] Although these theories often times leads to very similar solutions, the appropriate theory for any particular application can be determined by the evaluation of two parameters. The first, μ, is a ratio of the elastic displacement of the surfaces at the point of pull-off to the effective range of the surface forces. This ratio is given by [30]

$$\mu = \left(\frac{Rw^2}{(E^*)^2 z_0^3}\right)^{\frac{1}{3}} \tag{6.2}$$

where R is the reduced radius of the spheres given by

$$R = \left(\frac{1}{R_1} + \frac{1}{R_2}\right)^{-1} \tag{6.3}$$

E^* is the combined elastic modulus of the spheres given by

$$E^* = \left(\frac{(1 - v_1^2)}{E_1} + \frac{(1 - v_2^2)}{E_2}\right)^{-1} \tag{6.4}$$

w is the work of adhesion (experimentally determined to 39 m Jm^{-2} for PDMS-glass adhesion), and z_0 is the equilibrium separation (taken to be 0.2 nm, which is the van der Waals radius of Si [36]). R_1 and R_2 are the radii of the two spheres and E and v correspond to their Young's modulus and Poisson's ratio, respectively. The effective radius (R) for the flat specimen R_{CF} is 2.00 mm and the effective radius for the bumpy specimen R_{CB} is 0.806 mm, the radius of the bump was computed at the peak. Using geometric parameters given in Table 6.1 and material properties given in Table 6.2, the values of μ for indentation of a flat surface and curved surface are given by 37.6 and 22.0, respectively. According to Johnson and Greenwood,[30] these values place the appropriate adhesion model as either JKR or Hertz, depending on the load. The critical parameter for determining between JKR and Hertz is the ratio $\bar{P}$ of load to pull-off force

$$\bar{P} = \frac{P}{\pi w R} \tag{6.5}$$

For indenting the flat and curved specimens at a load of 1000 µN these ratios are 4.1 and 20.2, respectively. These values place the adhesion studied here well within the JKR region of the adhesion map given by Johnson and Greenwood. [30]

Using JKR theory the pull-off force F is dependent only on the surface energy and the effective radius R

$$F = -\frac{3}{2}\gamma\pi R \tag{6.6}$$

Thus, the JKR predicted switchability is given by

$$S_{JKR} = 1 - \frac{R_{CB}}{R_{CF}} = 0.60 \tag{6.7}$$

This value is slightly higher than the experimentally observed value of 0.50 ±0.02, however, this is to be expected as indenting perfectly on the peak of a bump represents the condition with the least contact area and, consequently, the highest switchability. Thus, Equation (6.7) represents an upper bound on the switchability.

Despite the maturity and convenience of JKR theory to describe adhesion, the applicability of JKR in the case of compliant layers on elastic substrates is a topic of current research. [37-42] The primary feature of JKR is to consider adhesive forces within the contact area, which can be considered as the summation of a Hertz contact area plus an area that arises due to interactive surface forces. The surface forces themselves are not influenced by the bilayer nature of the PDMS-NiTi hybrid, but the Hertz solution will be affected. Consequently, to confirm that the switchability observed between the flat and bumpy morphologies could be described by conventional JKR theory, a finite element (FE) model for the Hertzian contact area was developed in Abaqus (Simulia, Dassault systèmes, 2014). Modeling approaches of this type have been commonly used to assess the effects of a thin layer on adhesion. [39-40] The goal of the FE analysis was to evaluate whether the bilayer morphology combined with underlying surface bumps was well-approximated by a Hertzian contact approximation in the load regime of interest (<1000 µN) such that the use of Johnson–Kendall–Roberts

(JKR) model to predict switchability would be appropriate.[31-32] As such, the finite element model discussed below did not explicitly include adhesive forces, but focused instead on evolution of contact area.

Two primary configurations were modeled: i) glass sphere indenting a flat PDMS-NiTi bilayer and ii) glass sphere indenting a PDMS-NiTi bilayer with a bump. Simulations of these two configurations with a pure PDMS material substituted for the bilayer were also simulated for comparison. All models were axisymmetric with geometric parameters as described in Table 6.1. The bilayer structure was meshed with 62400 4-node reduced integration axisymmetric elements (CAX4R); the indenter was meshed with 65100 CAX4R elements. The bumpy surface was modeled as a sinusoid. Contact between the glass indenter and the PDMS layer was implemented using surface to surface discretization with small sliding. Tangential contact behavior was assumed to be frictionless. Normal contact was defined as hard contact and all contact constraints were enforced directly (in contrast to a penalty method). Nominal linear elastic material properties were used for the three materials and are given in Table 6.2.

Table 6.1: Geometric parameters for the finite element model.

Geometric parameter	(μm)
Indenter radius	2000
PDMS layer thickness	12
Bump height	3
Bump period	400
Model radius	75
Bilayer substrate thickness	47

Table 6.2: Material properties for the finite element model.

	Glass[43]	PDMS[44-45]	NiTi[46]
E (GPa)		2.1	56
v	0.3	0.49	0.3

Linear elastic material properties were selected because the von Mises stresses in the PDMS under the loads of interest did not exceed its yield strength. Loading was applied via displacement control on the top surface of the indenter and loads were computed from the summation of reaction forces on the top surface of the indenter. The bottom boundary of NiTi was fixed. To ensure convergence of the solution with contact nonlinearity, displacement incrementation was controlled such that the maximum displacement increment during any increment was 1 nm.

Contour plots of the maximum absolute principal strains at a load of 1000 μN for the flat specimen geometry are shown in Figure 6.6. The bilayer specimen geometry is shown in a; the same geometry is shown in b, but with a substrate comprised completely of PDMS, shown for comparison as it represents the classic Hertz solution.

The influence of the bilayer interface on the strain field can be clearly observed. In the bilayer material, a, the indent-induced strain is primarily contained in the more compliant PDMS layer such that the bilayer boundary serves to qualitatively change the morphology of the strain from the case of a homogeneous material. This is most evident in the region of the bilayer with a tensile strain component near the outside contact boundary; this is not observed in the homogeneous specimen, b.

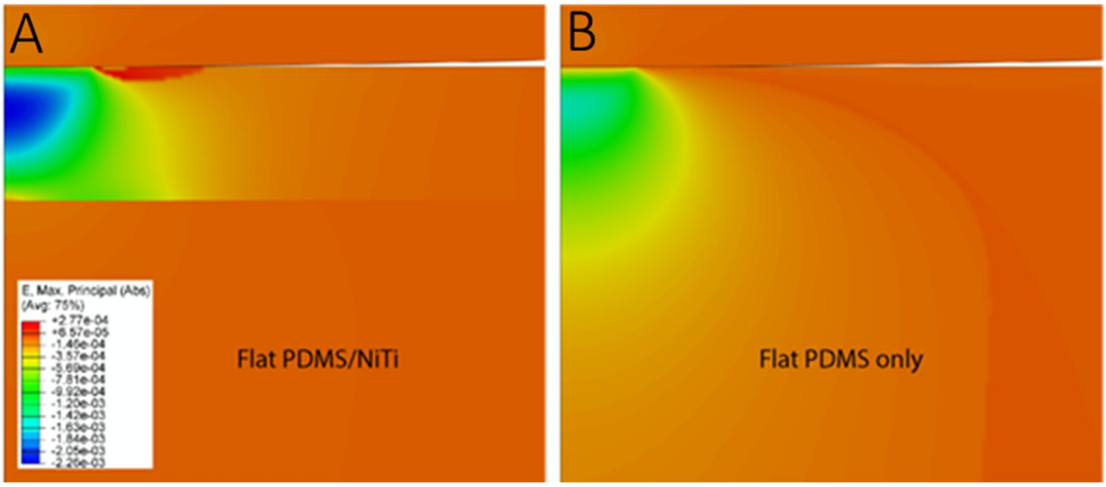

Figure 6.6: Maximum (absolute) principal strain (A) for a bilayer specimen and (B) a PDMS only specimen of the same geometry.

The effect of the differences in strain morphology between the homogeneous PDMS material and the bilayer material on the contact area is not immediately obvious. To directly examine the differences, the contact area for the bilayer was computed via FE analysis as a function of load for both configurations. These data are shown in Figure 6.7 A, where the dashed line is the contact area for the flat geometry and the solid curve is the contact area for the bumpy geometry. As expected, the contact area for the flat specimen is significantly larger than for the bumpy specimen (e.g., nearly a factor of two at the maximum preload). The Hertz contact area, assuming a homogenous PDMS material, was also calculated and is plotted for both configurations. The contact area after Hertz is given by [31]

$$A = \pi a^2 = \pi \sqrt[3]{\left(\frac{3FR}{4E^*}\right)^2} \tag{6.8}$$

where *a* is the radius of the contact area, *F* is the applied load, E^* is the effective modulus and defined in Equation (6.4), and *R* is the effective radius given by Equation (6.3). For the Hertz contact calculation, the PDMS modulus only was used for the substrate and the NiTi was ignored.

From Figure 6.7, the Hertz solution describes the contact area well for both samples, but begins to deviate slightly with increasing load. The agreement between the finite element analysis (FEA) model of the bumpy bilayer sample and the Hertz PDMS-only model is very good.

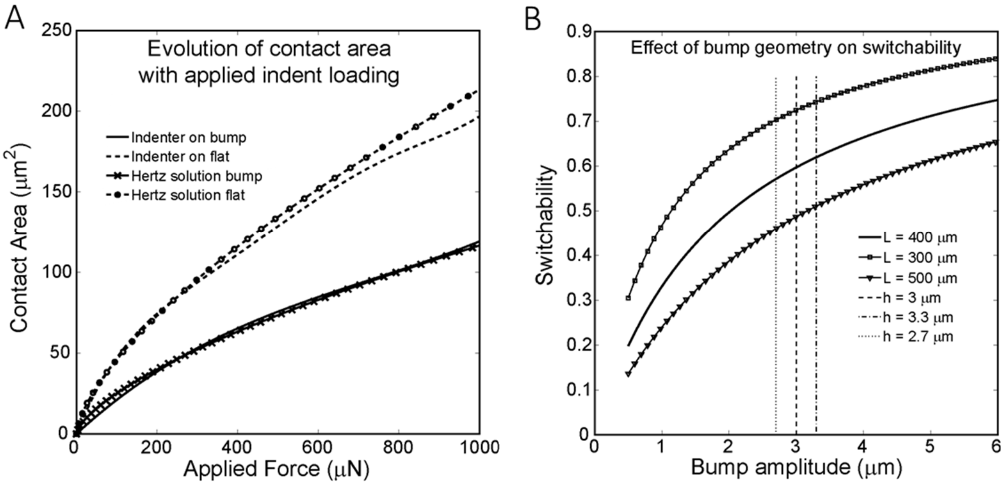

Figure 6.7: (A) Evolution of contact area with applied load in a NiTi PDMS hybrid system. (B) Effect of the bump geometry on the switchability.

This indicates that although the interface does influence the stress and strain fields underneath the indenter, the analytical contact area calculation is still valid over the loads of interest. This was particularly surprising, given the significant differences between the strains under the indenter due to the presence of the NiTi interface. Because of this good agreement with respect to contact area the use of analytical solutions, specifically JKR theory, to describe adhesion and switchability in this bilayer system is warranted.[32]

To examine the sensitivity of switchability to the geometry of the bump, Equation (6.4) was solved for bump amplitudes ranging from less than 1 µm up to 6 µm. In addition, the period L of the bumps was varied from 300 µm to 500 µm. These results are shown in Figure 6.7 B, where the dashed line indicates the value at which the FEA analysis was run (3 µm) and two lines showing ±10% of this value. As can be seen from these data, the experimental values are well within the predicted switchability bounds defined by uncertainties in the geometry. These comparisons are sufficient to conclude that the switchability is entirely due to geometry change and the resultant contact area reduction.

Topographic Change and PDMS Micropattern: The overarching goal of this research was to create a temperature- induced switchable adhesive surface. The premise was to use the recently discovered indentation induced TWSME surfaces to change the contact area between the surface and the probe as a function of temperature. After cooling, the flat surface would have a relatively large contact area with the probe, and after heating the structured surface would make poor contact (e.g., Figure 6.5 C). These NiTi TWSME surfaces are advantageous because the change in surface structure occurs over a narrow temperature range, each state is stable at room temperature, is inherent to the material occurring very quickly (i.e., fraction of a second), and is repeatable over many thermal cycles. Furthermore, although not explored in this work, it would be possible to thermally cycle the NiTi relatively quickly using resistive heating.

Because metallic surfaces exhibit poor dry adhesion via van der Waals forces, our surfaces were coated with PDMS and PDMS pillars in order to facilitate contact adhesion.

The experimental investigation of our switchable adhesive surfaces revealed that the pull-off forces, switching efficiency, and reversibility of all tested samples are not only affected by the change in contact area but also by the topographic change of the

TWSME material and the PDMS micropattern. Both factors are thoroughly discussed below in turn.

The results in Figure 6.5 strongly suggest that the switchability is due to the change in topography, caused by the TWSME of the NiTi alloy. This is supported by the fact that the NiTi-PDMS sample without TWSME shows no sudden switching behavior. Consequently, the temperature range at which the adhesion switch occurs may be adjusted by choosing a shape memory alloy with a different transition temperature. The sudden change in the adhesion at the transition temperature can be explained by the change in contact area between the surface and the probe induced by the TWSME of the NiTi (Figure 6.5 C). The contact area between probe and sample is reduced due to the topographical changes of the NiTi and depends on the protrusion geometry, i.e., the width and the height.

Relative to a smooth PDMS coating, adding 50 µm diameter PDMS pillars on the NiTi TWSME surfaces had a dramatic influence on the adhesive behavior. At low temperatures, where the underlying NiTi is relatively flat, the addition of the pillars decreases the overall pull-off force. This is expected as the presence of the pillars will lead to an overall decrease in the contact area. It is difficult to quantify this value as the precise location of the probe on the surface will strongly influence the number of pillars it comes in contact with. Careful observation of the force-displacement curves in Figure 6.4 B shows discontinuous behavior, indicating that multiple detachment events occur (i.e., pillars separate from the probe at different times). The approximately half-dozen discontinuities are consistent with the likely number of pillars in contact with the probe. Figure 6.5 B also shows almost no measurable adhesion after heating. The reason for this drastic change in switching efficiency is most likely caused by the angle dependent adhesion of the pillar structures; it was shown that adhesion is greatly reduced if the tip of the structure and the probe are misaligned.[28] Even a very small tilt angle of 2°–3° causes a significant decrease in pull-off force. Furthermore, the inclination of the pillars due to the formation of protrusions will provoke bending of the pillars, which also reduces adhesion.[47] In this study the PDMS pillars were specifically designed to be shorter than their diameter. It is expected that long aspect ratio pillars may better conform to a rigid probe, and thereby increase contact area, as has been observed in previous studies.[26] In a subsequent study, this system will be modified using different adhesion enhancing tip geometries such as mushroom shaped tips or higher aspect ratios to further increase adhesion while maintaining the switchability.

6.4 Conclusions

In conclusion, we developed a switchable adhesion system by combining a NiTi two-way shape memory alloy with a bioinspired adhesive PDMS layer. This hybrid material enables to reversibly switch between an adhesive and a low and non-adhesive state. By changing the protrusion geometry of the NiTi shape memory alloy and the pattern of the PDMS layer we were able to alter the switching efficiency, the pull-off forces, and the reversibility of the switch. Such novel smart adhesives can be of interest for many applications such as pick and place processes, for temporary adhesion in biomedical devices, or for climbing robots. Furthermore, systems combining active shape memory alloys and a functional surface may also be adapted to switch other surface properties, e.g. friction, wetting behavior or reflectivity. By use of an additional active material such as liquid crystal elastomers or shape memory polymers further functionality might be provided, triggered by one or two different stimuli, e.g., heat and/or UV-light.[48]

6.5 Acknowledgments

The research leading to these results has received funding from the European Research Council, ERC Advanced Grant “Switch2Stick”, Agreement No. 340929, awarded to E. Arzt. C.P.F. gratefully acknowledges the support of this work from the National Science Foundation (NSF) CAREER award (Grant No. DMR-1255603) as well as the University of Wyoming International Travel Grant.

6.6 References

1. Frensemeier, M.; Kaiser, J. S.; Frick, C. P.; Schneider, A. S.; Arzt, E.; Fertig, R. S.; Kroner, E., Temperature-Induced Switchable Adhesion using Nickel–Titanium–Polydimethylsiloxane Hybrid Surfaces. *Advanced Functional Materials* **2015,** *25* (20), 3013-3021.
2. del Campo, A.; Arzt, E., Fabrication approaches for generating complex micro-and nanopatterns on polymeric surfaces. *Chemical Reviews* **2008,** *108* (3), 911-945.
3. Sameoto, D.; Menon, C., Recent advances in the fabrication and adhesion testing of biomimetic dry adhesives. *Smart Materials and Structures* **2010,** *19* (10), 103001.
4. Boesel, L. F.; Greiner, C.; Arzt, E.; del Campo, A., Gecko-Inspired Surfaces: A Path to Strong and Reversible Dry Adhesives. *Advanced Materials* **2010,** *22* (19), 2125-2137.
5. Autumn, K.; Dittmore, A.; Santos, D.; Spenko, M.; Cutkosky, M., Frictional adhesion: a new angle on gecko attachment. *Journal of Experimental Biology* **2006,** *209* (18), 3569-3579.
6. Murphy, M. P.; Aksak, B.; Sitti, M., Adhesion and anisotropic friction enhancements of angled heterogeneous micro-fiber arrays with spherical and spatula tips. *Journal of Adhesion Science and Technology* **2007,** *21* (12-13), 1281-1296.
7. Murphy, M. P.; Aksak, B.; Sitti, M., Gecko-Inspired Directional and Controllable Adhesion. *Small* **2009,** *5* (2), 170-175.
8. Kamperman, M.; Kroner, E.; del Campo, A.; McMeeking, R. M.; Arzt, E., Functional adhesive surfaces with "gecko" effect: the concept of contact splitting. *Advanced Engineering Materials* **2010,** *12* (5), 335-348.
9. Vogel, M. J.; Steen, P. H., Capillarity-based switchable adhesion. *Proceedings of the National Academy of Sciences* **2010,** *107* (8), 3377-3381.
10. Gillies, A. G.; Kwak, J.; Fearing, R. S., Controllable particle adhesion with a magnetically actuated synthetic gecko adhesive. *Advanced Functional Materials* **2013,** *23* (26), 3256-3261.
11. Northen, M. T.; Greiner, C.; Arzt, E.; Turner, K. L., A Gecko-Inspired Reversible Adhesive. *Advanced Materials* **2008,** *20* (20), 3905-3909.
12. Paretkar, D.; Kamperman, M.; Schneider, A. S.; Martina, D.; Creton, C.; Arzt, E., Bioinspired pressure actuated adhesive system. *Materials Science and Engineering: C* **2011,** *31* (6), 1152-1159.
13. Nadermann, N.; Ning, J.; Jagota, A.; Hui, C. Y., Active Switching of Adhesion in a Film-Terminated Fibrillar Structure. *Langmuir* **2010,** *26* (19), 15464-15471.
14. Jeong, H. E.; Kwak, M. K.; Suh, K. Y., Stretchable, Adhesion-Tunable Dry Adhesive by Surface Wrinkling. *Langmuir* **2010,** *26* (4), 2223-2226.
15. Krahn, J.; Sameoto, D.; Menon, C., Controllable biomimetic adhesion using embedded phase change material. *Smart Materials and Structures* **2011,** *20* (1), 015014.
16. Kim, S.; Sitti, M.; Xie, T.; Xiao, X., Reversible dry micro-fibrillar adhesives with thermally controllable adhesion. *Soft Matter* **2009,** *5* (19), 3689-3693.
17. Eisenhaure, J. D.; Xie, T.; Varghese, S.; Kim, S., Microstructured Shape Memory Polymer Surfaces with Reversible Dry Adhesion. *ACS applied materials & interfaces* **2013,** *5* (16), 7714-7717.
18. Reddy, S.; Arzt, E.; del Campo, A., Bioinspired Surfaces with Switchable Adhesion. *Advanced Materials* **2007,** *19* (22), 3833-3837.
19. Nagasawa, A.; Enami, K.; Ishino, Y.; Abe, Y.; Nenno, S., Reversible shape memory effect. *Scripta Metallurgica* **1974,** *8* (9), 1055-1060.

20. Otsuka, K.; Kakeshita, T., Science and technology of shape-memory alloys: new developments. *MRS Bulletin* **2002,** *27* (02), 91-100.
21. Ni, W.; Cheng, Y.-T.; Grummon, D. S., Microscopic shape memory and superelastic effects under complex loading conditions. *Surface and Coatings Technology* **2004,** *177*, 512-517.
22. Zhang, Y.; Cheng, Y. T.; Grummon, D. S., Shape memory surfaces. *Applied Physics Letters* **2006,** *89*, 041912.
23. Zhang, Y.; Cheng, Y.-T.; Grummon, D. S., Two-way indent depth recovery in a NiTi shape memory alloy. *Applied Physics Letters* **2006,** *88* (13), 131904-131904-3.
24. Fei, X. L.; Zhang, Y. J.; Grummon, D. S.; Cheng, Y. T., Indentation-induced two-way shape memory surfaces. *Journal of Materials Research* **2009,** *24* (3), 823-830.
25. Qin, E.; Peter, N. J.; Frensemeier, M.; Frick, C. P.; Arzt, E.; Schneider, A. S., Vickers Indentation Induced One-Way and Two-Way Shape Memory Effect in Austenitic NiTi. *Advanced Engineering Materials* **2014,** *16* (1), 72-79.
26. Greiner, C.; del Campo, A.; Arzt, E., Adhesion of Bioinspired Micropatterned Surfaces: Effects of Pillar Radius, Aspect Ratio, and Preload. *Langmuir* **2007,** *23* (7), 3495-3502.
27. Kroner, E.; Blau, J.; Arzt, E., Note: An adhesion measurement setup for bioinspired fibrillar surfaces using flat probes. *Review of Scientific Instruments* **2012,** *83* (1), -.
28. Kroner, E.; Arzt, E., Single macropillars as model systems for tilt angle dependent adhesion measurements. *International Journal of Adhesion and Adhesives* **2012,** *36*, 32-38.
29. Guidoni, G.; Schillo, D.; Hangen, U.; Castellanos, G.; Arzt, E.; McMeeking, R.; Bennewitz, R., Discrete contact mechanics of a fibrillar surface with backing layer interactions. *Journal of the Mechanics and Physics of Solids* **2010,** *58* (10), 1571-1581.
30. Johnson, K.; Greenwood, J., An adhesion map for the contact of elastic spheres. *Journal of colloid and interface science* **1997,** *192* (2), 326-333.
31. Hertz, H., On the contact of elastic solids. *Journal für die reine angewandte Mathematik* **1881,** *92* (156-171), 110.
32. Johnson, K.; Kendall, K.; Roberts, A., Surface energy and the contact of elastic solids. *Proceedings of the royal society of London. A. mathematical and physical sciences* **1971,** *324* (1558), 301-313.
33. Derjaguin, B. V.; Muller, V. M.; Toporov, Y. P., Effect of contact deformations on the adhesion of particles. *Journal of colloid and interface science* **1975,** *53* (2), 314-326.
34. Maugis, D., Adhesion of spheres: the JKR-DMT transition using a Dugdale model. *Journal of colloid and interface science* **1992,** *150* (1), 243-269.
35. Bradley, R. S., LXXIX. The cohesive force between solid surfaces and the surface energy of solids. *The London, Edinburgh, and Dublin Philosophical Magazine and Journal of Science* **1932,** *13* (86), 853-862.
36. Bondi, A., van der Waals volumes and radii. *The Journal of physical chemistry* **1964,** *68* (3), 441-451.
37. Sridhar, I.; Johnson, K.; Fleck, N., Adhesion mechanics of the surface force apparatus. *Journal of Physics D: Applied Physics* **1997,** *30* (12), 1710.
38. Johnson, K.; Sridhar, I., Adhesion between a spherical indenter and an elastic solid with a compliant elastic coating. *Journal of Physics D: Applied Physics* **2001,** *34* (5), 683.
39. Sridhar, I.; Zheng, Z.; Johnson, K., A detailed analysis of adhesion mechanics between a compliant elastic coating and a spherical probe. *Journal of Physics D: Applied Physics* **2004,** *37* (20), 2886.

40. Sburlati, R., Adhesive elastic contact between a symmetric indenter and an elastic film. *International Journal of Solids and Structures* **2009,** *46* (5), 975-988.
41. Reedy, E., Thin-coating contact mechanics with adhesion. *Journal of Materials Research* **2006,** *21* (10), 2660-2668.
42. Barthel, E.; Perriot, A., Adhesive contact to a coated elastic substrate. *Journal of Physics D: Applied Physics* **2007,** *40* (4), 1059.
43. Oliver, W. C.; Pharr, G. M., An improved technique for determining hardness and elastic modulus using load and displacement sensing indentation experiments. *Journal of Materials Research* **1992,** *7* (06), 1564-1583.
44. Carrillo, F.; Gupta, S.; Balooch, M.; Marshall, S. J.; Marshall, G. W.; Pruitt, L.; Puttlitz, C. M., Nanoindentation of polydimethylsiloxane elastomers: Effect of crosslinking, work of adhesion, and fluid environment on elastic modulus. *Journal of Materials Research* **2005,** *20* (10), 2820-2830.
45. Castellanos, G.; Arzt, E.; Kamperman, M., Effect of viscoelasticity on adhesion of bioinspired micropatterned epoxy surfaces. *Langmuir* **2011,** *27* (12), 7752-7759.
46. Liu, Y.; Xiang, H., Apparent modulus of elasticity of near-equiatomic NiTi. *Journal of Alloys and Compounds* **1998,** *270* (1), 154-159.
47. Paretkar, D.; Kamperman, M.; Martina, D.; Zhao, J.; Creton, C.; Lindner, A.; Jagota, A.; McMeeking, R.; Arzt, E., Preload-responsive adhesion: effects of aspect ratio, tip shape and alignment. *Journal of The Royal Society Interface* **2013,** *10* (83), 20130171.
48. Liu, D.; Broer, D. J., Self-assembled Dynamic 3D Fingerprints in Liquid-Crystal Coatings Towards Controllable Friction and Adhesion. *Angewandte Chemie International Edition* **2014,** *53* (18), 4542-4546.

Chapter 7

Switchable metallic microtopographies for biomedical applications

Abstract - The chemistry and topography of an implant surface are known to have a strong influence on the cell response in biomedical applications. During the healing process, an implant surface encounters a highly active microenvironment. Processes such as cell-adhesion, proliferation and differentiation depend in a complex succession on the implant surface, and their control is a key issue in tissue engineering. Therefore, we developed a potential implant material with a surface topography that can be switched between flat und structured using temperature as an external stimulus. By using a quaternary nickel-titanium based alloy it was possible to adjust the transformation temperatures. A key aspect is that not only the temperature range of the topography switch lies within a biologically acceptable range, but also both surface geometries can be stabilized at body temperature (~ 37°C), depending on the thermal history of the material.

Due to the addition of copper and chromium, the transformation temperatures were suppressed, but the alloy suffered from copper ion leakage when incubated in cell cultivation media. Therefore, the surface shows low biocompatibility without passivation. Electrochemical oxidation was used to pacify the surface, thereby reducing the ion leakage and increasing biocompatibility while retaining the desired dynamic topography. A switchable surface topography could be used in a metallic implant material to provide control of surface morphology to activate cell alignment or cell proliferation.

7.1 Introduction

A key issue in cell cultivation and tissue engineering is the guidance of cell growth, their attachment, alignment and migration on an implant surface. The use of a metallic shape memory surface as implant material may offer the possibility to alter the topography and roughness by a certain external stimulation, e.g. induction heating.

As described by Duerig et al., nickel-titanium (NiTi) shape memory alloys have become a ‘household’ material in the medical engineering world and attention has turned particularly towards implants.[1] For example, NiTi alloys are specifically used as orthodontic arch wires and vascular stents.[1-3] In the stable physiological temperature conditions, its superelastic behavior was mostly used instead of the more complex shape memory effect.[4] Besides pseudoelasticity, subtle aspects such as biocompatibility, thermal deployment and hysteresis make NiTi a promising material for biomedical applications. However, Simon et al. presented one approach using the one-way shape memory effect.[5] They inserted a straight, thin wire for treatment of pulmonary embolism. Upon reaching the correct position, the wire self-unfolded to a complex filter shape. Triggered by body heat, the trained shape memory wire, recovered its programmed shape.

Most active implant devices based on the one-way shape memory effect are inserted directly after cooling or with active cooling during insertion into the body. Subsequently, the phase transformation from martensite to austenite, and therefore the shape change, is induced by the body’s heat.

More recently, Pfeifer et al. presented an adaptable orthopedic implant, which can be externally stimulated.[6] Motivated by the demand for implant materials which can be activated externally after a certain time, they used the one-way shape memory effect to adapt the implant stiffness during the healing process. In fracture repair, this supports the healing process without the need of a second surgery. Heating the implant to 60°C through induction activated a shape change of the NiTi alloy and, thus, changed the stiffness of the implant device.

Müller et al. used the one-way shape memory effect in a similar way to stabilize tibia osteotomies in rabbits. They used noninvasive induction heating to increase fixation stiffness, thereby promoting bone healing.[7-8] They revealed that, induction heating of the implant to 40 °C or even 60 °C has neither led to significant inflammatory changes, necrosis nor corrosion pits in a rat model. The advantage of an external activation enables a specific timing of the mechanical stimulus, several weeks after the implantation. For applications in human therapy, the phase transformation temperatures have to be lowered to reduce tissue irritation due to heat.

These studies demonstrate the potential of implant materials with a one-way shape memory effect, to enable a one-time stimulation of the healing process. The introduction of an implant device with the reversible two-way shape memory effect may enhance stimulation of the healing process, due to temporally control of multiple activation cycles. In addition, while the one-way shape memory effect induces mostly macroscopic shape changes of the implant, the implementation of a reversible two-way shape memory effect, permits relatively small reversible actuation. With such a switchable topography the healing process could be accelerated, due to guidance of cell adhesion or the stimulation of bone growth, by actively introducing or releasing stresses. Ingnatius et al. concluded, after cyclic stretching of cell matrices, that mechanical load promoted the proliferation and differentiation of osteoblastic precursor cells.[9]

Various investigations have focused on surface treatments and the cell-surface interaction of NiTi implant materials, not only because Ni is known to cause hypersensitive reactions and tissue necrosis,[10] but also because surface topography and chemistry play a crucial role in the healing process.[11-13] Shabalovskaya et al. summarized recent developments in NiTi surface modifications for biomedical applications. They demonstrate how a Ni- ion release is effectively prevented if the surface integrity is maintained under strain and no Ni-rich sub-layers are present. Mechanical surface treatments such as shot peening, grinding, and groove formation were used to change the surface topography and promote cell adhesion as well as endothelialization.[14] [15] Palmaz et al. determined that grooves of 1, 3, 15 and 22 µm size promoted an increased rate of migration of endothelial cells up to 64.4% compared to a polished smooth surface. Thereby a promising result regarding the endothelialization time for endovascular stent surfaces was shown.[14] More recently, different publications and patents on topographical features of metallic medical devices gave insights into the importance of cell alignment and enhanced endothelialization due to specific microtopographies.[16-18] Although Dalby et al. demonstrated that random nano-and microtopographies influence osteogenic differentiation, other researches showed that cells differentiate between specific pattern and feature sizes.[19-20]

Control of the features plays a crucial role for the development and analysis of implant materials and their cell-interaction. Accordingly, research on active implant materials emerged significantly over the last decade. Active spatial control of cell-growth through switchable nano- and micropatterned topographies opens the opportunity to gain deeper insight into adhesion-mediated cell signaling and adds another dimension to the mechanobiology of cells.[21-23] Currently, stimuli responsive substrates use humidity and temperature to induce a change in the materials chemical configuration, leading to a change in topography or a change in the molecular configuration of the interface.[24] Until now, most studies have investigated switchable topographies on single material polymers and were restricted to periodic patterns. Investigations on metallic surfaces with different switchable topographies using Ti or NiTi based alloys, which are frequently used as implant materials, are still missing.[12, 25-26]

A switchable topography can be elicit by trained NiTi surfaces.[27] It was shown that textures formed by indentation, cold embossing and electrochemical machining followed by planarization yield a shape memory surface. The topography changed reversibly from flat to bumpy by heating above, and cooling below, the austenite-martensite phase transformation temperatures.[27-30] The two-way shape memory effect (TWSME) is thought to be related to the localized stress due to indentation and subsequent planarization. Current understanding of the TWSME mechanism treats the deformation-stabilized martensite as a nucleation site that guides the growth of the thermally induced martensite. During cooling, the growth of the preferred martensitic variants leads to a shape change, which is shown to be repeatable over thermal cycling.

The work in this chapter is using the deformation induced TWSME to achieve a temperature-induced switchable topography on a metallic implant material.

The transformation temperatures of commonly used NiTi shape memory alloys exceed the temperature tolerances of living cells by far. Therefore, a novel shape memory alloy was developed, which meets the requirements for contact with cells, namely a small hysteresis width and martensite-austenite phase transformation temperatures near body temperature i.e. 37°C. If switchable topographies can be induced through embossing in a NiTiCuCr alloy will be investigated in the present work. Furthermore, the activation of a switchable topography near body temperature and its biocompatibility will be explored by cytotoxicity tests and by screening the ion release rates.

7.2 Material and methods

A polycrystalline NiTiCuCr shape memory alloy was developed in collaboration with Ingpuls GmbH (Germany). The alloy with a composition of $Ni_{42.5}Ti_{49.65}Cu_{7.5}Cr_{0.35}$ at% was annealed at 800°C, above the recrystallization temperature, for 30 min and the 2 mm thick sheets were cut into pieces of 10 mm^2 using a wire-cutting saw.

Three samples were prepared for thermal analysis by differential scanning calorimetry (DSC) using a Mettler Toledo DSC1 Star System and a temperature range from -80 to +80 °C. Each sample was measured over three cycles with heating and cooling rate of 10 $Kmin^{-1}$. Characteristic phase transformation temperatures were determined by the tangent method.

The two-way shape memory effect was trained with cold-embossing and subsequent planarization. The samples were ground using 2500 SiC paper, followed by mechanical polishing steps down to 1 µm. The polished samples were cooled to a temperature of -10°C and embossed in the cooled state using a hydraulic press (Paul-Otto-Weber GmbH) with a metallic micro-mesh obtained from Haver & Boecker OHG. The cloth like mesh made from stainless steel wires and was embossed into the surface applying a load of 100 kN for 10s. The textured NiTiCuCr surface was subsequently planarized by compression with an optically smooth hard metal workpiece applying a load of 200 kN. Thereafter oxide suspension polishing (OP-S Suspension, Struers GmbH, Germany) was performed up to an average roughness (R_a) of 0.04 µm.

The temperature-induced change in the surface topography was measured with white-light interferometry (Zygo NewView 5000). The sample was heated and cooled using a Linkam PE120 heating/cooling stage. The surface topography was measured in situ, between 25 °C and 40 °C in 1 °C steps, both for heating and cooling of the sample.

The bulk microstructure and surface chemistry of the NiTiCuCr alloy were analyzed using X-ray diffraction analysis (XRD) and energy dispersive X-ray spectroscopy (EDS). The X-ray diffraction pattern were recorded with $\Theta/2\Theta$ scans using a Bruker AXS D8 X-ray diffractometer to determine the material composition on the polished and the oxide surface.

For cytotoxicity testing, the samples were immersed in ethanol and put in an ultrasonic bath for 5 min, dipped into acetic acid for 6 s, immersed in acetone, ethanol and isopropanol, and rinsed with distilled water in between each step. Afterwards, the samples were stored in phosphate-buffered saline (PBS) for 24 h. Under sterile conditions, they were immersed in 70% ethanol for 20 min, washed with PBS for 5 min and immersed in sterile distilled water for 5 min. Three samples were incubated in cell-culture media (Fibroblast Basal Medium, PCS-201-030, ATCC®) with a fibroblast growth-kit, serum-free (PCS-201-040, ATCC®). After 48h, the cell culture media was renewed. The removed cultivation media was saved for ion analysis. Human primary dermal fibroblast were seeded (neonatal, PCS-201-010, ATCC®) with a density of $5x10^4$ ml^{-1}. As a control, an empty polystyrene well was filled with the cell culture media. The cells were incubated for 48h at 37 °C and 5% CO_2. The samples and the control were washed twice with PBS before they were live-dead stained with 4 µM Calcein AM and 2 µM Ethidium Homodimer and finally incubated for 30 min at room temperature.

Images of the samples were taken using an optical microscope (BX51, Olympus, Japan). The ion concentration of Ni, Ti, Cu and Cr isotopes in the cell culture media was measured using inductively coupled plasma mass spectrometry (ICP-MS, LC 1100 MSD SL, Agilent, USA) after 48 h immersion of a NiTiCuCr sample.

The surface was electrochemically oxidized using acetic acid as electrolyte and a voltage of 10 V with a current of 15 mA for 4 h. The oxide layers were characterized with an inVia Raman spectroscope (Renishaw plc, UK), with a Nd:YAG Laser at 532 nm wavelength. The switchable topography after the oxidation process was characterized analogue to the measurements before the oxidation.

7.3 Results

A quaternary $Ni_{42.5}Ti_{49.65}Cu_{7.5}Cr_{0.35}$ alloy system was developed in collaboration with Ingpuls GmbH with the requirements to have a small hysteresis width, with a martensite finish temperature (M_f) and an austenite finish temperature (A_f) as close as possible to 37 °C and used in the following experiments.

7.3.1 Phase transformation temperatures

The phase transformations of the quaternary alloy system are shown in DSC measurements in Figure 7.1. One single peak was measured during either heating or cooling, strongly indicating a one-step transformation from austenite to martensite and vice versa. One peak appears slightly above body temperature of 37 °C and the other one slightly below 37 °C. The specific phase transformation temperatures are listed accordingly. The transformation to austenite starts at 30.7 °C and finishes at 51.3 °C., while for the martensite transformation a start temperature of 29.7 °C and a finish temperature of 5.8 °C are shown. A thermal hysteresis, which is typical for martensitic phase transformation, is still present, but reduced to a minimum, as required for the intended application in biomedicine. In addition, the sample is still in a transition state right at the application temperature of 37 °C at which austenite transformation is not finished for samples heated from room temperature.

7.3.2 Switchable topographies activated near body temperature

White light interferometry measurements visualize a switchable temperature-induced surface topography (Figure 7.2). The topography changes from flat to textured after heating the sample to 40°C and vice versa upon cooling the sample to room temperature. The average roughness (R_a) changes from 0.05 µm with peak to valley roughness (R_z) of 0.26 µm at 20°C to a R_a of 0.17 µm and an R_z of 1.72 µm at 40 °C. Over five heating and cooling cycles the topography exhibits a stable recovery behavior.

Analysis of the change in topography during heating or cooling revealed two different states at 37 °C. Coming from room temperature, the sample remains nearly flat at 37 °C, while coming from the heated state with 42 °C, a mesh-like pattern appears at 37 °C.

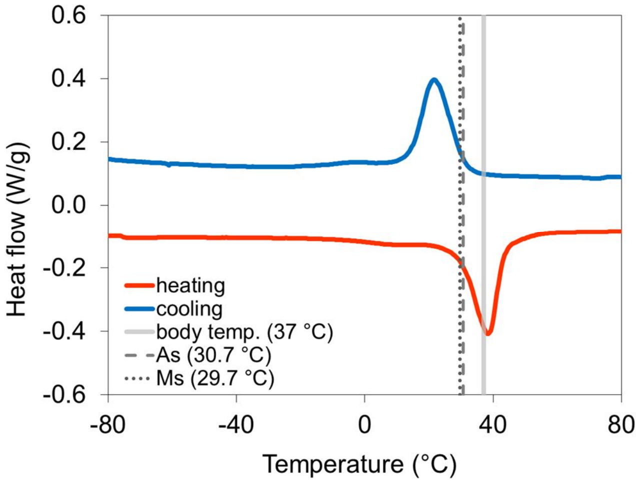

Phase transformation	Temperature C°
M_f	5.8
M_s	29.7
A_s	30.7
A_f	51.3

Figure 7.1: DSC measurement of heating and cooling the NiTiCuCr shape memory alloy. A phase transformation near body temperature with a small hysteresis width is shown.

Subsequently, both topographies can be stabilized at body temperature, depending on the thermal history of the sample. Coming from the cooled state, the surface shows a R_a is 0.08 µm with an R_z of 0.91 µm at 37 °C. Coming from the heated state, R_a increased to 0.15 µm with an R_z of 1.93 µm.

The results show that switchable topographies can be induced in the quaternary NiTiCuCr system and manifest reversible switchability near body temperature. Furthermore, the topography at the usual incubation temperature of 37 °C can be adjusted by pre-heating or cooling the sample.

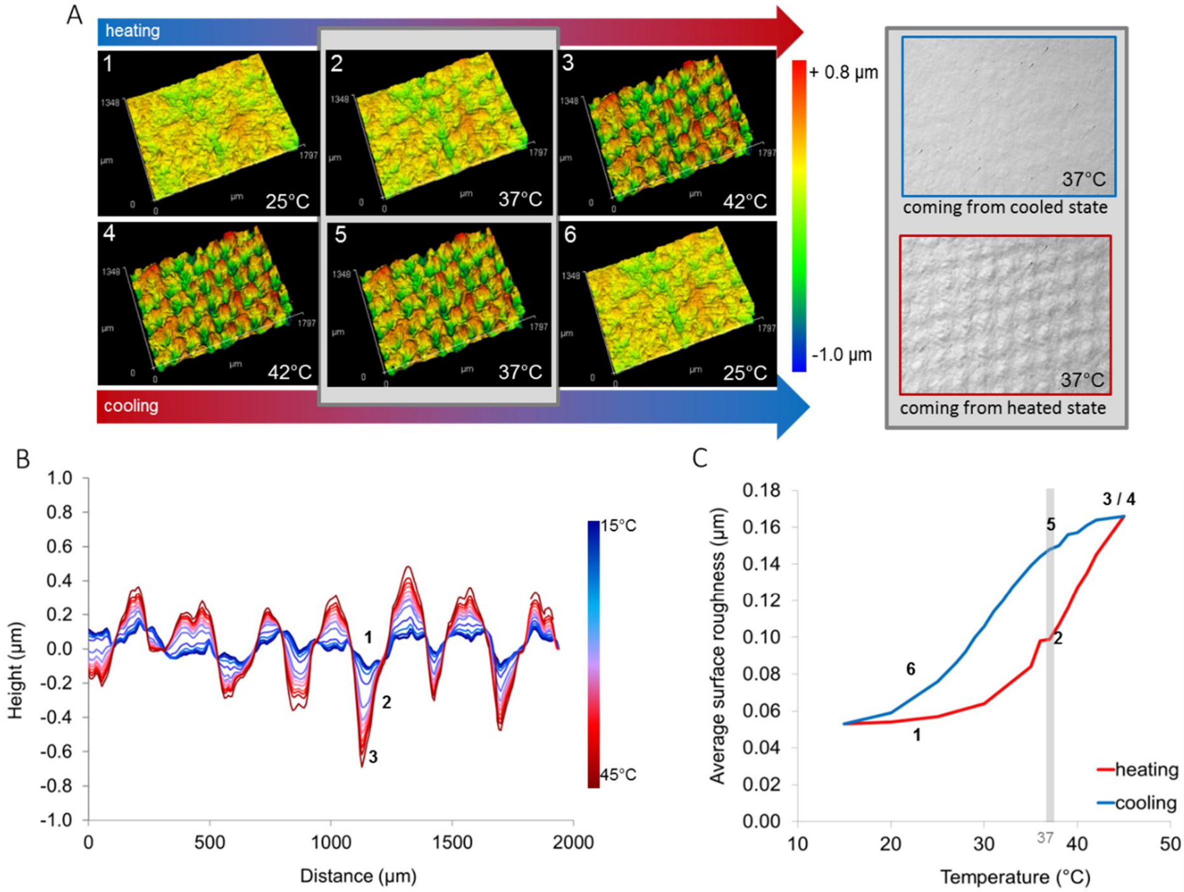

Figure 7.2: Switchable topography in NiTiCuCr activated near body temperature. (A) White light interferometry images of the change in topography during heating from 25 °C to 42 °C and cooling back to 25 °C. The material shows a flat or a textured topography at 37 °C depending on its thermal history. (B) Profile of the topography depending on the temperature. (C) The reversible change in roughness shows a hysteresis during the heating and cooling cycles.

7.3.3 Ion release and celltoxicity

The ICP-MS results are shown in Figure 7.3. The concentration of dissolved metal ions in the cell-cultivation media well exceeded parts per million concentrations for all isotopes. In particular, the highest ion concentration was measured for Cu-isotopes. The concentration was exceeding the measurement standards by far. Due to a non-linear calibration curve, no absolute values on the Cu ions can be given.

Considering the toxicity of heavy metal ions for cells and bacteria,[31-33] the high concentration of copper-ions and the additional presence of chromium- and nickel-ions increase the potential for cytotoxicity of the polished NiTiCuCr surface.

The actual cytotoxicity of the NiTiCuCr surface was tested with fibroblast cells after 48h of cultivation via life-dead staining. Figure 7.4 shows optical micrographs of the fibroblast cells on the NiTiCuCr surface, only few cells are present.

The NiTiCuCr samples show very low cell activity and viability compared to the polystyrene control surfaces. While the fibroblasts on the polystyrene control are viable and extending in an elongated shape, the fibroblasts on the NiTiCuCr surfaces are balled up to a spherical shape, to minimize their contact area with the substrate. In comparison, the control shows viable extended fibroblasts in elongated shape on the polystyrene substrate.

With both, the ion concentrations from ICP-MS and the life-dead staining, the polished NiTiCuCr surface indicates a possible toxic effect of the surface or the media. If no stable oxide layer has formed on the metal surface, the ion release by diffusion into the cell-cultivation media is an unsaturated process. A stable oxide layer could be used as an ion diffusion barrier layer, to prevent the cells from toxic ion-concentrations.

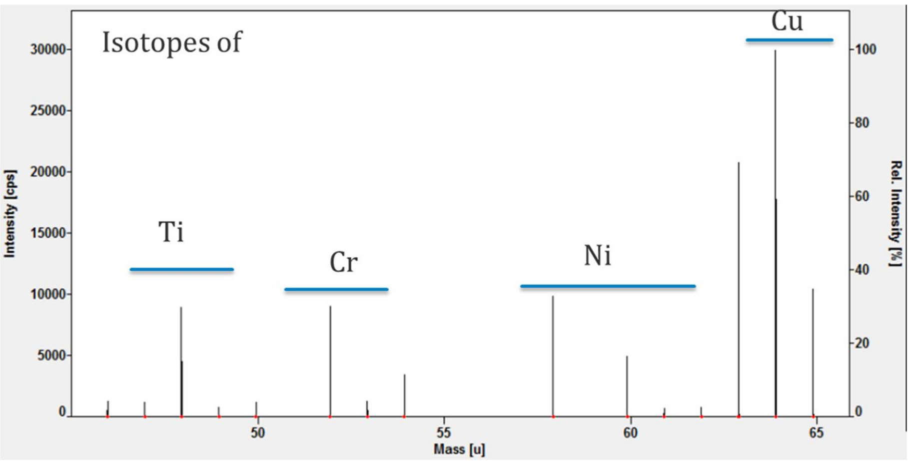

Figure 7.3: Ion concentration measured by inductively coupled plasma mass spectrometry. All isotopes show a concentration in the parts per million range.

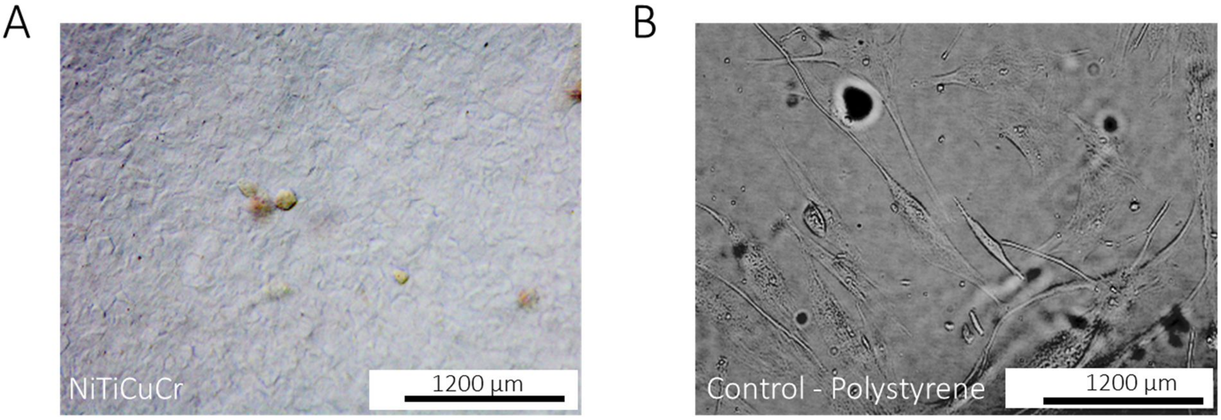

Figure 7.4: Optical microscopy images of fibroblast seeded on NiTiCuCr and the control surface after 48h in cultivation media. (A) The inspection of the surface reveals few cells, which are balled up to minimize contact with the NiTiCuCr. (B) Inspection of the control reveals more cells with extended morphologies.

7.3.4 Ion barrier layer

In order to gain such a passivated surface, electrochemical oxidation was applied on the NiTiCuCr surface. Figure 7.5 A shows an optical micrograph of an electrochemically oxidized NiTiCuCr surface.

A clearly visible oxide layer has formed in the circular spot exposed to the electrolyte. The metallic appearance changed to dark blue with iridescent colors at the edge of the oxidized area. Images taken by scanning electron microscopy show a dense oxide layer without visible cracks (Figure 7.5, B). Moreover, as demonstrated in Figure 7.5 C, the switchability of the topography induced by the TWSME is preserved after the electrochemical oxidation. The topography was reversibly changed by heating and cooling of the sample between 30°C and 40°C. Oxidation by electrolysis led to the growth of an oxide layer on the NiTiCuCr samples. The composition of the oxide was analyzed using EDS and Raman spectroscopy. The atomic composition found with EDS is tabulated in Table 7.1. The sample that underwent electrochemical oxidation has a peak at 0.525 keV, indicating the presence of an increasing amount of oxygen after the electrochemical treatment normalized to the titanium peak.

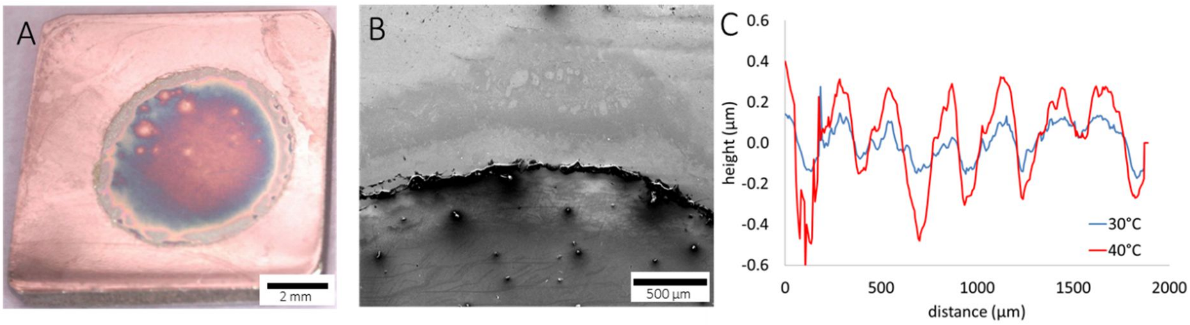

Figure 7.5: Oxide formation on the NiTiCuCr surface. (A) An oxide layer was formed by electrochemical oxidation in the sample centre. (B) SEM micrograph of the dense oxide layer on the surface. (C) Profile of the topography in the cooled and heated state. The surface showed a temperature-induced switchable roughness.

The analysis of the Raman spectra in Figure 7.6 reveals peaks at 265, 473, and 600 cm-1. According to Firstov et al. and Gu et al., the spectra of rutile contains peaks at 240, 447 and 612 $cm^{-1}$and the spectra of anatase TiO_2 shows peaks at 143, 196, 396, 516 and 637 cm^{-1}.[34-35] The peaks appear less distinct due to the poor christalinity of the oxide layer. The broad shift between 550 and 740 cm^{-1} is thought to arise from defects in the rutile structure.

Table 7.1: Data of the composition of the polished and electrochemical treated sample measured by EDS.

	wt.%		at. %	
Element	Sample pol.	Sample ox.	Sample pol.	Sample ox.
Ni	44.88	42.03	42.73	39.92
Ti	45.76	38.91	49.43	33.95
Cu	9.08	8.32	7.59	5.47
Cr	0.27	0.27	0.25	0.22
O	-	6.90	-	18.03

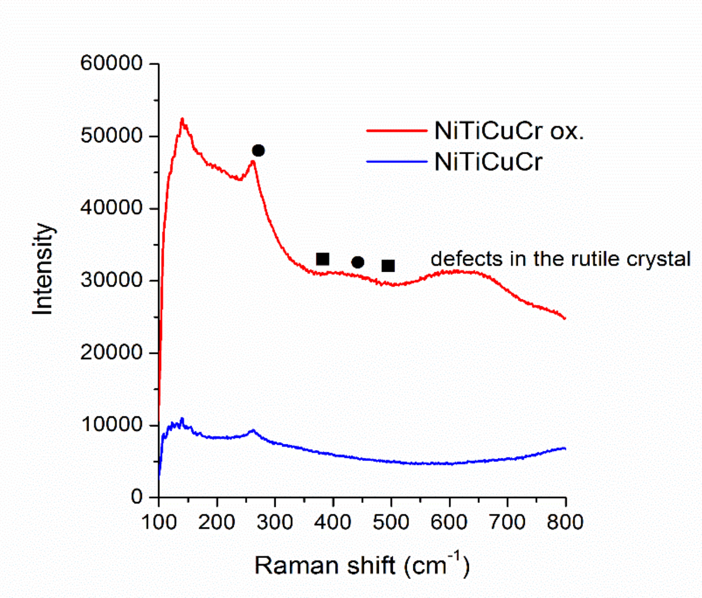

Figure 7.6: The Raman spectra of a polished sample (blue) and an electrochemically grown oxide layer on a sample (red). The oxide spectra indicates the presence of rutile (circles) and anatase (squares) phase of TiO_2.

7.4 Discussion

Phase transformation behavior: The DSC measurements of commercially available $Ti_{45.1}Ni_{49.6}Cu_{4.97}Cr_{0.29}$ wires (Ormco Corp., USA) show similar phase transformation behavior.[36] The measurements published by Iijima et al. show a one-step transformation and an increase in phase transformation temperature for the quaternary alloy compared to binary NiTi or ternary NiTiCu alloys.[36]

The substitution of Ni by Cu ions increases the crystallographic compatibility at the martensite-austenite interface, leading to smaller transformation hysteresis. With a more compatible phase interface, the fatigue resistance is enhanced and the functional stability is increased for cycling applications.[37-39] In addition, the phase transformation temperature increases with increasing amount of Cu. Additions of Cr as a quaternary alloying element helped to suppress the phase transformation to lower temperatures, while capitalizing the benefits of the presence of Cu. Jaeger et al. focused on the hysteresis and phase transformation temperatures in quaternary alloys.[40] They reported the addition of Cr lowered the phase transformation temperatures more than other elements such as V, Fe, or Co.[41]

The M_s and A_s temperatures being nearly identical in specific NiTiCuCr alloys is also shown by investigations of Wang et al. After annealing a $Ni_{45.1}Ti_{49.6}Cu_{4.97}Cr_{0.29}$ alloy at 800 °C, M_s and A_s were measured at nearly the same temperature, differing only about 1°C. The increase of M_s and A_s to 29.7 °C and 30.7 °C respectively, can be explained by the increased amount of Cu in the alloy composition used in the present study compared to the alloy used by Wang et al.[42]

Two-way shape memory topographies: To our knowledge, no research was conducted on the TWSME in quaternary shape memory alloys, with a phase transformation near body temperature. Most studies, using a commercially available quaternary shape memory alloy of NiTiCuCr, are focused on superelastic properties at body temperature for use in orthodontic wires.[36] They investigate the pseudoelastic behavior, corrosion resistance and effects of cold rolling on pseudoelasticity.[43-44] The A_f of these alloys is usually below the physiological temperature, leading to a fully austenitic state for applications in the body. The one-way or two-way shape memory effect is rather considered as a side effect.[45-46] Meling and Odegaard addressed concerns that the superelastic properties and stiffness of the wires may change with altering temperature. For example, wires located in the mouth of patients may change their mechanical properties during uptake of hot or cold food or drinks. They showed that ingestion of cold liquids could provide inadequate forces for tooth movement, thereby revealing that the temperature-induced shape memory effect is able to apply forces on its environment.

Here, for the first time, an implant material is presented, that is designed to use the TWSME for a temperature actuated switchable topography at physiologically relevant temperatures for *in vitro* and *in vivo* cell cultivation. The size of the switchable surface features induced with the TWSME can range from hundreds of nanometers to a few microns, depending on the alloy and the training procedure. Cells were shown to interact mostly with structures of the same length scale; however, depending on the cell type and cultivation time, their sensitivity can extend to the nanometer scale. Fibroblasts adapt after 24 h cultivation time to grooves down to a threshold of 35 nm in depth.[19, 47] Overall, feature depth and radius of curvature seem to be the topographic parameters with the strongest influence on cell guidance.[19, 48]

The switchable surface topographies in NiTiCuCr are trained to elicit switchable random roughness, grooves, spherical protrusions or other microscopic elevations on the surface of the implant. Thus, by changing the implant topographies the rate of endothelialization and cell alignment could be controlled. Therefore, in-stent restenosis and thrombosis could be reduced.[14, 49] The principle effects of such a switchable topography were demonstrated by Ebara et al.[50] They changed the alignment of cells using the one-way shape memory effect in a thermo-sensitive shape memory polymer. A groove pattern was altered by heating into a smooth surface or a surface with perpendicular grooves. The cells adapted with cultivation time, even if the material was kept at 32 °C, due to the specific phase transformation temperatures of the shape-memory polymer.

With switchable surface topographies on the NiTiCuCr alloy, a metallic implant material with strong mechanical properties compared to polymer materials, was developed. The two-way shape memory effect allows reversible actuation without any changes in surface chemistry. The set phase transformation temperatures allow an accurate control of the topographies at 37 °C.

Ion leakage and celltoxicity: It is well documented that a high concentration of Cu ions leads to a high mortality rate of cells is evident considering that toxicity of Cu ions for cells.[31-33] Haider et al. investigated the ion release and corrosion resistance in ternary NiTiCu and NiTiCr alloys after immersion in PBS solution.[51] They detected a small release of Cu ions and a large amount of Cr ions into the media, for all tested alloys.[52] Hwang et al. investigated the metal release and corrosion resistance of orthodontic arch wires and brackets of NiTiCu or NiTiCuCr into artificial saliva with a pH value of 7.[53] With regard to literature, threshold values for the lethal concentration of Cu ions were hard to determine. Cao et al. concluded after an elaborated summary on literature dealing with various cell-types and copper concentrations that the thresholds for Cu accumulation vary for the different cell types in the body. Their findings suggest a LD_{50} dose of about 46 $\mu g ml^{-1}$ (~29 μM) Cu ions for L929 mouse fibroblasts and >99 % cell death with 24 h exposure to 100$\mu g ml^{-1}$ (~62 μM). [33]

Other studies observed that in contrast to the cytotoxic effects, a specific concentration of Cu ions could contribute positively to wound healing and atherogenesis.[54-55]. Heidenau et al. demonstrated highly antibacterial properties with a tolerable cytocompatibility, in *in-vitro* tests with direct surface contact, for fourfold Cu-TiO_2 coatings. Furthermore, their patent on structured coatings for implants using powder-filled ceramic coatings in order to enhance surface roughness and promote the active elution of ions, reflects the impact of the surface texture on ion-release and subsequent cell-interaction.[56]

As demonstrated by Heinecke et al., the presence of Cu could also accelerate the pathogenesis of vascular diseases such as arteriosclerosis. They revealed that a micro-molar concentration of Cu-ions promoted a modification of low-density lipoproteins by human arterial smooth muscle cells. [55] Subsequently, a remaining Cu-leakage from the NiTiCuCr surface with micromole concentration could also have positive effects on cell-growth and arterial desease.

Studies on ternary NiTi based shape memory alloys revealed that the addition of passive metals such as Ti, Cr and Ta developed stable oxide layers, which contribute to the corrosion resistance. Haider et al. investigated the TiO_2 layer formed on the NiTi and NiTiCu surface as well as Cr_2O_3 and Ta_2O_5 layers formed on NiTiCr and NiTiTa surfaces.[51-52] Kassab et al. compared the corrosion behavior of ternary NiTi alloys adding Cu, Fe or Pd. For NiTiCu alloys, the lowest corrosion resistance and lowest oxide resistance was measured, leading to a poor stability of the oxide layer in NiTiCu. Furthermore, they revealed a distribution of metallic Cu within the TiO_2 layer.[57]

Even if quaternary NiTi based shape memory alloys are rarely investigated, orthodontic arch wires made of NiTiCuCr have been marketed as Copper NiTi™. Zhen et al. indicated the formation of a passive film of TiO_2 on a TiNiCuCr alloy. They exposed the alloy, which is used for orthodontic applications, to artificial saliva. Additional to the oxide formation, the alloy showed good corrosion resistance.[58]

The formation of a TiO_2 layer by electrochemical oxidation demonstrates a strategy to prevent the NiTiCuCr sample surface for corrosion and building a barrier against the Ni and Cu leakage. If the oxidation layer covers the complete sample surface, the concentration of Cu ion leakage could probably be reduced below ppb and reduce cytotoxicity, respectively.

7.5 Conclusions

In the present study, switchable topographies were induced into a quaternary shape memory alloy using the TWSME. The phase transformation temperatures, the temperature dependent surface topographies, and the cytotoxicity were analyzed in order to develop a metallic implant material with switchable surface topography.

» The DSC measurements revealed a phase transformation with small hysteresis near body temperature. At the operating temperature of 37 °C the material lies right between both peaks, leading to partial phase transformation. These material characteristics offer the possibility to switch the sample topography without (lethal) cell damage due to overheating or undercooling.

» Switchable topographies were induced using embossing and re-planarization. A surface with reversible change in roughness is elicited. Due to the partial phase transformation at 37 °C and the hysteresis, two different surface topographies can be induced at 37 °C, depending on the sample's thermal history.

» A high release of Cu ions has led to notable cytotoxicity and low cell viability. Electrochemical oxidation was applied in order to form a stable TiO_2 oxide layer on the surface. The oxidation process did not influence the induced switchable topographies.

A reversibly switchable micro- and nanotopography in a metallic shape memory alloy may allow to investigate time-dependent cell migration and alignment, as well as time-dependent cell-substrate interactions. Switchable topographical features on metallic implant devices, for example on intravascular stents, could first promote cell proliferation and guidance with a specific texture, and then stop the orientation by recovering a smooth surface. The control of the topographies could be triggered externally via induction heating, in a similar manner as presented by Müller et al.[7-8]

7.6 Acknowledgements

The author thanks M. Oberringer and W. Metzger from the faculty of medicine at the Saarland University in Homburg, for their expertise in cell-mechanbiology to develop the concept of this study. Similar gratitude is expressed to J. Atchison for her contributions in Raman spectroscopy and electrochemical oxidation and to E. Kroner for his support on the first manuscript of this study.

The research leading to these results was conducted within a Grant of the European Research Council, ERC Advanced Grant “Switch2Stick”, Agreement No. 340929, awarded to E. Arzt.

7.7 References

1. Duerig, T.; Pelton, A.; Stöckel, D., An overview of nitinol medical applications. *Materials Science and Engineering: A* **1999,** *273*, 149-160.
2. Saburi, T.; Tatsumi, T.; Nenno, S., Effects of heat treatment on mechanical behavior of Ti-Ni alloys. *Le Journal de Physique Colloques* **1982,** *43* (C4), C4-261-C4-266.
3. Gil, F.; Manero, J.; Planell, J., Relevant aspects in the clinical applications of NiTi shape memory alloys. *Journal of Materials Science: Materials in Medicine* **1996,** *7* (7), 403-406.
4. Serruys, P. W.; Kutryk, M. J., Handbook of coronary stents. **2011**.
5. Simon, M.; Kaplow, R.; Salzman, E.; Freiman, D., A Vena Cava Filter Using Thermal Shape Memory Alloy: Experimental Aspects 1. *Radiology* **1977,** *125* (1), 89-94.
6. Pfeifer, R.; Müller, C. W.; Hurschler, C.; Kaierle, S.; Wesling, V.; Haferkamp, H., Adaptable orthopedic shape memory implants. *Procedia CIRP* **2013,** *5*, 253-258.
7. Müller, C. W.; Pfeifer, R.; El-Kashef, T.; Hurschler, C.; Herzog, D.; Oszwald, M.; Haasper, C.; Krettek, C.; Gösling, T., Electromagnetic induction heating of an orthopaedic nickel–titanium shape memory device. *Journal of Orthopaedic Research* **2010,** *28* (12), 1671-1676.
8. Müller, C. W.; Pfeifer, R.; Meier, K.; Decker, S.; Reifenrath, J.; Gösling, T.; Wesling, V.; Krettek, C.; Hurschler, C.; Krämer, M., A Novel Shape Memory Plate Osteosynthesis for Noninvasive Modulation of Fixation Stiffness in a Rabbit Tibia Osteotomy Model. *BioMed research international* **2015,** *2015*.
9. Ignatius, A.; Blessing, H.; Liedert, A.; Schmidt, C.; Neidlinger-Wilke, C.; Kaspar, D.; Friemert, B.; Claes, L., Tissue engineering of bone: effects of mechanical strain on osteoblastic cells in type I collagen matrices. *Biomaterials* **2005,** *26* (3), 311-318.
10. Wataha, J. C.; O'Dell, N. L.; Singh, B. B.; Ghazi, M.; Whitford, G. M.; Lockwood, P. E., Relating nickel-induced tissue inflammation to nickel release in vivo. *Journal of Biomedical Materials Research* **2001,** *58* (5), 537-544.
11. Shevchenko, N.; Pham, M.-T.; Maitz, M., Studies of surface modified NiTi alloy. *Applied Surface Science* **2004,** *235* (1), 126-131.
12. El Feninat, F.; Laroche, G.; Fiset, M.; Mantovani, D., Shape memory materials for biomedical applications. *Advanced Engineering Materials* **2002,** *4* (3), 91.
13. Thierry, B.; Tabrizian, M.; Trepanier, C.; Savadogo, O.; Yahia, L. H., Effect of surface treatment and sterilization processes on the corrosion behavior of NiTi shape memory alloy. *Journal of Biomedical Materials Research* **2000,** *51* (4), 685-693.
14. Palmaz, J. C.; Benson, A.; Sprague, E. A., Influence of surface topography on endothelialization of intravascular metallic material. *Journal of vascular and interventional radiology* **1999,** *10* (4), 439-444.
15. Wirth, C.; Comte, V.; Lagneau, C.; Exbrayat, P.; Lissac, M.; Jaffrezic-Renault, N.; Ponsonnet, L., Nitinol surface roughness modulates in vitro cell response: a comparison between fibroblasts and osteoblasts. *Materials Science and Engineering: C* **2005,** *25* (1), 51-60.
16. Khang, D.; Carpenter, J.; Chun, Y. W.; Pareta, R.; Webster, T. J., Nanotechnology for regenerative medicine. *Biomedical microdevices* **2010,** *12* (4), 575-587.
17. Carpenter, S.; Garza, A.; Palmaz, J. C. Method for making topographical features on a surface of a medical device. US 9050394 B2, **2012**.

18. Carpenter, S.; Poor, M.; Palmaz, J. C. Topographical features and patterns on a surface of a medical device and methods of making the same. US 20140114435 A1, **2013**.
19. Curtis, A.; Wilkinson, C., Topographical control of cells. *Biomaterials* **1997,** *18* (24), 1573-1583.
20. Dalby, M. J.; Gadegaard, N.; Tare, R.; Andar, A.; Riehle, M. O.; Herzyk, P.; Wilkinson, C. D.; Oreffo, R. O., The control of human mesenchymal cell differentiation using nanoscale symmetry and disorder. *Nature materials* **2007,** *6* (12), 997-1003.
21. Ebara, M., Shape-memory surfaces for cell mechanobiology. *Science and Technology of Advanced Materials* **2015,** *16* (1), 014804.
22. Hook, A. L.; Voelcker, N. H.; Thissen, H., Patterned and switchable surfaces for biomolecular manipulation. *Acta Biomaterialia* **2009,** *5* (7), 2350-2370.
23. Greco, F.; Mattoli, V., Introduction to active smart materials for biomedical applications. In *Piezoelectric Nanomaterials for Biomedical Applications*, Springer: **2012**, pp 1-27.
24. Skorb, E. V.; Andreeva, D. V., Surface Nanoarchitecture for Bio-Applications: Self-Regulating Intelligent Interfaces. *Advanced Functional Materials* **2013,** *23* (36), 4483-4506.
25. Park, J. B.; Lakes, R. S., Metallic implant materials. *Biomaterials* **2007**, 99-137.
26. Liu, X.; Chu, P. K.; Ding, C., Surface modification of titanium, titanium alloys, and related materials for biomedical applications. *Materials Science and Engineering: R: Reports* **2004,** *47* (3), 49-121.
27. Zhang, Y.; Cheng, Y. T.; Grummon, D. S., Shape memory surfaces. *Applied Physics Letters* **2006,** *89*, 041912.
28. Ni, W.; Cheng, Y.-T.; Grummon, D. S., Microscopic shape memory and superelastic effects under complex loading conditions. *Surface and Coatings Technology* **2004,** *177*, 512-517.
29. Zhang, Y.; Cheng, Y.-T.; Grummon, D. S., Two-way indent depth recovery in a NiTi shape memory alloy. *Applied Physics Letters* **2006,** *88* (13), 131904-131904-3.
30. Fei, X. L.; Zhang, Y. J.; Grummon, D. S.; Cheng, Y. T., Indentation-induced two-way shape memory surfaces. *Journal of Materials Research* **2009,** *24* (3), 823-830.
31. Gaetke, L. M.; Chow, C. K., Copper toxicity, oxidative stress, and antioxidant nutrients. *Toxicology* **2003,** *189* (1), 147-163.
32. Elshahawy, W. M.; Watanabe, I.; Kramer, P., In vitro cytotoxicity evaluation of elemental ions released from different prosthodontic materials. *Dental materials* **2009,** *25* (12), 1551-1555.
33. Cao, B.; Zheng, Y.; Xi, T.; Zhang, C.; Song, W.; Burugapalli, K.; Yang, H.; Ma, Y., Concentration-dependent cytotoxicity of copper ions on mouse fibroblasts in vitro: effects of copper ion release from TCu380A vs TCu220C intra-uterine devices. *Biomedical microdevices* **2012,** *14* (4), 709-720.
34. Gu, Y. W.; Tay, B. Y.; Lim, C. S.; Yong, M. S., Characterization of bioactive surface oxidation layer on NiTi alloy. *Applied Surface Science* **2005,** *252* (5), 2038-2049.
35. Firstov, G. S.; Vitchev, R. G.; Kumar, H.; Blanpain, B.; Van Humbeeck, J., Surface oxidation of NiTi shape memory alloy. *Biomaterials* **2002,** *23* (24), 4863-4871.
36. Iijima, M.; Ohno, H.; Kawashima, I.; Endo, K.; Mizoguchi, I., Mechanical behavior of superelastic nickel-titanium orthodontic wires with different transformation temperature under different temperature and stresses. *Dent Mater* **2002,** *18*, 88-93.
37. Ball, J. M.; James, R. D., Fine phase mixtures as minimizers of energy. In *Analysis and Continuum Mechanics*, Springer: **1989**, pp 647-686.

38. Nam, T. H.; Saburi, T.; Shimizu, K. i., Cu-content dependence of shape memory characteristics in Ti–Ni–Cu alloys. *Materials Transactions, JIM* **1990,** *31* (11), 959-967.
39. Zarnetta, R.; Takahashi, R.; Young, M. L.; Savan, A.; Furuya, Y.; Thienhaus, S.; Maaß, B.; Rahim, M.; Frenzel, J.; Brunken, H., Identification of Quaternary Shape Memory Alloys with Near-Zero Thermal Hysteresis and Unprecedented Functional Stability. *Advanced Functional Materials* **2010,** *20* (12), 1917-1923.
40. Jaeger, S.; Maaß, B.; Frenzel, J.; Schmidt, M.; Ullrich, J.; Seelecke, S.; Schütze, A.; Kastner, O.; Eggeler, G., On the widths of the hysteresis of mechanically and thermally induced martensitic transformations in Ni–Ti-based shape memory alloys. *International Journal of Materials Research* **2015,** *106* (10), 1029-1039.
41. Maaß, B. Strukturbildungsprozesse bei der Herstellung und funktionelle Eigenschaften pseudoelastischer Ni-Ti-Cu-(X)-Formgedächtnislegierungen. Dissertation, Ruhr-Universität Bochum, Bochum, **2012**.
42. Wang, Q.; Zheng, Y.; Liu, Y., Microstructure, martensitic transformation and superelasticity of Ti 49.6 Ni 45.1 Cu 5 Cr 0.3 shape memory alloy. *Materials Letters* **2011,** *65* (1), 74-77.
43. Suzuki, Y.; Ohkata, I.; Yamauchi, K.; Inaba, T.; Kobayashi, J., Recent activities of Association of Shape Memory Alloys(ASMA) in Japan. *Shape Memory Materials'94* **1994**, 519-522.
44. Lin, H. C.; Yang, C. H.; Lin, K. M.; Hsu, G. K., A study of Ti50−x/2Ni40−x/2Cu10Crx (x = 0 ~ 1 at.%) shape memory alloys. *Journal of Alloys and Compounds* **2005,** *386* (1–2), 157-164.
45. Meling, T. R.; Ødegaard, J., The effect of short-term temperature changes on the mechanical properties of rectangular nickel titanium archwires tested in torsion. *The Angle orthodontist* **1998,** *68* (4), 369-376.
46. Brantley, W. A.; Eliades, T., Orthodontic materials: scientific and clinical aspects. Thieme: **2011**.
47. Loesberg, W.; Te Riet, J.; van Delft, F.; Schön, P.; Figdor, C.; Speller, S.; van Loon, J.; Walboomers, X.; Jansen, J., The threshold at which substrate nanogroove dimensions may influence fibroblast alignment and adhesion. *Biomaterials* **2007,** *28* (27), 3944-3951.
48. Loesberg, W. A.; te Riet, J.; van Delft, F. C. M. J. M.; Schön, P.; Figdor, C. G.; Speller, S.; van Loon, J. J. W. A.; Walboomers, X. F.; Jansen, J. A., The threshold at which substrate nanogroove dimensions may influence fibroblast alignment and adhesion. *Biomaterials* **2007,** *28* (27), 3944-3951.
49. Simon, C.; Palmaz, J. C.; Sprague, E., Influence of topography on endothelialization of stents: clues for new designs. *Journal of long-term effects of medical implants* **2000,** *10* (1&2).
50. Ebara, M.; Uto, K.; Idota, N.; Hoffman, J. M.; Aoyagi, T., Shape-Memory Surface with Dynamically Tunable Nano-Geometry Activated by Body Heat. *Advanced Materials* **2012,** *24* (2), 273-278.
51. Haider, W.; Munroe, N.; Pulletikurthi, C.; Gill, P. K. S.; Amruthaluri, S., A comparative biocompatibility analysis of ternary nitinol alloys. *Journal of materials engineering and performance* **2009,** *18* (5-6), 760-764.
52. Haider, W.; Munroe, N., Assessment of corrosion resistance and metal ion leaching of nitinol alloys. *Journal of materials engineering and performance* **2011,** *20* (4-5), 812-815.

53. Hwang, C.-J.; Shin, J.-S.; Cha, J.-Y., Metal release from simulated fixed orthodontic appliances. *American Journal of Orthodontics and Dentofacial Orthopedics* **2001,** *120* (4), 383-391.
54. Heidenau, F.; Mittelmeier, W.; Detsch, R.; Haenle, M.; Stenzel, F.; Ziegler, G.; Gollwitzer, H., A novel antibacterial titania coating: metal ion toxicity and in vitro surface colonization. *Journal of Materials Science: Materials in Medicine* **2005,** *16* (10), 883-888.
55. Heinecke, J. W.; Rosen, H.; Chait, A., Iron and copper promote modification of low density lipoprotein by human arterial smooth muscle cells in culture. *Journal of Clinical Investigation* **1984,** *74* (5), 1890.
56. Heidenau, F.; Ziegler, G. Strukturierte Beschichtungen für Implantate sowie Verfahren zu deren Herstellung. DE102006041023A1, **2007**.
57. Kassab, E.; Neelakantan, L.; Frotscher, M.; Swaminathan, S.; Maaß, B.; Rohwerder, M.; Gomes, J.; Eggeler, G., Effect of ternary element addition on the corrosion behaviour of NiTi shape memory alloys. *Materials and Corrosion* **2014,** *65* (1), 18-22.
58. Zheng, Y. F.; Wang, Q.; Li, L., The electrochemical behavior and surface analysis of Ti49. 6Ni45. 1Cu5Cr0. 3 alloy for orthodontic usage. *Journal of Biomedical Materials Research Part B: Applied Biomaterials* **2008,** *86* (2), 335-340.

Chapter 8
Summary and outlook

8.1 General summary

Frequently used materials, which are capable to show a reversible shape change, are near equiatomic nickel-titanium (NiTi) shape memory alloys. Emerging research on NiTi shape memory alloys has established that a reversible two-way shape memory surface can be induced using indentation techniques. By the use of this preparation technique the surface shows a reversible change from a smooth to a structured topography depending on the temperature.

Many functional surfaces with super-hydrophobic, (anti-) reflective, adhesive or bioactive properties, gain their functionality due to specific nano- and microstructures. A change in their spatial arrangement due to a switchable topography may also lead to a switchability of their surface function. For example the adhesion of a surface with dry adhesive microstructures could be changed by switching from a flat to a structured topography and vice versa. This responsiveness of the properties to a stimulus, such as temperature, will widen their current field of applications.

The aim of this thesis was to investigate the indentation induced two-way shape memory effect (TWSME), in order to (i) understand the microstructural transformation mechanisms and control the switchable surface structures, (ii) to simplify and establish a surface preparation process for larger areas, (iii) to present an approach for an application of switchable shape memory surfaces, and (iv) to transfer the TWSME onto another shape memory alloy to activate switchable microtopographies by body heat. Subsequently, as shown in Figure 8.1, a summary of the main research and results carried out on these sections is given.

(i) Understanding the two-way shape memory effect and switchable surface structures in NiTi alloys

Limited studies exists on investigating the effect of pre-existing Ti_3Ni_4 precipitates on the TWSME in NiTi shape memory alloys. The core theory is that the size of precipitates strongly influences the formation of stress-induced martensite, which is critical for the TWSME. Therefore, the role of pre-existing precipitates on the indentation induced TWSME in an austenitic NiTi alloy was investigated in the present study by a systematic variation of aging temperature, leading to solutionized, coherent or incoherent Ti_3Ni_4 precipitates. Vickers indentation on differently aged NiTi, followed by planarization and subsequently observing the evolution of the surface topography as a function of temperature gave insight into the fundamentals of the two-way shape memory behavior.

- The experiments demonstrated an indentation induced two-way shape memory effect in austenitic NiTi, depending on former heat treatment. A two-way shape memory effect was only found in solutionized and 400°C aged material, containing semi-coherent Ti_3Ni_4 precipitates.
- It was concluded that upon indentation the induced stress fields contribute to the activation of corresponding martensite variants during phase transformation. Leading to the temperature-induced macroscopic change in topography.
- The flat or the structured topography was shown to be stable at room temperature, depending on the sample's thermal history. Coming from the cooled state, below M_f, the surface was flat at room temperature and coming from the heated state, above A_f, the sample was structured at room temperature.
- A critical temperature was found which leads to the increase of protrusion height and decrease of reversibility. The two-way shape memory effect disappeared with heating the samples significantly above the transformation temperature. This was attributed to the critical role of stabilized martensite.

The insight into the influence of heat treatment, microstructure, and cycling temperature on the indentation induced TWSME will be a helpful complement in order to match the desired switching temperature for a certain application with the right shape memory alloy composition. For example with the austenitic material, a switchable topography with a shape memory effect around room temperature was induced. Besides that, the austenitic material has superior mechanical properties compared to the martensitic material. The increased young's modulus and hardness in the austenitic state might be of importance for load bearing or anti-abrasive applications.

Furthermore, the shown loss of the TWSME due to overheating significantly above the transformation temperatures is a crucial limitation regarding the development of new preparation techniques. This had to be taken into account for the subsequent objective of the present thesis – the development of a new preparation process.

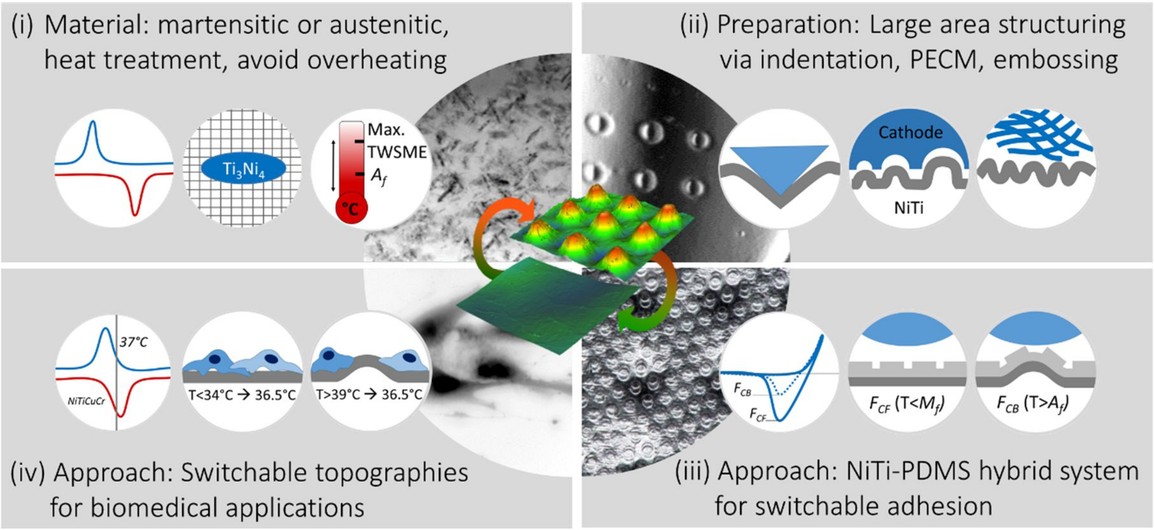

Figure 8.1: Graphical summary on the four sections, related to two-way shape memory topographies, investigated in the present thesis. (i) Microstructural characterization and analysis of the TWSME in austenitic NiTi shape memory alloys. A TWSME was induced by heat treatment leading to coherent Ti3Ni4 precipitates. Overheating of the sample exceeding the austenite finish temperature removed the TWSME. (ii) The previously used indentation process to prepare shape memory topographies was supplemented by an electrochemical microstructuring and cold-embossing process. (iii) A first approach, which combines NiTi with a dry adhesive PDMS layer, has led to a functional surface with temperature-induced switchable adhesion. The change in adhesive properties was induced by a change in contact area. (iv) In order to gain a switchable topography, which can be triggered near body temperature, the TWSME was induced in a NiTiCuCr alloy. The small hysteresis width of the alloy enables a flat and a structured state at 37 °C depending on the sample's thermal history.

(ii) *Development of a large area structuring (preparation) process for two-way shape memory topographies*

The switchable topographies of TWSME surfaces give rise to potential applications in the field of optical and biomedical devices or switchable dry adhesives. The implementation of these ideas mostly requires the structuring of larger arrays at a time and less elaborate preparation techniques are preferred. Since common machining processes are withdrawn, due to strong generation of heat, which deteriorates the shape memory behavior and the extraordinary mechanical properties of NiTi shape memory alloys, cold embossing and pulsed electrochemical machining (PECM) were applied.

In order to save material resources and reduce preparation complexity the single indentations and multiple grinding steps for the current state of the art preparation of shape memory surfaces were replaced by two steps of cold embossing. A polished NiTi sample was first embossed with a metallic micro-mesh, and second re-planarized using a nearly flat emboss. Measurements using white light interferometry show that a TWSME, which leads to the switchable microtopographies, was successfully induced on the sample.

» The main geometric features of the mesh were stored intrinsically in the embossed sample surface and appear from the optically smooth NiTi surface when the sample was heated above the critical transformation temperature.

» After cooling the sample back to room temperature, the structures disappeared almost entirely. As for the single indentation structuring, the switch in topography is shown to be reversible over multiple temperature cycles.

» The switchable surface structures approximately reached the original dimensions of the mesh and led to a reversible change in surface roughness.

In a second experimental set up, PECM was applied to structure the NiTi surface with both low heat generation and sub-surface deformation during manufacturing. Two different tools were used to form linear and bumpy protrusions on the NiTi surface. Subsequently, these protrusions were flattened in order to replanarize the surface. After one step of polishing, the topography was analyzed via white light interferometry and three dimensional optical microscopy at room temperature, above the transformation temperature and after cooling to room temperature. The following observations were made:

- The results revealed that a formation of structures on the surface via PECM is technically possible. Linear and semispherical microstructures of different size remained on top of the NiTi substrate after PECM.
- A two-way shape memory effect was induced by the compression of the structures into the surface. This technique led to an array with switchable microtopography.
- In addition to the occurring shape change, which forms elevated structures on top of the surface, also a sink-in shape change was observed, which formed cavities in the surfaces. Thus, the apparent compression of structures has led to two different deformation orientations of the two-way shape memory effect: Raised surface protrusions, which are surrounded by a sunken groove, were formed.

The results prove that deformation mechanisms for larger areas, like cold embossing and PECM, can be applied to generate microtopographies with a two-way shape memory effect. Cold embossing and PECM are already applied in industry using roll-to-roll processes or larger scale batch processes. Thus, a first step in up-scaling of switchable topographies in NiTi was made. Apart from that, the results of the compression experiments gave further insight in the complex interaction of induced deformation, microstructure, and the TWSME in NiTi shape memory alloys. The shown shape change behavior provides the impetus for additional detailed microstructural analysis.

Gaining switchable topographies on larger scale by use of the developed preparation techniques, may lead to systems, which combine functional microstructures and switchability to access a dynamic surface response. The practical feasibility of this idea was examined within the framework of this thesis: The design of a hybrid system with temperature-induced switchable adhesion.

(iii) Combining functional microstructures and switchable surfaces - an approach to encounter switchable adhesion

Many industrial processes require efficient adhesion systems to grip and release fragile objects such as wafers, lenses or glass plates. State-of-the-art solutions such as vacuum-based handling systems are cost-intensive and have limitations in their applicability. An alternative are micro-patterned bioinspired dry adhesive surfaces similar to those found in biological adhesion systems of spiders and geckos. These synthetic micro-patterned adhesives allow an easy adaptation to a variety of surfaces, causing an increase in contact area at negligible elastic strain and, thus, improved adhesion. One significant barrier for the application of these micro-patterned surfaces is the lack of switchability.

A novel switchable dry adhesive, which combines an adhesive silicone rubber with a NiTi shape memory alloy was developed. NiTi is trained by surface deformation and grinding, to elicit a temperature-induced switchable microtopography with protrusions at high temperature and a flat surface at low temperature. The trained surface was coated with either a flat or a micro-patterned adhesive polydimethylsiloxane (PDMS) layer, resulting in a temperature-induced switchable surface, to tune dry adhesion. Adhesion tests show that the topographical change of the NiTi strongly influences the adhesive performance of the hybrid system.

» The transition between the flat and the structured NiTi topography reduced adhesion by 56% for a sample with a smooth PDMS layer and by 100% for a sample with a patterned PDMS layer.

» The hybrid systems revealed strong reversibility, allowing repeated switching between an adhesive and a less/non-adhesive surface over frequent temperature cycles.

» The change in adhesion was discussed in terms of reversible changes in contact area based on classic contact mechanics models and a Finite Element model. The comparison with the models verified that the change in the contact area due to the TWSME is responsible for the loss in adhesion.

The significant switch in the adhesion performance opens possibilities to tailor dry adhesive systems showing strong adhesive properties and easy detachment, which is required for pick and place processes of sensitive objects. Apart from adhesion phenomena, switchable microtopographies and the change in contact area have a substantial influence on cell-growth and cell-behavior (proliferation), which are key features in the field of biomedical applications. Motivated by this and taking into account the previous results, a switchable microtopography, triggered at body temperature, was induced on a novel shape memory alloy.

(iv) Switchable microtopographies activated at body temperature in a quaternary shape memory alloy

The development of switchable surfaces for biomedical devices is in the focus of many studies, since surface chemistry and topography are known to have a strong influence on cell response. Based on the previous chapters, the goal was to develop a shape memory alloy, which can reversibly switch its topography but has a switching temperature around body temperature. The use of a two-way shape memory topography will allow changing between both states - smooth and patterned - without modifying the surface chemistry. This is crucial to understand the cell mechanobiology, i.e. the complex interaction of the cell with the implant material. A quaternary $Ni_{42.5}Ti_{49.65}Cu_{7.5}Cr_{0.35}$ alloy system was used to elicit a martensitic phase transition around 37 °C and a recovery with small hysteresis width. These material characteristics offer the possibility to switch the sample topography without (lethal) cell damage due to overheating or undercooling.

- By heating the sample surface above 36 °C up to 40 °C the topography changed from flat to bumpy, and vice versa upon cooling the sample back from 35 °C to 30 °C.
- It was observed that both topographies, smooth and patterned, are stable at 37 °C, depending on the thermal history of the sample. The phase transformation near body temperature enables a flat surface at 37 °C, coming from the martensitic state (30 °C) and a structured topography coming from the austenitic state (40 °C).
- The immersion of a NiTiCuCr sample in cell cultivation media for two days exhibited a very high concentration of copper ions, which are known to be toxic for cells. This leakage of Cu-ions should be reduced by pacifying the surface via electrochemical oxidation, primarily leading to growth of TiO_2 and CuO layers.

The reduction of cytotoxicity in combination with the reversible switch of the surfaces topography near body temperature opens possibilities to stimulate biomedical surfaces, which might be able to tune cell growth and cell adhesion dynamically. More specifically, a batch of NiTiCuCr samples with and without switchable topographies will be used to analyze the cell responsiveness for a change in roughness. The influence of the switch from a smooth to a structured topography and vice versa on cell growth will be observed.

8.2 Outlook

Various aspects related to the indentation induced TWSME in shape memory alloys have been presented in this work. The literature review revealed two main aspects: First, most previous work has focused on the phenomenological understanding of the TWSME. Second, and as a result of the present research, a systematic microstructural analysis which may build the bridge from a fundamental microstructural understanding to the phenomenological observations, is missing. Hence, a detailed TEM investigation of the areas beneath the deformed material is of considerable interest. *In situ* TEM heating and cooling experiments could give insights into the specific phase transformation behavior leading to the TWSME, e.g. the detailed role of stabilized martensite.

The development of new preparation techniques was another topic of the present thesis. That a switchable surface topography could be induced via cold embossing and electrochemical machining is a promising result regarding upscaling for industrial applications. Both techniques were already used in industry, either in form of roll-to-roll processing or batch processing. The size of the switchable surface structures ranges from micro- to millimeter scale, but also smaller structure sizes could be induced. In a first try, micro-holes on a wafer were successfully transferred onto the NiTiCuCr surface resulting in micro-pillars, but during the experiments, the brittle wafer burst. Thus, in principle the small feature size can be transferred via embossing. Only the structuration of a wear resistant tool with the positive master structures will be challenging. Apart from embossing, also electrochemical machining is already applied for structuration on different scales.[1] As shown by Weinmann and colleagues a high machining accuracy, for micromechanical machining systems, could be reached in steel, using pulsed electrochemical micromachining and a proper tool design. Mineta and their team investigated the fabrication of very thin NiTi sheets for biomedical applications via electrolysis. It would be of interest if such a high machining accuracy and thin NiTi foils with a switchable topography could also be fabricated in a similar manner.[2] If the switchable topographies will not longer be limited to flat bulk material, but could be induced on deformable sheets and foils, additional applications especially in biomedicine and micro actuation would be accessible.[3-4] Analogue to the self-deployable origami stent with hill and valley folds, presented by Kuribayashi et al., a switchable topography on a stent foil would be able to influence cell-growth and thus, promote the healing process after vascular disease. [5]

Alternative possible applications for switchable TWSME surfaces were discussed in the present thesis. The presented approaches were successful 'proof of concepts', but a detailed transfer into possible industrial applications was not yet achieved. The approach to utilize a switchable topography in a NiTi-PDMS hybrid system allowing switchable adhesion, yielded promising results, such as good adhesive performance and near-ideal recovery rates. By the use of mushroom structures - pillars with a broadened cap on top, see Figure 8.2, the adhesion forces of these hybrid systems were increased, which enables the lifting of heavier weights. However, if this stronger adhesion force can be as easily reduced by switching the topography, as with the flat pillars, has to be proofed in further experiments.

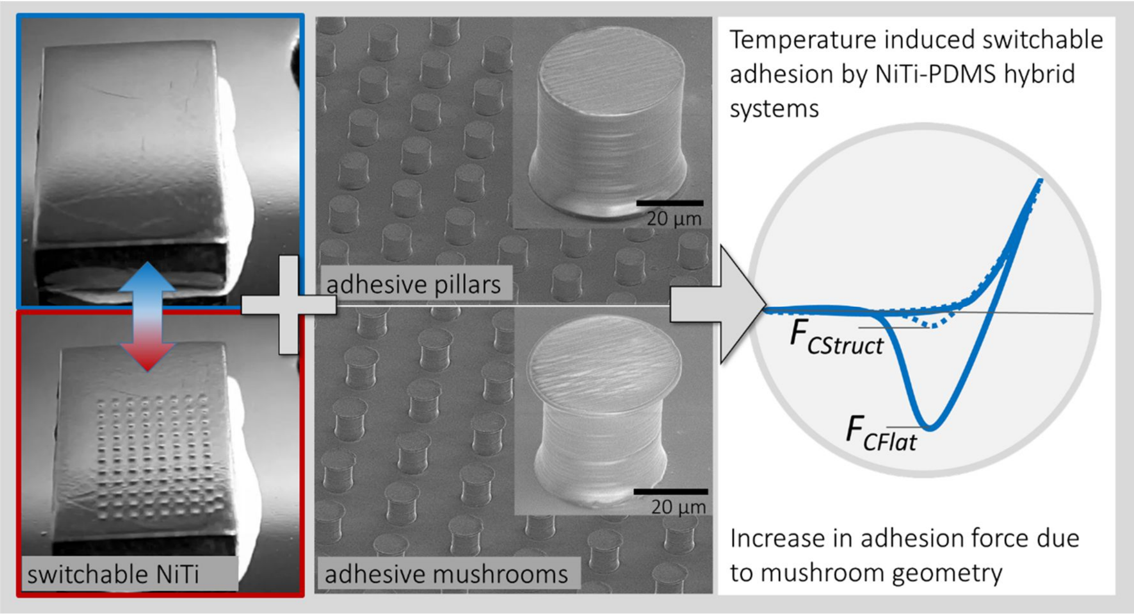

Figure 8.2: NiTi-PDMS hybrid system for temperature-induced switchable adhesion. A change from a pillar geometry to the bioinspired mushroom geometry leads to an increase in adhesion force. It has to be tested, whether the switchable NiTi topography induces a loss of adhesion in the structures state also for these hybrid samples.

In the field of optics, the combination of two-way shape memory topographies with optically active films or microstructures could be used to change the surface reflectivity. For example, the controllable change in surface roughness could lead to a change in the spacing of optical grits, and enable or disable Bragg-diffraction. To conclude, the presented approaches can be seen as inspiration for all applications were the effect of existing functional microstructures and/or functional coatings is strongly related to their spatial arrangement. The latter is proofed to be changeable by the use of TWSME topographies, as shown in this thesis.

The combination of a hydrophobic-hydrophilic surface with a specific switchable underlying topography could lead to a change in contact angle, e.g. a local control of wettability as shown in Figure 8.3. But also the combination of a switchable topography and a polymer coating with responsive wettability, as presented by Sun and colleague, could lead to enhanced control of surface wettability.[6] A responsive wettability might be of interest for microfluidic devices ranging from ink-jet printing to biomedical microelectromechanical systems (bioMEMS).[7-10] Surface wettability is a major driving force associated with switching proteins and cell attachment.[11] Thus, a hybrid system, combining a switchable NiTiCuCr surface with altering wettability regions may enable the manipulation of the adhesion-mediating proteins. As mentioned by Hook et al. such an implant system would show great potential: "The most interesting and useful systems are those that combine patterns on the micro- or even nanoscale and switchable architectures, as they are able to achieve both temporal and spatial control over biomolecule surface interactions."[12]

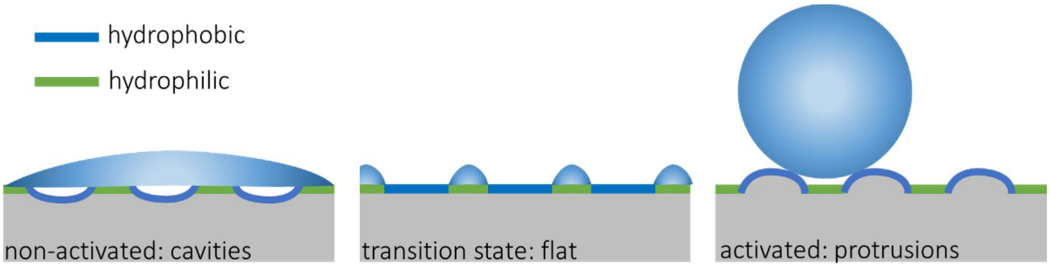

Figure 8.3: Schematic illustration of a surface system with controllable wetting properties. The change from hydrophilic to hydrophobic is driven by the switchable topography in combination with chemical surface modifications. A well-considered spatial arrangement of hydrophilic and hydrophobic areas on a surface with switchable surface arrays could improve local wettability.

A more elaborated approach would be the investigation of two-way shape memory topographies in ferromagnetic shape memory alloys. The transfer of the presented knowledge onto an alloy, which can be triggered by a magnetic field, would increase the field of applications significantly. Especially in the fields of biomedicine, or actuator techniques, a magnetic field, which can be switched easily and with high frequency between two states, would be of interest. Since temperature is a relatively slow stimulus and many elements or processes are sensitive to heat (cell growth, processors, tactile systems due to thermal expansion), the change from the thermal to a magnetic stimulus would offer many advantages.

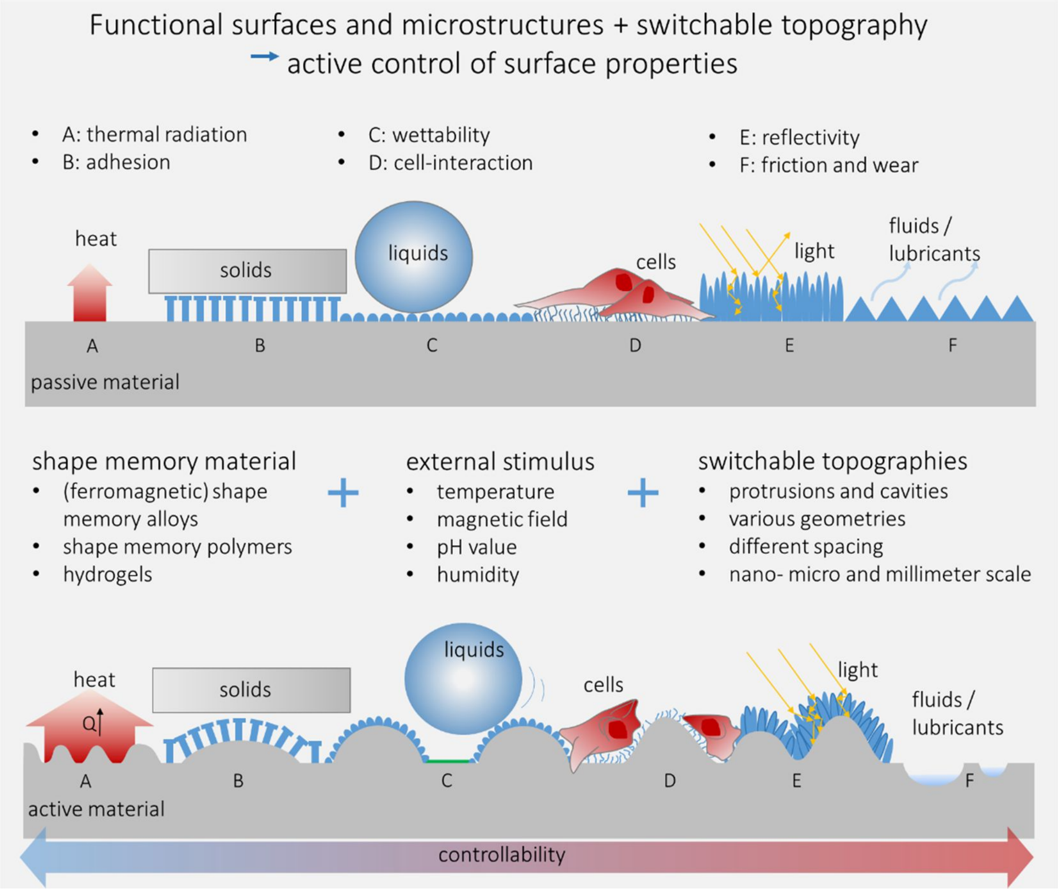

Figure 8.4: Scheme of active hybrid systems, which combine functional coatings or microstructures with a switchable topography. By the use of a shape memory topography on its own, or in combination with certain functional microstructures, static properties like wettability, reflectivity or lubrication could be actively changed. In general, all properties, which are influenced by the surface roughness and the contact area, should be able to be triggered using a shape memory substrate and the corresponding external stimulus.

8.3 References

1. Weinmann, M.; Weber, O.; Bähre, D.; Munief, W.; Saumer, M.; Natter, H., Photolithography–Electroforming–Pulse Electrochemical Machining: An Innovative Process Chain for the High Precision and Reproducible Manufacturing of Complex Microstructures. *International Journal of Electrochemical Science* **2014,** *9*, 3917-3927.
2. Mineta, T.; Mitsui, T.; Watanabe, Y.; Kobayashi, S.; Haga, Y.; Esashi, M., Batch fabricated flat meandering shape memory alloy actuator for active catheter. *Sensors and Actuators A: Physical* **2001,** *88* (2), 112-120.
3. Quandt, E.; Halene, C.; Holleck, H.; Feit, K.; Kohl, M.; Schloßmacher, P.; Skokan, A.; Skrobanck, K., Sputter deposition of TiNi, TiNiPd and TiPd films displaying the two-way shape-memory effect. *Sensors and Actuators A: Physical* **1996,** *53* (1), 434-439.
4. Kohl, M.; Liu, Y.; Krevet, B.; Dürr, S.; Ohtsuka, M. In *SMA microactuators for microvalve applications*, Journal de Physique IV (Proceedings), EDP sciences: **2004**; pp 333-342.
5. Kuribayashi, K.; Tsuchiya, K.; You, Z.; Tomus, D.; Umemoto, M.; Ito, T.; Sasaki, M., Self-deployable origami stent grafts as a biomedical application of Ni-rich TiNi shape memory alloy foil. *Materials Science and Engineering: A* **2006,** *419* (1), 131-137.
6. Sun, T.; Wang, G.; Feng, L.; Liu, B.; Ma, Y.; Jiang, L.; Zhu, D., Reversible Switching between Superhydrophilicity and Superhydrophobicity. *Angewandte Chemie International Edition* **2004,** *43* (3), 357-360.
7. Calvert, P., Inkjet printing for materials and devices. *Chemistry of Materials* **2001,** *13* (10), 3299-3305.
8. Delamarche, E.; Juncker, D.; Schmid, H., Microfluidics for processing surfaces and miniaturizing biological assays. *Advanced Materials* **2005,** *17* (24), 2911-2934.
9. Xin, B.; Hao, J., Reversibly switchable wettability. *Chemical Society Reviews* **2010,** *39* (2), 769-782.
10. Grayson, A. C. R.; Shawgo, R. S.; Johnson, A. M.; Flynn, N. T.; Li, Y.; Cima, M. J.; Langer, R., A BioMEMS review: MEMS technology for physiologically integrated devices. *Proceedings of the IEEE* **2004,** *92* (1), 6-21.
11. Ponsonnet, L.; Reybier, K.; Jaffrezic, N.; Comte, V.; Lagneau, C.; Lissac, M.; Martelet, C., Relationship between surface properties (roughness, wettability) of titanium and titanium alloys and cell behaviour. *Materials Science and Engineering: C* **2003,** *23* (4), 551-560.
12. Hook, A. L.; Voelcker, N. H.; Thissen, H., Patterned and switchable surfaces for biomolecular manipulation. *Acta Biomaterialia* **2009,** *5* (7), 2350-2370.

List of Figures

List of Tables